

Homo- and Heterogeneous Silicone Micro-Nano Structures: Synthesis, Functionalization and Applications

Dissertation

zur

Erlangung der naturwissenschaftlichen Doktorwürde

(Dr. sc. nat.)

Vorgelegt der

Mathematisch-naturwissenschaftlichen Fakultät

der

Universität Zürich

von

Kangwei Chen

aus

China

Promotionskommission

Prof. Dr. Stefan Seeger (Vorsitz)

Prof. Dr. Karl-Heinz Ernst

Prof. Dr. Greta Patzke

Zürich, 2024

To the gentle readers

Acknowledgements

First and foremost, I would like to sincerely thank Prof. Dr. Stefan Seeger for giving me the opportunity to carry out my doctoral thesis in his group and for giving me the freedom to explore the exciting world of material chemistry and nanotechnology. I am extremely grateful for his support, encouragement, and scientific supervision.

I would also like to thank Prof. Dr. Karl-Heinz Ernst and Prof. Dr. Greta Patzke for agreeing to be part of my Doctoral Committee.

I am deeply grateful to Dr. Shanqiu Liu for being excellent teamwork and for his kind guidance in the early stages of my doctoral research.

I would like to thank Dr. Yuan Li, Yuen Yee Lau, Dr. Wenzhe Niu, Zhenbin Wang, Dr. Jie Xu, Dr. Alexandre Laroche, Dr. Davide Bottone, and Dr. Georg Artus for sharing their invaluable knowledge and for their insightful advice.

I am thankful to Marino Kriftner and Marc Frey, whose master's theses provided important information for the synthesis of the DCMVS-based structures.

My special thanks to Dr. Andres Käch, Dr. Jana Döhner, and Dr. Joana Delgado Martins from the Center for Microscopy and Image Analysis (ZMB) of the University of Zurich for their kind help in sample preparation, microscopy imaging, and data process. I would also like to acknowledge the ZMB for providing their facilities.

I also wish to thank the whole Seeger group for creating a pleasant working environment and a relaxing atmosphere in the office: Prof. Dr. Stefan Seeger, Dr. Georg Artus, Dr. Yuan Li, Dr. Shanqiu Liu, Dr. Sandro Oliveira, Alessandro De Crema, Dr. Xiaotian Zhang, Dr. Noah Naef, Dr. Samet Varol, Dr. Behzad Sardari, Dr. Jie Xu, Dr. Alexandre Laroche, Dr. Davide Bottone, Dr. Cinzia Clamor, Dr. Subir Das, Rabab Azizi, Yuen Yee Lau, and Nathalia Münch.

I would also like to thank the people from the administration and workshop of the Department of Chemistry, especially Fabienne Stutz, Nicole Reimann, Dr. Sabine

Stockhause, Chantal Henningsen-Conus, Roland Zehnder, Teresa Sury, and Maja Gossweiler for their continuous support and help.

My thanks also go to the Graduate School of Chemical and Molecular Sciences Zurich (CMSZH) for the generous financial support and the joyful activities they organized.

Finally, and most important, words cannot express my gratitude to my parents and my girlfriend, Yiran Ji. I could not have undertaken this journey without their love, accompaniment, unconditional support, and encouragement.

Abstract

Controlling the physicochemical properties of solid surfaces is of utmost importance in many fields, from Life Sciences to Physics to Chemistry. Besides protection of the support material underneath, energy conversion, catalysis, and waterproofing properties are just a few examples. Creating rough surfaces on the micro and nanoscale and modifying the structures with different chemical compounds are considered promising methods to extend the applicability of the functional surfaces. Therefore, the interest in developing the new strategy that can fabricate morphological-tunable micro and nanostructures on solid surfaces, improving the efficiency and controllability of surface functionalization, and applying the functional surface coatings in different practical scenarios has been growing for many years.

In the first and second parts of this work, systematic investigations of the effects of the synthesis conditions on the morphology and surface properties of the single-component (SC) silicone nanostructures have been conducted. Practical applications of silicone nanorods (SNRs) materials have been explored. Especially when different cellulosic papers are used as the substrate, SNRs coating endows them with a completely different nanoscale surface texture. While maintaining normal appearance, printability, and writability, the decorated papers exhibit enhanced physicochemical durability and functionalities in waterproofing, self-cleaning, and anti-microbial.

In the third part, to investigate the geometrical effects of the coating structures, a dynamic Droplet Assisted Growth and Shaping (d-DAGS) synthesis strategy is developed to synthesize the stiff bamboo-shaped SC-SNRs. Unless the other silicone-based micro and nanostructures, such as filaments and wires, the obtained bamboo-shaped SNRs present many advanced features, including in situ controllable morphology, tunable height, robust anti-wetting property, and enhanced mechanical stiffness and chemical durability. Tentative applications of the as-prepared samples in promoting the buoyancy of the floating stuff, self-cleaning, and water harvesting have been successfully conducted, and exciting results have been obtained, for example, a

maximum water collecting rate (WCR) of $32.3 \pm 0.6 \text{ mg}\cdot\text{cm}^{-2}\cdot\text{min}^{-1}$ is achieved from the sample with 6-segments bamboo-shaped silicone coating, which is at an advanced level in related studies. In addition, the bottom-up growing mechanism is perfectly verified and explained by the d-DAGS mechanism. Further attempts to grow ultra-long rods with 12 and 18 segments (very high aspect ratio) expand the possibility of developing this method and replicating it on other materials.

In the final part, based on the d-DAGS method, different precursors are introduced to synthesize the multi-component hybrid (MCH) silicone nanostructures. Small units (segments) with different chemical compositions are arranged in a controllable specific order to form a bamboo-shaped structure, i.e., MCH-SNRs. The co-existence of the inert and reactive components enables the as-prepared superhydrophobic products to be modified directly and selectively. Region-selective functionalization (RSF) has been successfully performed on the level of a single nanostructure, whose modifiable regions hinge upon the dynamic arrangement of the synthesis process. A vertical region-selective protection (RSP) mechanism is proposed to explain the different surface behaviors of the functionalized MCH-SNRs samples. Additionally, confocal microscopy has been the first-time used to visually reveal the water penetration level and directly exhibit the intermediate wetting state.

In addition, a mushroom-like structure, namely, silicone micro-hoodoos (SMHs), has been synthesized when tri-chlorosilane and di-chlorosilane are mixed during the synthesis process. A possible new growing mechanism is proposed and discussed. The excellent anti-adhesive performance shown in the adhesive loop tack strength test of this unique structure strongly supports their potential applications in protecting the substrates underneath the functional coatings.

In summary, the results presented in this work systematically demonstrate the one-step synthesis, in-situ shape control, region-selective functionalization, and practical applications of the homo- and heterogeneous silicone-based nanostructures. Further developing and applying the presented facile, efficient, and low-cost d-DAGS method on other materials will provide more opportunities to engineer the surfaces and interfaces with unique physicochemical properties, expand the applicability of the functional coatings, and explore the new world of material science and nanotechnology.

Publications and Conferences

Research Articles

- **Chapter 4.1 & 4.2**
Liu, S.*, **Chen, K.***, Salim, A., Li, J., Bottone, D. & Seeger, S.:
Printable and Versatile Superhydrophobic Paper via Scalable Nonsolvent Armor Strategy
ACS Nano **2022**, 16, 9442-9451. (*Co-first author)
- **Chapter 4.1 & 4.3**
Chen, K., Liu, S., Lau, Y.-Y. & Seeger, S.:
One-Step Synthesis of Dynamically Shaped Stiff Nanorods Using Soft Silicone Materials to Control Water Repulsion and Collection
Small **2022**, 18 (40), 2203820. (Selected as Front Cover)
- **Chapter 4.1 & 4.4**
Chen, K., Xu, J., Laroche, A., Lau, Y.-Y. & Seeger, S.:
Heterogeneous Silicone Nanorods with Region-Specific Functionality
Manuscript submitted
- **Chapter 4.4**
Chen, K., Frey, M., Kriftner, M. & Seeger, S.:
Mushroom-Shaped Silicone Nanostructure as a Functional Coating in Anti-Adhesive Application
Manuscript in preparation

- **Chen, K.** & Seeger, S.:
Hierarchical Structured Silicone Nano-Trees for Wastewater Treatment
Manuscript in preparation

- Lau, Y.-Y., **Chen, K.**, Liu, S., Reith, L. & Seeger, S.:
Silicone Nanofilament Coatings as Flexible Catalyst Supports for a
Knoevenagel Condensation Reaction in Batch and Flow Systems
ACS omega **2022**, 7, 43, 39463-39470.

- Lau, Y.-Y., **Chen, K.** & Seeger, S.:
Silicone Nanofilaments-Based Coating Approach for Point-of-Use Drinking
Water Treatment
Manuscript submitted

Contribution to Conferences

Conferences

- **Chen, K.** & Seeger, S.:
One-Step Synthesis of Dynamically Shaped Stiff Silicone Nanorods
Oral presentation, 17th European Congress and Exhibition on Advanced Materials and Processes, Frankfurt am Main, Germany, 03 - 07 September, 2023.

- **Chen, K.** & Seeger, S.:
Dynamic Synthesis of Bamboo-Shaped Silicone Nanorods to Control Water Repulsion and Collection
Poster presentation, SCS Fall Meeting 2023, Bern, Switzerland, 24 - 25 August, 2023.
(Best Poster Presentation Award)

Symposiums

- **Chen, K.** & Seeger, S.:
One-Step Synthesis of Dynamically Shaped Stiff Nanorods Using Soft Silicone Materials
Poster presentation, Doktorandentag, Zurich, Switzerland, 13 September, 2022.

- **Chen, K.** & Seeger, S.:
One-Step Synthesis of Dynamically Shaped Stiff Nanorods Made from Soft Silicone Materials and Its Use to Control Water Repulsion and Collection
Oral presentation, 13th CMSZH Retreat, Savognin, Switzerland, 15 - 17 June, 2022.

Contents

Acknowledgements	I
Abstract.....	III
Publications and Conferences	V
Research Articles	V
Contribution to Conferences	VII
Contents	VIII
Abbreviations	XII
List of Symbols	XIV
Physical Constants	XIV
Symbols	XV
1. Introduction.....	1
2. Theory and Background.....	5
2.1 Silicone chemistry.....	5
2.1.1 General aspects	5
2.1.2 Synthesis of polysiloxanes.....	6
2.1.3 Surface silylation and chemical structures of silsesquioxanes	8
2.1.4 Silicone-based micro- and nanomaterials.....	10
2.1.5 Fabrication methods and mechanisms	11
2.1.6 Chemical modifications	16
2.1.7 Applications	18
2.2 Wetting of solid surfaces	20
2.2.1 Homogeneous planar solid surface.....	20

2.2.2 Rough and heterogeneous solid surface	21
2.2.3 Intermediate wetting state.....	23
3. Materials and Methods.....	24
3.1 Materials	24
3.1.1 Chemicals	24
3.1.2 Substrates.....	25
3.2 General synthetic protocol.....	27
3.2.1 Experimental setup	27
3.2.2 Experimental procedure.....	28
3.3 Synthesis of SC silicone nanostructures	31
3.3.1 Silicone nanofilaments	31
3.3.2 Silicone nanorods	31
3.3.3 Bamboo-shaped silicone nanorods	33
3.4 Synthesis of MCH silicone nanostructures	35
3.4.1 Bamboo-shaped nanostructures	35
3.4.2 Mushroom-shaped nanostructures	36
3.5 Chemical functionalization on MCH silicone nanostructures	37
3.6 Sample evaluation and characterizations	38
3.6.1 Chemical durability test.....	38
3.6.2 Mechanical durability test	39
3.6.3 Environmental durability test	40
3.6.4 Buoyancy test	40
3.6.5 Biological test.....	41
3.6.6 Water harvesting	41
3.6.7 Ninhydrin test	42
3.6.8 High-speed camera	42
3.6.9 Contact angle goniometry.....	44

3.6.10 Fourier transform infrared spectroscopy (FT-IR)	44
3.6.11 UV-vis spectroscopy	44
3.6.12 Scanning electron microscopy (SEM)	44
3.6.13 Transmission electron microscopy (TEM)	45
3.6.14 Confocal microscopy	45
4. Results and Discussion.....	47
4.1 Synthetic parameters of the regular SC-SNRs	47
4.1.1 ETCS-based silicone nanostructures	47
4.1.2 VTCS-based silicone nanostructures	50
4.1.3 Cellulosic-paper-based substrate	51
4.1.4 Summary.....	53
4.2 Characterizations and applications of ETCS-SC-SNRs on cellulosic-paper-based substrate	54
4.2.1 Synthesis and characterizations of the ETCS-SC-SNRs coating	54
4.2.2 Robust superhydrophobicity of the SNRs-paper	57
4.2.3 Scale-up fabrication.....	60
4.2.4 Printability and writability of the SNRs-paper	60
4.2.5 Applying ETCS-SC-SNRs on preprinted cellulosic-paper-based substrate	63
4.2.6 Antimicrobial functionality.....	66
4.2.7 Other cellulosic-paper-based substrates	67
4.3 Synthesis and applications of the bamboo-shaped SC-SNRs.....	68
4.3.1 d-DAGS mechanism.....	68
4.3.2 Characterizations of the bamboo-shaped SNRs	73
4.3.3 Ultra-long bamboo-shaped SNRs.....	75
4.3.4 Robust superhydrophobicity.....	77
4.3.5 Transparency of the bamboo-shaped SNRs coatings	81
4.3.6 Enhanced chemical, environmental, and mechanical durability	83

4.3.7 Buoyancy promotion and self-cleaning	87
4.3.8 Water-harvesting	88
4.4 Synthesis and functionalization of the MCH silicone nanostructures.....	94
4.4.1 Synthesis of the MCH structures	94
4.4.2 Microscopic characterizations of the MCH structures	98
4.4.3 Geometrical parameters	100
4.4.4 Preliminary proof of the MCH property	101
4.4.5 The RSF mechanism.....	102
4.4.6 Proof of the RSF and the MCH property.....	103
4.4.7 Surface wetting properties and the RSP theory	109
4.4.8 Visualization of water penetration status	112
4.4.9 Anti-adhesive application (MCH-SMHs).....	119
Summary and Outlook	121
References.....	127
Curriculum Vitae	143

Abbreviations¹

1D	One-dimensional
2D	Two-dimensional
3D	Three-dimensional
AR	Aspect ratio
CA	Contact angle
CLSM	Confocal laser scanning microscope
CVD	Chemical vapor deposition
DAGS	Droplet-Assisted Growth and Shaping
DCMVS	Dichloromethylvinylsilane
d-DAGS	dynamic Droplet-Assisted Growth and Shaping
DMF	<i>N, N</i> -dimethylformamide
DMPA	2,2-dimethoxy-2-phenylacetophenone
EDX	Energy-dispersive X-ray spectroscopy
EE-SNRs	ETCS-ETCS bamboo-shaped SNRs
EEV-SNRs	ETCS-ETCS-VTCS bamboo-shaped SNRs
Eq.	Equation
ETCS/E	Ethyltrichlorosilane
ETCS-SNRs	Ethyltrichlorosilane based SNRs
EtOH	Ethanol
EVE-SNRs	ETCS-VTCS-ETCS bamboo-shaped SNRs
EV-SNRs	ETCS-VTCS bamboo-shaped SNRs
FT-IR	Fourier-transform infrared spectroscopy
HAADF	High angle annular dark field detector
MB	Methylene blue
MCH	Multi-component hybrid
MTCS	Trichloromethylsilane

¹ In alphabetical order.

MW	Molecular weight
NH ₂ @SNRs	Cysteamine clicked SNRs
Ninhydrin	2,2-dihydroxyindane-1,3-dione
n-seg-ETCS-SNRs	ETCS based bamboo-shaped SNRs with n segments
PDMS	Polydimethylsiloxane
PI	Photo-initiator
<i>RH</i>	Relative humidity
RSF	Region-selective functionalization
RSP	Region-selective protection
<i>RT</i>	Reaction time
S.D.	Standard deviation
SC	Single-component
seg	Segments
SEM	Scanning electron microscopy
SH@SNRs	1,4-Butanedithiol clicked SNRs
SNFs	Silicone nanofilaments
SMHs	Silicone micro-hoodoos
SNRs	Silicone nanorods
SNTs	Silicone trees
STEM	Scanning transmission electron microscopy
TEM	Transmission electron microscopy
UV	Ultra-violet
UV-Vis	Ultra-violet visible
<i>VOL</i>	Volume of precursor
VTCS/V	Trichlorovinylsilane
VTCS-SNRs	Trichlorovinylsilane based SNRs
WCA	Water contact angle
WD	Water droplet
WSA	Water sliding angle

List of Symbols

Physical Constants

Gravitational acceleration $g = 9.806 \text{ m}\cdot\text{s}^{-2}$

Universal gas constant $R = 8.314 \text{ 51 J}\cdot\text{mol}^{-1}\cdot\text{K}^{-1}$

Symbols¹

A	area	m^2
d	diameter	m
F	force	N
h	height	m
l	length	m
m	mass	kg
M	molar mass	$\text{kg}\cdot\text{mol}^{-1}$
P	pressure	Pa
r	roughness factor	non-dimensional
S	fog capture area	m^2
t	time	s
T	temperature	$^{\circ}\text{C}$
WCR	water collection rate	$\text{g}\cdot\text{m}^{-2}\cdot\text{h}^{-1}$
We	weber number	non-dimensional
α	tilt angle	$^{\circ}$
γ	surface tension	$\text{N}\cdot\text{m}^{-1}$
θ_{CA}	contact angle	$^{\circ}$
θ_{WCA}	water contact angle	$^{\circ}$
θ_{WSA}	water sliding angle	$^{\circ}$
λ	wavelength	nm
v	velocity	$\text{m}\cdot\text{s}^{-1}$

¹ Non-standard SI units used throughout the text are given in parentheses.

1. Introduction

Design and synthesis of micro- and nanomaterials with desired specific physical, chemical, and mechanical properties and performance characteristics have attracted remarkable attention from science and industry. In the past decades, numerous nano-engineering techniques have been developed to maximize design freedom, and countless real-life applications were bound to nanotechnology. As one of the crucial subjects of nanoengineered surfaces and interfaces, the fabrication of solid surfaces featuring unique functionalities, for example, waterproofing[1-3], water-harvesting[4], self-cleaning[5-7], protein adsorption[8], drug release and delivery[9], oil-water separation[10], and catalyst immobilization[8, 11], has been found indispensable in various practical scenarios. Among numerous materials used in nanotechnology and surface science, silicone-based nanomaterial is considered one of the most popular types. Benefiting from multifaceted functions and unique physicochemical properties, such as oxidative stability, chemical inertness, and thermal properties[12], 1D-SNFs, since their discovery by the Seeger group more than a decade ago[1], the development of their fabrication, modification, and applications have never been stopped.

SNFs have been reported to be produced at room temperature via either liquid or gas phase chemical synthesis methods[1, 13]. Most substrate materials can be coated after appropriate surface activation treatment[14-16]. The engineered substrate surfaces are generally characterized by low-surface-energy and high roughness at micro- and nanometer scales[12, 17]. Diverse applications, such as oil-water separation[10], support for oxygen evolution catalysts[18], water disinfection[19], and anti-icing[20], have been extensively investigated.

However, the conventional SNFs coating faces enormous challenges for the following reasons: *(i)* High surface roughness is typically caused by highly entangled irregular SNFs networks, whereas a single SNF structure may have tens of microns in length but with a curved and messy morphology. Therefore, precise control over surface coating thickness and uniformity is hardly achieved; *(ii)* SNFs are fragile and susceptible to

mechanical damage[5], such as linear abrasions, cyclic abrasions, and finger wiping. Developing the mechanical stability of soft silicone materials remains a formidable challenge. (iii) most silicone-based micro- and nanostructures are made of single chemical composition with intrinsic hydrophobicity and inert chemical properties. Non-reactive functional groups are typically exposed on the surface of the formed structures, such as alkyls[12] and perfluoroalkyls[21]. Harsh conditions are normally required for their further chemical modifications.

Even though the DAGS mechanism has been proposed for explaining the in situ growth pattern of various shapes of silicone-based materials, such as filaments, rods, volcanoes, chalices, tubes, and helices[22], further development of silicone-based micro- and nanostructures requires a deeper understanding and expansion of the mechanism in terms of structural optimization[23]. In addition, enhancing the degree of freedom in the design of nanomaterials should not only focus on structural design but also consider chemical composition adjustment and the possibility of further surface chemical modifications. Therefore, from the mechanism of synthesizing silicone-based nanostructures to their morphological-design, chemical functionalization, effects on surface physicochemical properties, and practical applications, many aspects of silicone-based nanomaterials are still waiting to be explored.

The scope of this thesis centers around refining and expanding the DAGS mechanism and using it as a basis for further development of silicone-based nanostructures bearing desired specific physicochemical and mechanical properties. Meanwhile, related studies, such as chemical functionalization on the synthesized nanostructures, wetting properties of the nanoengineered solid surface, and practical applications of the obtained samples, were also conducted. The aims of each chapter are as follows:

- Chapter 4.1: investigate the roles of the synthetic parameters in the growing and shaping process of the silicone nanostructures via the gas phase method.

The gas phase chemical synthesis method, the so-called CVD method, was used in this thesis because it is facile, efficient, low-cost, solvent-free, and environmentally friendly[23-25]. Previous studies[26] have revealed that basic synthetic parameters, such as T , absolute water amount, RH , and the precursor and substrate types, can collectively affect the geometric properties of the synthesized silicone-based micro- and nanostructures. In this chapter, a series of fundamental experiments were designed and

performed to evaluate the combinations of different synthetic parameters, including *RH*, *RT*, *VOL*, and substrate and precursor types. Other factors remained constant. Notably, only single-component nanostructures, considered homogeneous in chemical compositions, were synthesized and analyzed. SEM was used for morphological characterizations.

- Chapter 4.2: discover the practical applications of the newly synthesized ETCS-based SNRs.

To expand the practical applications of the newly synthesized ETCS-SC-SNRs, investigations on the cellulosic-paper-based substrate were conducted. In recent years, complicated and costly synthesis processes, limitations in mass production, and adverse effects on the environment due to organic solvents have become the main obstacles for the real-world applications of waterproof cellulosic paper[25]. Simultaneously achieving anti-wetting properties, printability, writability, well-readability, and enhanced mechanical stability on the cellulosic paper surface remains a technique challenge. The cellulosic paper has intrinsic hydrophilic properties because of the monosaccharide building units and poor mechanical strength after contact with water[27, 28]. Most surface-engineering strategies, such as photolithography[2], chemical etching[29, 30], and nanoparticulate deposition[31-33], can hardly be applied on cellulosic-paper-based substrates because of the undesired damages from unignorable thermal or wet-chemical treatments[34]. With the development of the ETCS-SC-SNRs, a non-solvent strategy to adopt the cellulosic-paper-based substrate, a micro-nano hierarchical morphology, is developed. The functionalities of the ETCS-SC-SNRs decorated samples, including waterproofing, self-cleaning, and antimicrobial properties, were examined in this chapter.

- Chapter 4.3: characterize the novel bamboo-shaped SC-SNRs, understand and improve their synthesis mechanism, i.e., d-DAGS mechanism, and explore their potential applications.

In order to overcome the vulnerability and irregularity of the nanostructures synthesized using silicone-based materials with inherent soft mechanical property, the specially designed bamboo-shaped SC-SNRs are produced via the d-DAGS method[23]. The repetitive dynamic regulation of synthetic parameters, concomitant with the periodic flushing and injection of silanes, has resulted in the formation of the highly-regular and

morphological-controlled bamboo-shaped SC-SNRs with a specific number of segments. Geometric parameters of the surface coatings are considered significant to surface wetting properties[35-37], the height of the synthesized bamboo-shaped structures, i.e., the thickness of the surface coating because of the uniformity of the formed structures, can be effectively tuned by arranging a different number of segment units. From 1 to 6, the well-structured ultra-long rods with 12 and 18 segments have been successfully fabricated. From hydrolysis and condensation reactions of the trifunctional silanes to the polysiloxane deposition process and the growing and shaping procedures of the bamboo-shaped structures, almost all details have been discussed in the studies of the d-DAGS mechanism. Compared to the conventional SNFs, the bamboo-shaped ETCS-SC-SNRs exhibited enhanced mechanical stiffness and chemical durability and excellent performance in promoting buoyancy and self-cleaning. The water-harvesting capability of the silicone-based structures, which has rarely been reported in other research, is particularly investigated in this chapter to solve the incessant water-scarcity problem caused by rapid population growth, over-consumption, environmental pollution, and global climate change[38-40].

- Chapter 4.4: develop MCH silicone-based nanostructures via the d-DAGS method and feature them desired site-specific physicochemical properties via the chemical modification method.

Based on the optimized d-DAGS mechanism, the heterogeneous multi-component hybrid (MCH) material with the desired site-specific physicochemical properties has been developed and analyzed in this chapter. The term heterogeneous indicates the difference in the chemical composition of different parts of the synthesized MCH nanostructures. With increasing material demands from the real world, developing more complicated and functional materials, from which the functional parts or specific properties can be intelligently allocated to the neediest positions, has been of great interest for many years[41-44]. Commonly used additive manufacturing methods, for example, fused deposition modeling[45, 46], laser engineered net shaping[47], and selective laser melting[48, 49], are either more suitable for metal substrates or hindered by inferior properties and processing issues on polymers[50]. Benefiting from the independent growth of each segment via the d-DAGS method, different precursors are used in synthesizing polysiloxanes, and the corresponding surface physical and chemical properties can therefore be tuned on-demand.

2. Theory and Background

2.1 Silicone chemistry

2.1.1 General aspects

Silicone, also known as polysiloxane or polyorganosiloxane, refers to a kind of mixed organic-inorganic polymer family that is made up of siloxane, namely, silicone-oxygen backbone (Si-O-Si) or network, with branched or unbranched chains. As a literal combination of the terms “silicon” and “ketone”, the expression “silicone” was coined by Kipping in 1901, whereas silicone chemistry started to bloom in the 1940s due to the Müller–Rochow synthesis of organochlorosilanes on an industrial scale[51, 52]. Based on the molecular weight and degree of crosslinking, siloxanes with macromolecular structures – highly crosslinked structures - are classified as polymers, whereas the ones with low molecular weight, e.g., trimers, tetramers and oligomers, usually exist as silicone fluids[53]. Today silicone polymers are widely used in our daily life because of their multifaceted functions as well as unique intrinsic physicochemical properties, for example, oxidative stability, chemical inertness, thermal and environmental stability, low toxicity, flexibility, biocompatibility, low flammability, and anti-adhesive properties[52, 54-57].

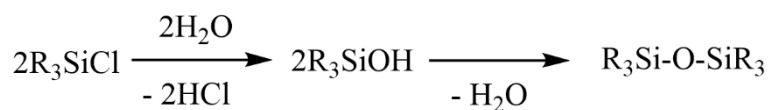
These properties and benefits of polysiloxanes can be explained by their structural characteristics. C-O bond is often selected and analyzed as a comparison. Si-O bonds are considered covalent and polar (more polarized than the C-O bond) but not fully ionic according to the electronegativity difference between the silicon and oxygen elements (Si: 1.74, O: 3.50, and C: 2.50)[58, 59]. Although the Si-O bond is reported to be longer than the C-O bond (1.63 Å¹ to 1.54 Å)[60, 61], it has a bigger bond strength (452 kJ·mol⁻¹) than the C-O bond (358 kJ·mol⁻¹)[62], plus the strong silicone bonding caused by the high polarity, eventually resulting in the good stability and chemical

¹ Å, angstrom, is a Non-standard SI metric unit of length equal to 10⁻¹⁰ m.

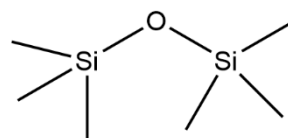
inertness of the silicone products, for example, the degradation temperature of PDMS in N₂ atmosphere is bigger than 300°C[34]. Compared to the bond angle of the C-O-C bond (111°)[63], a much larger value can be found in the Si-O-Si bond (142°)[64], which indicates that the polymers based on the Si-O-Si backbone are much more flexible than the one based on carbon. In addition, the high flexibility of the polysiloxanes contributes to easier shielding and protection[65]. When the nonpolar hydrophobic organic groups, e.g., methyl, locate on the Si-O-Si chain, that can efficiently shield the main chain and weak the intermolecular interactions, leading to the silicone configuration with the organic groups pointing outside, eventually resulting in the low surface tension of polymer materials[65]. With a low rotation barrier, more configurations can be adopted on the Si-O-Si chain; a good example is that the smaller rotation energy of the Me₂Si-O bond (3.3 kJ·mol⁻¹) than the H₂C-H₂C bond (13.8 kJ·mol⁻¹) in polyethylene contributes to a nearly free rotation[65].

2.1.2 Synthesis of polysiloxanes

The production of silicone polymer materials is typically started from the monomer of organo-substituted silanes with the general formula R_nSiX_(4-n), where R represents the organic residue, and X is the hydrolysable group, e.g., alkoxy, acyloxy, and halogen. Functional-chlorosilanes, as one of the most important precursors for silicones, are generally thermally stable but react quickly with water or other oxygen-moiety-containing reagents to generate the intermediate products – silanols or siloxanols – and further condensate to form the respective polysiloxanes (**Figure 2.1.1**), so-called the hydrolysis and condensation reactions.[22, 23, 53, 59].



For R = Me:



hexamethyldisiloxane

Figure 2.1.1: A simple sample of synthesizing siloxanes. Adapted with permission from[59].

Functional-chlorosilanes are considered to have four different types based on the number of chlorine atoms (hydrolysable groups) on the central silicon atom, which are M (R_3SiCl), D (R_2SiCl_2), T ($RSiCl_3$), and Q ($SiCl_4$), where R = organic moiety, as shown in **Figure 2.1.2**[57]. The reactivity of the precursors and the properties of the formed polysiloxanes are significantly influenced by the substituents on the silicon atom[53]. Adding crosslinkers to the polysiloxanes either in their initial polymerization process or later with reactions to the side or end groups can also affect the characteristics of the final products[53].

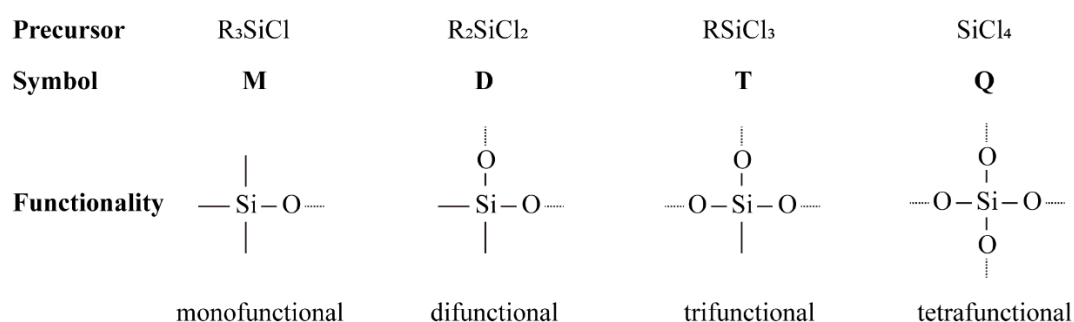


Figure 2.1.2: Polysiloxane building blocks, where R = organic moiety.

As mentioned above, two main steps are involved in the synthesis of polysiloxanes: (1) hydrolyzation of hydrolysable group X of the silane $R_nSiX_{(4-n)}$ to produce intermediate silanols; (2) subsequent condensation reactions to form the polysiloxanes. It still lacks clear clues of the sequence and kinetics of all possible reactions in the above steps, so both homo- and heterofunctional condensation reactions might occur[12, 66]. The intermolecular condensations can be catalyzed by either acid or base[67]. As the product of the hydrolyzation of hydrolysable group X is HX, when chlorosilanes are used as a precursor, byproduct hydrochloric acid is produced and inversely catalyzes the reactions[23]. Therefore, the whole procedure is somehow self-catalytic[22].

Depending on the degree of functionality of different precursors, they may contribute to different types of polysiloxanes:

- (1) Monofunctional silanes can work as the terminator to control the chain length in polycondensation reactions;
- (2) Difunctional silanes can be used to produce linear polyorganosiloxanes and cyclic diorganosiloxanes, which are considered the two most important siloxanes in research and industry[59]. For example, PDMS (**Figure 2.1.3**), due to their excellent stability

and physicochemical properties, have been widely used in lubricants, rubbers, resins, oils, etc.[57, 68]. Although cyclic dimethylsiloxanes have many overlap applications with PDMS, they can be specially used in cosmetics and personal care products[69].

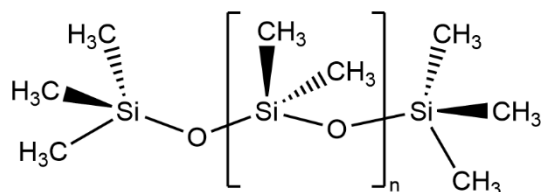
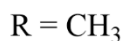
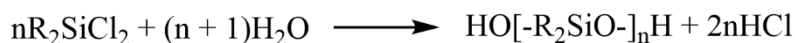


Figure 2.1.3: Reactions and chemical structures of PDMS.

(3) Tri- and tetrafunctional silanes can form polysiloxanes with more complicated structures because of their ability to crosslink. Whereas the product of trifunctional silanes, Silsesquioxanes, with the general formula $(RSiO_{3/2})_n$, are considered a subspecies of polysiloxanes and frequently used as protective or functional coatings in different substrates, such as electronic and optical devices, glass, wood, and fibers[12]. The reactions to synthesize polysilsesquioxanes are given in **Figure 2.1.4**, whereas the overall reaction is based on the assumption of complete condensation[12]. However, it has been evidenced that the complete condensation of all hydroxyl groups cannot happen, as seen in silicone resins[4, 66]. A general formula of polysilsesquioxane, $[RSiO_x(OH)_{3-2x}]_n$, where $0 < x < 3/2$, is used assuming complete hydrolysis.

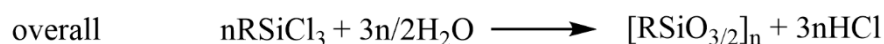
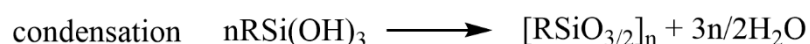
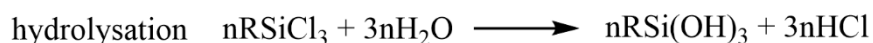


Figure 2.1.4: Reactions to form polysilsesquioxanes.

2.1.3 Surface silylation and chemical structures of silsesquioxanes

According to the chain length and the size of substituents on the silicon atom, different types of polymerizations can be observed, such as horizontal, vertical, and bulk polymerizations[70, 71]. As one of the most widely used applications of polysiloxanes, surface modification – to alter the surface energy, roughness, and wetting properties, has been of great interest for many years. Many mono-, di-, and trifunctional silanes

have been successfully loaded on the hydroxyl groups containing substrate surfaces in various pathways, namely surface silylation (**Figure 2.1.5**)[70], different types of substrates, such as silica[72-74], metal (germanium, titanium, and aluminium)[16, 73, 75], polyester[15, 76], textiles[15], and glass[4, 14, 77], can be used after pretreatment.

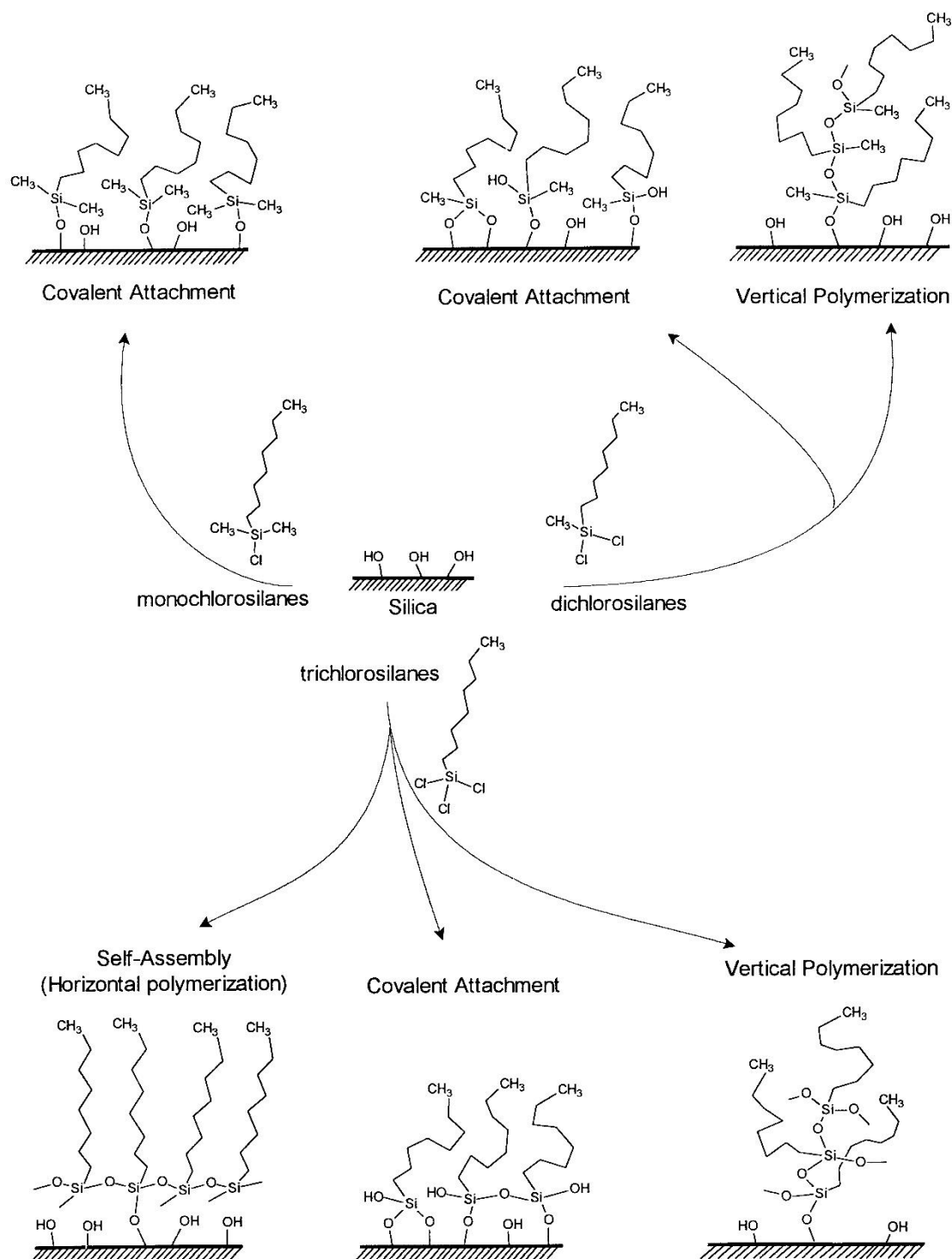


Figure 2.1.5: Surface silylation on hydroxyl groups containing silica surface. Reprinted with permission from[70].

Notably, as shown in **Figure 2.1.5**, trifunctional silanes are more reactive than their monofunctional analogs and are able to conduct polymerizations in the presence of water, leading to various surface architectures, including covalent attachment, self-assembly (2D), and surface-induced polycondensation (3D)[70]. As illustrated in **Figure 2.1.6**, silsesquioxanes can adopt different chemical structures depending on the reaction and curing conditions, including well-defined 3D polyhedral cage structures (size may be different), partial cage structures, polymeric 2D ladder structures, and random structures[55, 78-80].

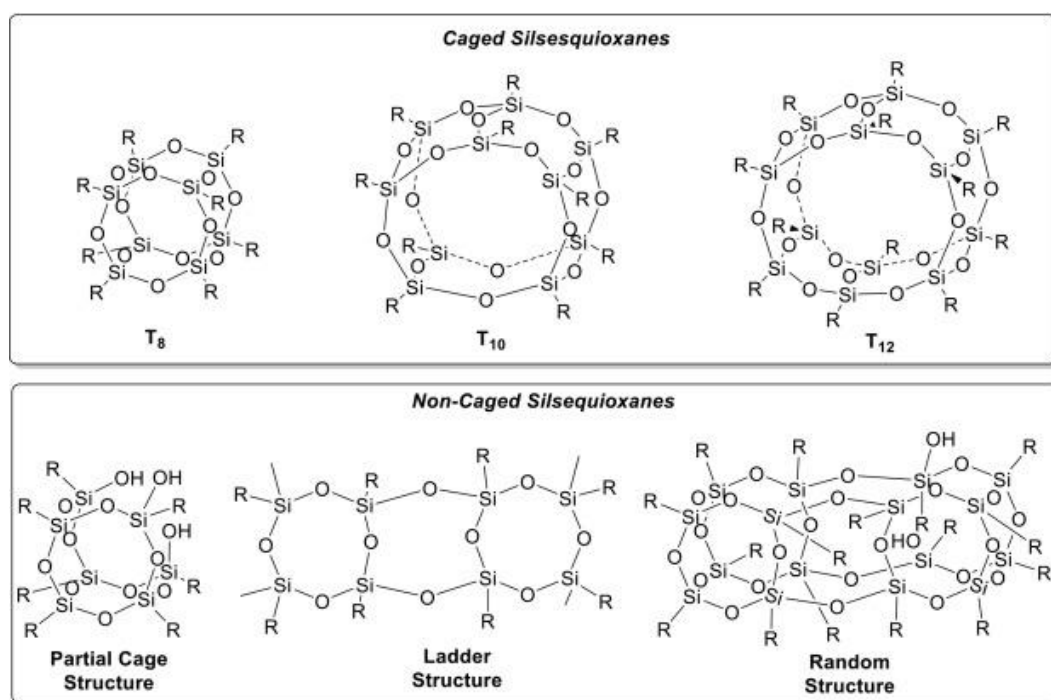


Figure 2.1.6: Structural variation of silsesquioxanes. Reprinted with permission from[78].

2.1.4 Silicone-based micro- and nanomaterials

Despite widespread application of different types of polysiloxanes, little has been investigated about the characteristics of the material at the nanometer scale[12]. Silicone-based 1D nanoparticles, for example, filaments, tubes, wires, and fibres, which are synthesized via the template-free method, have been developed only since the beginning of this century[81, 82]. Subsequently, many studies have been conducted on developing silicone-based micro- and nanomaterials with different physical, chemical, and mechanical properties and different functionalities. As the examples shown in **Figure 2.1.7**, different shapes of silicone-based micro- and nanomaterials, such as stars,

helices, filaments, volcanos, chalices, and tubes, have been reported[22].

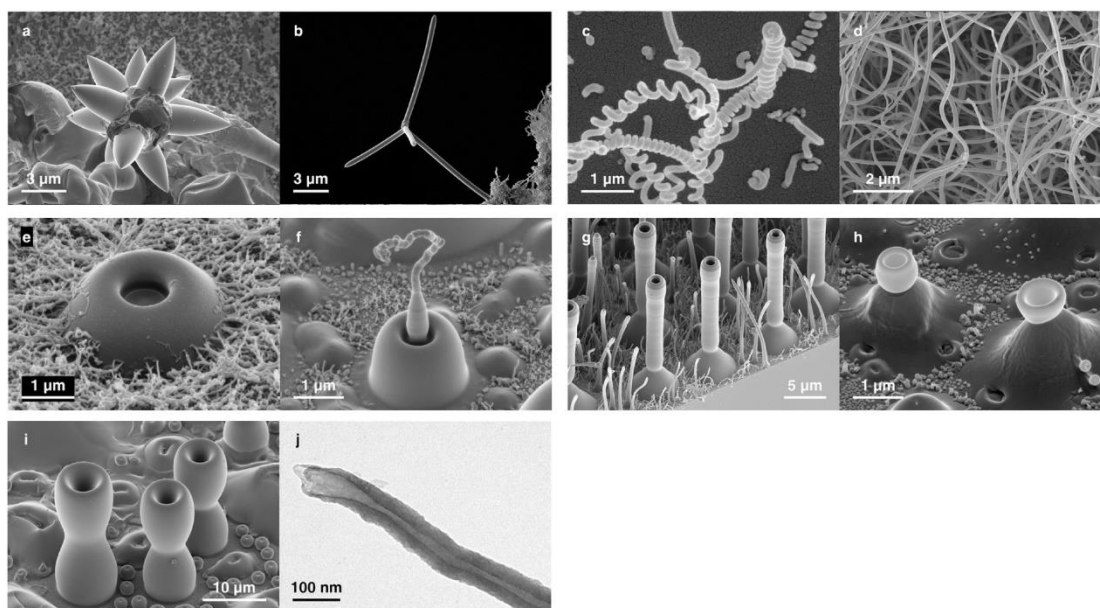


Figure 2.1.7: SEM images of (a, b) stars. (c) helices. (d) SNFs. (e) volcanoes. (f) SNF on top of a volcano. (g) rods. (h) chalices on top of a volcano. (i) chalices. (j) TEM image of a silicone nanotube. Adapted with permission from [22].

2.1.5 Fabrication methods and mechanisms

Various methods have been developed and successfully applied in fabricating and tuning the micro- and nano-roughness and morphology of decorated structures for decades, for example electro-spinning and electro-spraying[83, 84], electrochemical deposition[85, 86], the sol-gel method[87], wet-chemical method[88, 89], lithography[35, 90, 91], chemical vapor deposition[92]. However, most of these methods either work on metallic materials or lack precise control over the structures formed on the substrate surface. Promising methods used in fabricating regular micro- and nanostructures, for example, chemical etching and lithography, are hindered in widespread adoption because of their unignorable drawbacks, such as the requirement of harsh conditions, use of hazardous materials, chemical waste production, and high cost[93, 94].

As for the silicone-based materials, depending on whether solvents are used, the known methods for synthesizing micro- and nanostructures can be roughly classified into two groups: liquid phase synthesis method and gas phase synthesis method[12]. Compared

to the liquid phase synthesis method, which requires the presence of organic solvents, such as toluene[95], trimethylamine and methanol[96], ethanol[97], and various other solvents[13], the gas phase synthesis method, typically including the techniques of “top-down” (physical deposition) and “bottom-up” (chemical deposition), is widely favored due to the advantages such as solvent-free[24], zero liquid waste[25], and accessible scale-up properties[98]. This thesis aims to discuss and develop the chemical-based gas phase synthesis method based on the previous studies in Seeger’s group.

Pretreatment

As previously mentioned, many different types of substrate materials (**Figure 2.1.8**) can be used in silicone-based surface coating after specific surface pretreatment – to produce or add hydroxyl groups on the substrate surface. These pretreatment methods consist of

- Liquid treatment – activate the solid surface by using solvents, strongly oxidizing liquid, cleaning solutions, or alkaline with or without the help of ultrasonication[1, 4, 75, 77, 99];
- Plasma treatment – use oxygen or the mixture of oxygen and hydrogen as process gas[72, 73, 82, 100, 101];
- UV-light[7].

Sometimes, more than one method is used in the retreatment process[100].

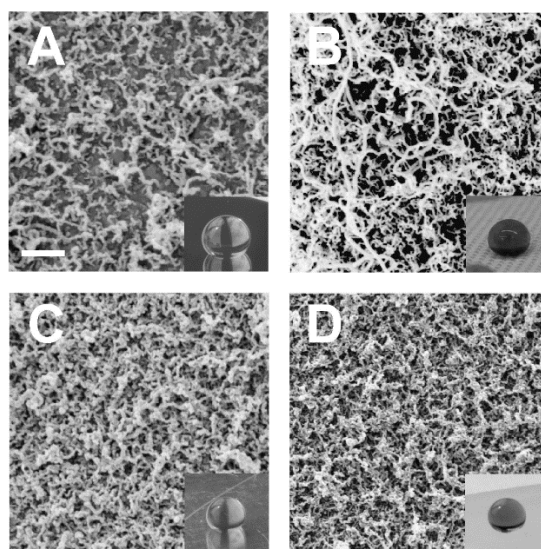


Figure 2.1.8: SEM images of SNFs on (a) silicon, (b) cotton, (c) aluminum,

and (d) PDMS substrates. Insert is the picture showing a water droplet sitting on the respective coating surface. Scale bar, 200 nm. Reprinted with permission from[14].

Synthesis in the gas phase

Unlike the physical deposition methods, which do not consist of any chemical reactions during the product forming and shaping process, the synthesis of silicone-based micro- and nanomaterials via the chemical vapor deposition method is dependent on the reactions between gaseous water and reactive silanes at room temperature and normal pressure inside the coating environment[1, 72, 100]. Commonly used silanes include MTCS, VTCS, ETCS, or a mixture of different silanes[15, 72, 102]. Similar procedures (**Figure 2.1.9**) have been reported from different studies that the reactions are triggered by the evaporation of the volatile silanes in the reaction atmosphere[1, 102] or by exposing the substrate to the coating environment[72]. Prior to the reactions, the reaction atmosphere is created by loading the necessary amount of water via methods such as flushing the moisture gas[1], evaporation of water[73], and using residual surface-adsorbed water[102].

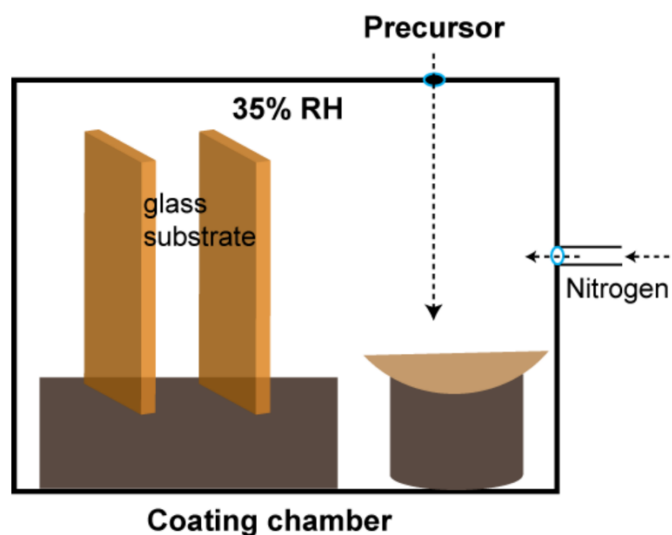


Figure 2.1.9: Schematic illustration of CVD method. Adapted with permission from[103].

DAGS mechanism

Many mechanisms have been developed to explain the growth mode of the silicone-based 1D nanomaterials, such as composition-based mechanism[4], surface-curvature-based mechanism[72], and diffusion-based mechanism[73], whereas the droplet

assisted growth and shaping (DAGS) mechanism[22] is considered a reasonable explanation to the room temperature processing and polymerization reactions of trifunctional silanes.

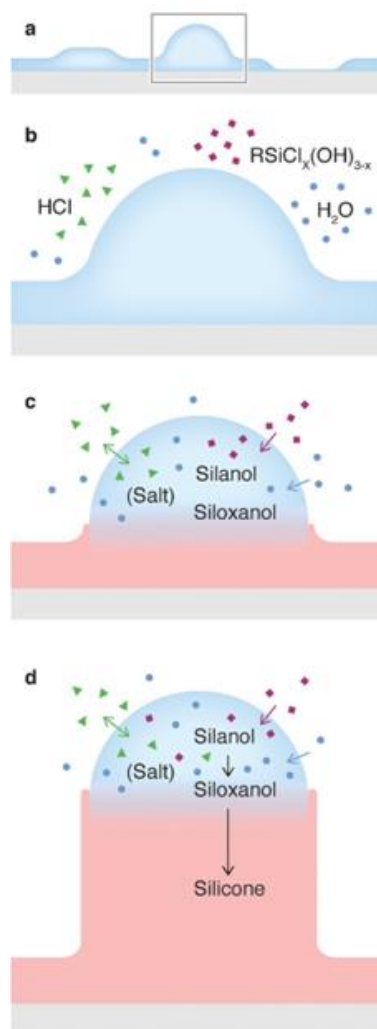


Figure 2.1.10: Illustration of the DAGS method. (a) water layer condensed on the substrate surface. (b) tiny water droplet increases into reaction volume through equilibrating with gases from the neighboring environment. (c) hydrolysis and condensation reactions in the water droplet to form the polysiloxanes. (d) deposition of insoluble silicone and growth of silicone-based nanostructure. Reprinted with permission from[22].

As shown in **Figure 2.1.10**, the DAGS method[22] demonstrates that the growth of 1D silicone-based nanomaterials starts from the formation of tiny water droplets on the substrate surface because of structural and chemical inhomogeneity after loading the necessary amount of water into the reaction chamber (via moist N_2 gas)[104, 105]. Subsequently, with the addition of volatile precursors, evaporating functional silanes

are able to react with water in the gas phase to generate (mono)silanol and HCl. It is impossible to further hydrolysis to (di- or tri-)silanols because the silanol is much harder to hydrolysis than the functional silanes. Soluble reactants and products (water, HCl, silanol, and chlorosilanes) are attracted and dissolved into the superficial tiny water droplets on the substrate surface, reducing water droplet activity and further hydrolysis and condensation reactions. Water droplets can be replenished from the surrounding gas phase because of the thermodynamic equilibration to guarantee that the reaction continues. Eventually, the polysiloxane is formed in the condensed water droplet, which is acting as the spatially confined reaction vessels, and further deposits at the liquid-solid interface result in the growth of 1D silicone-based micro- and nanostructures.

Reaction parameters

Systematic parameters, such as T , absolute water amount, RH , RT , and the precursor and substrate types, collectively affect the product morphologies, thereby influencing the surface roughness and physicochemical properties[26]. Based on different combinations of reaction parameters, different shapes of silicone-based structures can be obtained; for example, as shown in **Figure 2.1.11**, by changing the RT and T , various micro- and nanostructures are presented.

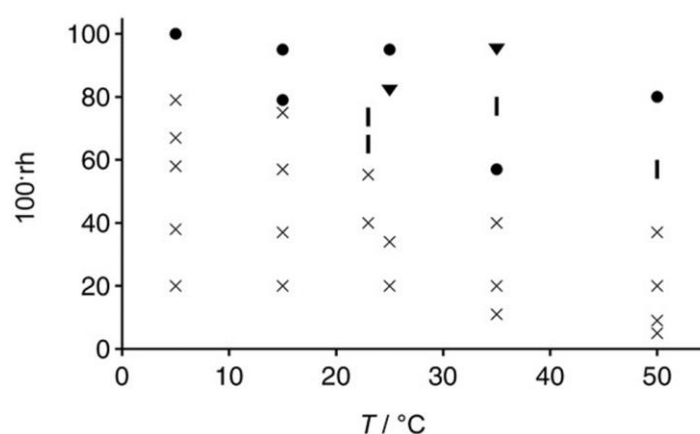


Figure 2.1.11: the obtained ETCS-based silicone micro- and nanostructures as a function of RH and T . ● : volcanoes, ▼ : chalice, × : SNFs and Rods.

Reprinted with permission from[22].

Notably, the parameters RH and VOL mainly affect the ratios between n_{silane} and n_{water} . The calculation of $n_{\text{silane}}/n_{\text{water}}$ is based on the assumption of ideal gas behavior, the

Arden Buck equation[106] is used to calculate the saturation pressure of water vapor P_s (in kPa) at the given temperature T (in Celsius).

$$P_s(T) = 0.61121e^{(18.678 - \frac{T}{234.5})(\frac{T}{257.14 + T})}$$

At a given RH, the corresponding pressure P_c can be calculated by:

$$P_c = P_s \cdot RH$$

The n_{water} is then obtained in equation:

$$n = \frac{P_c V}{RT}$$

Where V is the volume of reaction chamber (in L).

2.1.6 Chemical modifications

In order to further extend and improve the design, synthesis, and applicability of the silicone-based micro- and nanomaterials, from morphology control[107, 108] to chemical modifications[19, 109, 110], various methods have been developed and attempted. As the geometrical parameters of the formed structures can be tuned during their growing process by adjusting the reaction parameters, further chemical modifications are considered the only way to change the physicochemical properties of the formed silicone-based structures. For example, oxidation treatment, which includes annealing[102], calcination[4], and various plasma treatment methods[77, 100, 111], enables to change the hydrophobic/superhydrophobic silicone-based functional surface coating to be superhydrophilic with θ_{WCA} close to 0° with or without affecting the initial morphologies. Moreover, the oxidized samples, which are usually decorated with hydroxyl groups, can be further modified by conducting chemical reactions with, for instance, 1H,1H,2H,2H-perfluorooctyltrichlorosilane[100, 101, 111], 1H,2H,2H-perfluorodecyltrichlorosilane[112], and titania nanoparticles[5, 113].

Besides the above oxidization methods, the photoinitiated thiol-ene click reactions are also reported to modify the surface chemical properties of the silicone-based materials that bear vinyl groups[110, 114-116]. As shown in **Figure 2.1.12**, the detailed radical-mediated thiol-ene click reaction mechanism demonstrates that[117]:

- Step 1: A radical initiator abstracts the H from the thiol molecule under thermal

or illumination conditions. This step produces a highly reactive thiyl radical $R_1-S\cdot$, which can attack the alkene groups ($R_2CH_2=CH$).

- Step 2: The formed carbon-centered radical ($R_1SCH_2C\cdot HR_2$) can also abstract the H from a R_1-SH molecule. This step is deemed an amplification step as the single thiyl radical leads to a series of chemical attacks, similar to the chain-growth free radical polymerizations.

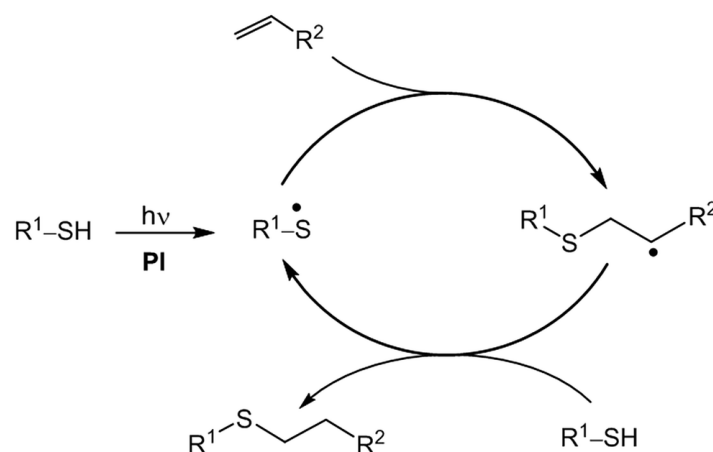


Figure 2.1.12: Scheme of the photochemical radical-mediated thiol-ene click reaction mechanism. Reprinted with permission from [117].

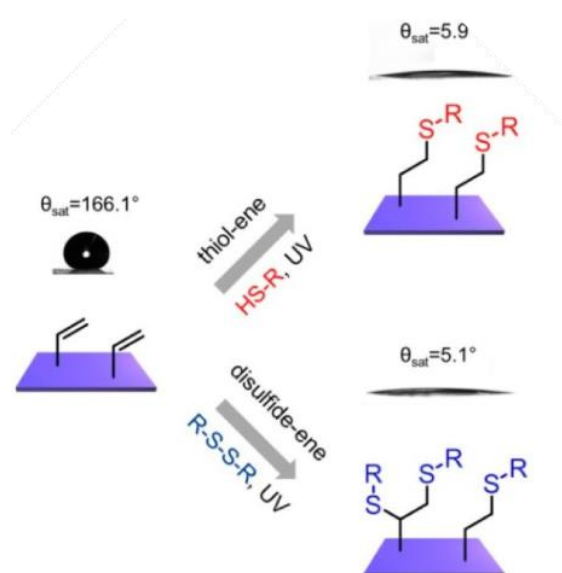


Figure 2.1.13: Schematic illustration shows that (top) thiol-ene click reaction of the VTCS-based surface coating with cysteamine and (bottom) disulfide-ene reaction with 3,3-dithiodipropionic acid. Adapted with permission from [110].

As illustrated in **Figure 2.1.13**, Li et al.[110] reported the successful functionalization of the VTCS-based SNFs structures with different thiol derivatives under 260 nm UV light for 15s, resulting in the change of surface wetting properties from superhydrophobic to superhydrophilic. Similarly, Wang et al.[114] (**Figure 2.1.14**) also reported the same thiol-ene click modifications based on the reactions between VTCS-based SNFs and the sulfobetaine under a 365 nm UV light for 10 min at room temperature with the help of photoinitiator DMPA. Various practical applications have been tested after the chemical modifications on the VTCS-containing silicone-based micro- and nanomaterials.

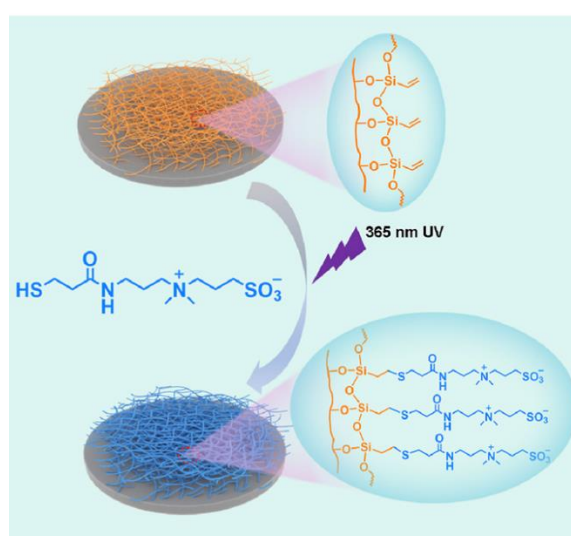


Figure 2.1.14: Thiol-ene click reactions on the VTCS-based SNFs with sulfobetaine. Adapted with permission from[114].

2.1.7 Applications

One of the most important reasons the silicone-based micro- and nanomaterials have attracted extensive attention is their multifunctionality. Many different practical applications of silicone-based materials have been widely reported. For example:

- Superhydrophobic: silicone-based micro- and nanostructures as a functional coating on the solid surface enable the reduction of the surface energy (depending on the functional groups) and increase the surface roughness, therefore leading to the superhydrophobic surface properties.[5, 12, 14, 15, 23, 24, 81, 95, 101, 112, 118]
- Oleophobic/superoleophobic: chemical modifications on the silicone-based

micro- and nanomaterials with some fluorine-containing chemicals, for example, 1H,2H,2H-perfluorodecyltrichlorosilane and 1H,1H,2H,2H-perfluorooctyltrichlorosilane, enables to improve the oil repellency of the surface coating.[111, 112, 119]

- Oil/water separation: based on the above-mentioned superhydrophobic or oleophobic properties, silicone-based coatings are also used for separating water and oil.[76]
- Switchable wettability: switch between superhydrophobic and superhydrophilic properties of the silicone-based coatings via chemical modification methods.[77]
- Surface wetting patterns: by introducing the partial masks in surface chemical modifications, such as the photoinitiated thiol-ene click reactions, different patterns on the surface based on the wettability are obtained.[77, 110]
- Wettability gradients: similar to the surface wetting patterns, using the photoresist masking technique or hydrolysis of silicone-based materials in alkaline solutions, wetting gradients on the substrate surface are achieved.[14, 120]
- Data storage: based on the stabilized plastrons by hierarchically structured silicone materials, two Cassie-type wetting states (at micro- and nanoscale)[121] are detected and distinguished by optical means and are therefore considered as bistable logic states to store binary data.[122]
- Self-cleaning: the rolling-off droplets on the silicone-modified substrate surface can remove dirt and contaminants.[23, 24, 88]
- Water harvesting: SNFs-modified hydrophobic and superhydrophobic solid surfaces are used for water harvesting applications.[4]
- Protein adsorption: enhanced site-specific or non-specific immobilization of proteins on the 1D SNFs modified substrate surfaces compared to the flat ones have been widely reported.[8, 123]
- Catalyst immobilization: silicone-based micro- and nanostructures are considered excellent catalyst support because of their chemical stability, large surface area, and possibility of chemical modifications, etc.[5, 113, 124]

2.2 Wetting of solid surfaces

2.2.1 Homogeneous planar solid surface

Depending on whether the liquid droplet that is in contact with a solid surface tends to spread on the surface or stay compact, the words “wetting” and “non-wetting” are used, respectively. According to Young’s equation[125] (**Eq. 2.2.1**), the wettability of the ideal homogeneous planar solid surface can be described as (**Figure 2.2.1.a**):

$$\cos \theta = \frac{\gamma_{SV} - \gamma_{SL}}{\gamma_{LV}} \quad (\text{Eq. 2.2.1})$$

Where θ is the contact angle determined from the solid-liquid-vapor contact line (“three-phase contact line” or “triple-line”); γ_{SV} , γ_{SL} , and γ_{LV} represent the solid-vapor, solid-liquid, and liquid-vapor interfacial tensions, respectively.

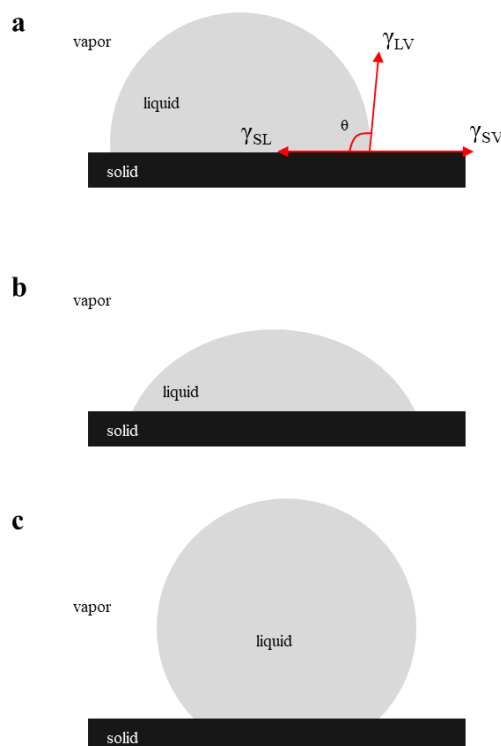


Figure 2.2.1: Scheme illustration of (a) the interfacial tensions at triple-line, (b) hydrophilic, and (c) hydrophobic surfaces.

Based on the fundamental relationships of the interfacial energies and the contact angle (shape) of the droplet (water) on the surface, the wettings of the solid surface can be classified as:

- complete wetting with $\theta = 0$ ($\cos\theta = 1$), where, $\gamma_{SL} + \gamma_{LV} = \gamma_{SV}$.
- Hydrophilic (**Figure 2.2.1.b**) with $\theta < 90^\circ$ ($\cos\theta > 0$), where $\gamma_{SV} > \gamma_{SL}$.
- Hydrophobic (**Figure 2.2.1.c**) with $\theta > 90^\circ$ ($\cos\theta < 0$), where $\gamma_{SV} < \gamma_{SL}$.

The reported highest θ_{WCA} on a fluorinated flat and homogeneous solid surface is $\sim 120^\circ$ [126, 127].

2.2.2 Rough and heterogeneous solid surface

Young's equation is no longer valid on the rough homogeneous (chemical) solid surface as the changes in the surface tension balance at the three-phase contact area (**Figure 2.2.2**).

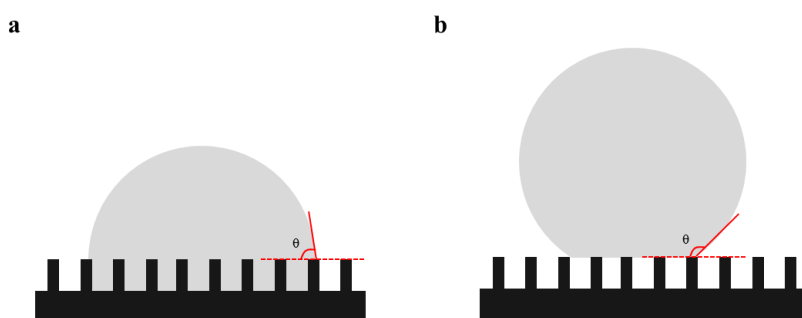


Figure 2.2.2: Schematic illustration of a droplet on a rough solid surface.

(a) Wenzel regime, (b) Cassie-Baxter regime.

By replacing the smooth surface in **Figure 2.2.1** with rough homogeneous surfaces shown in **Figure 2.2.2.a**, both unwetted and wetted areas of the surface have been increased by a roughness factor r [128]:

$$r = \frac{A_{actual}}{A_{smooth}} \quad (\text{Eq. 2.2.2})$$

Due to the surface tension of rough surface is related to smooth surface:

$$\gamma^* = r \cdot \gamma \quad (\text{Eq. 2.2.3})$$

Hence, the new balance of surface forces:

$$\cos\theta^* = r \cdot \cos\theta = r \cdot \left(\frac{\gamma_{SV} - \gamma_{SL}}{\gamma_{LV}}\right) \quad (\text{Eq. 2.2.4})$$

Eq. 2.2.4 is the so-called Wenzel equation, which relates the θ^*_{WCA} measured on a rough homogeneous solid surface to the θ_{WCA} defined on the flat surface.

In the case of the presence of two different materials (chemical compositions), so-called heterogeneous solid surface, for example, as shown in **Figure 2.2.2.b**, an air layer is enclosed in the cavities between liquid and solid, the mixed θ^{**}_{WCA} in this state can be calculated based on the Cassie-Baxter equation[36]:

$$\cos\theta^{**} = f_1 \cdot \cos\theta_1 + f_2 \cdot \cos\theta_2 \quad (\text{Eq. 2.2.5})$$

Where f_x and θ_x ($x = 1$ or 2 , and $f_1 = 1 - f_2$) represent the solid fraction and contact angle of the respective substance, in the Cassie-Baxter regime, one of the chemical components is air, and $\theta_{\text{air}} = 180^\circ$. Hence, the **Eq. 2.2.5** can also be written as:

$$\cos\theta^{**} = f \cdot \cos\theta + (1 - f) \cdot \cos 180^\circ = f \cdot \cos\theta + f - 1 \quad (\text{Eq. 2.2.6})$$

Conventionally, when a water droplet can maintain its spherical shape on the solid surface and easily roll off, the surface is defined as superhydrophobic with θ_{WCA} larger than 150° and θ_{WSA} less than 10° [121, 129, 130].

2.2.3 Intermediate wetting state

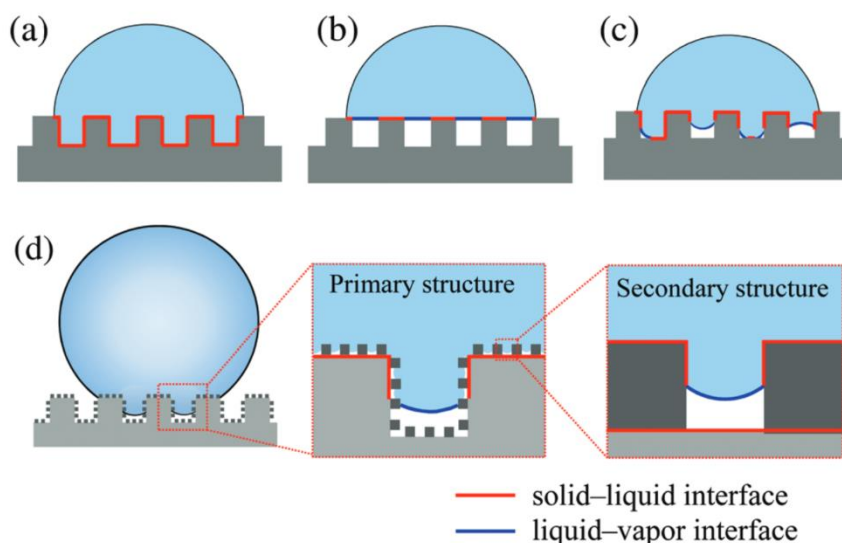


Figure 2.2.3: Schematics of the different wetting states: (a) Wenzel state, (b) Cassie-Baxter state, (c) partial wetting state for one-scale structured surface, and (d) partial wetting model for a dual-scale structured surface. Reprinted with permission from[131].

Considering the effect of physical geometries on wettability, the Wenzel state describes the liquid droplet penetrating the rough surface and fully wetting the substrate (**Figure 2.2.3.a**), and the Cassie-Baxter state indicates that the liquid droplet sits on the peak of rough surface (**Figure 2.2.3.b**)[36, 128]. However, the perfect Wenzel and Cassie-Baxter states are rare in real situations[132]. The mixed-wetting state, also known as the partial wetting state or intermediate state, exists between Wenzel and Cassie-Baxter states and is, therefore, developed and discussed in recent years[131, 133-136]. As shown in **Figure 2.2.3.c-d**, in 2019, Nagayama et al.[131] reported the theoretical partial wetting model via the thermodynamic energy minimization method and tested the model by conducting experiments on surfaces bearing different surface morphologies. In 2023, they reported a deeper understanding of the intermediate wetting state based on the surface free energy analysis[137], further verifying the suitability of this model for their fabricated Si surfaces from theoretical and experimental viewpoints.

3. Materials and Methods

3.1 Materials

3.1.1 Chemicals

The chemicals used throughout the project are listed in **Table 3.1.1**.

Table 3.1.1: List of Chemicals (in alphabetical order)¹.

Name	Specification	Supplier
1,4-butanedithiol	97%	Sigma-Aldrich
2,2-dimethoxy-2-phenylacetophenone	99%	Sigma-Aldrich
2,2-dihydroxyindane-1,3-dione	99%	Alfa Aesar
Acetone	≥ 99.8%	Merck Millipore
Atto 633-COOH	-	ATTO-TEC
BL21 Escherichia Coli strain	-	Life Technologies
Chloroform	≥ 99.5%	Sigma-Aldrich
Cysteine	~ 95%	Sigma-Aldrich
Deconex 11 universal	-	Borer Chemie AG
Dichloromethylvinylsilane	97%	Thermo Fisher GmbH
Ethanol absolute	-	Sigma-Aldrich
Ethyltrichlorosilane	99%	Sigma-Aldrich
Hydrochloric acid	37%	Sigma-Aldrich
Methylene blue	99.80%	Sigma-Aldrich
<i>N,N</i> -dimethylformamide	≥ 99.8%	Sigma-Aldrich
Rhodamine B	≥ 95%	Sigma-Aldrich
Sodium hydroxide	≥ 97%	Sigma-Aldrich
Tetrahydrofuran	≥ 99.5%	Sigma-Aldrich
Toluene	99.80%	Sigma-Aldrich

¹ Unless other specified, all chemicals were used as received without further purification.

Trichlorovinylsilane	97%	Sigma-Aldrich
----------------------	-----	---------------

All functional silane chemicals were stored and handled in the N₂-filled glove box to avoid undesirable reactions.

Water

Deionized water was from the lab's water line. Ultrapure Milli-Q water with a resistivity of 18.2 MΩ·cm produced by a Simplicity water purification system (Merck Millipore) was used throughout the project.

Detergent deconex solution¹

10% (v/v) aqueous solution of Deconex 11 universal was prepared and stored under ambient conditions for further use.

Ninhydrin solution

Ninhydrin dissolved in EtOH absolute (0.02 g·mL⁻¹) was stored in a lab refrigerator (4 °C) for further use.

Dye-containing water

Atto 633-COOH (M_w = 652 g·mol⁻¹) fluorescent dye dissolved in Milli-Q water (50 μg·mL⁻¹) was stored in a lab refrigerator (-20 °C) for further use.

3.1.2 Substrates

Glass substrate and activation

Microscopic glass slides (26 × 76 × 0.15 mm) and coverslips (1#) purchased from Menzel (Braunschweig, Germany) were used after the surface cleaning and activation process. The undesired dirt and other organic and inorganic contaminants on the surface of the received glass substrate must be removed to avoid possible adverse effects on the homogeneity and reproducibility of the silicone nanostructures. Therefore, for each time of cleaning and activation, 8 pieces of glass slides were placed upright in a glass staining jar filled with 10% (v/v) aqueous solution of detergent Deconex 11 universal. After ultrasonication at 37 kHz and 50 °C for 2 h, the glass slides were removed, thoroughly rinsed with Milli-Q water for several minutes, and dried by N₂-gun (nitrogen

¹ Deconex 11 universal is a mildly alkaline water solution (pH = 11) normally used as the surfactant.

gas flow). After the cleaning step, the glass surface was gently activated (hydroxyl groups loaded) by the alkaline Deconex solutions, an indicator is that the surface can be thoroughly wetted¹ as shown in **Figure 3.1.1**. All cleaned and activated glass slides were stored in a clean plastic slide container for further use.

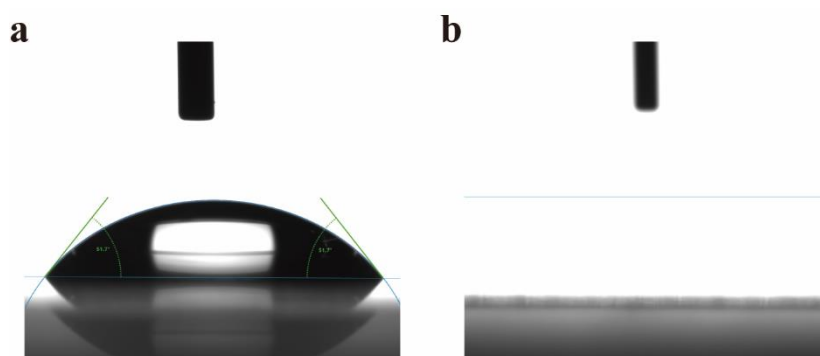


Figure 3.1.1: Picture of water droplet (10 μL) on (a) untreated glass slide ($\sim 51.7^\circ$) and (b) the freshly activated glass slides ($\sim 0^\circ$).

Other Substrates

Cellulosic papers (A4 size) were purchased from Refutura (Germany) and cut into small pieces (10 cm x 10 cm) before coating. Some other cellulosic-paper-based samples, including letter envelopes, toilet paper, and package boxes, were also used as supporting material.

Oxygen plasma

Oxygen plasma treatment (**Figure 3.1.2**) was employed to activate the substrate surface in some cases. The pristine substrates² were placed on a metal frame and inserted into the low-pressure oxygen plasma chamber Femto (Diener Electronic, Germany). After 2 min of surface hydroxylation treatment at 100-watt power, the samples were carefully taken out and immediately placed into the coating chamber for further synthesis steps.



Figure 3.1.2: Oxygen plasma.

¹ Notably, the θ_{WCA} of the activated glass slides would increase after long-term storage.

² Letter envelop and package box.

3.2 General synthetic protocol

In this section, the general synthetic procedure (gas phase) of the silicone-based micro- and nanostructures is summarized based on earlier studies in our group[1, 22] and our newly developed d-DAGS mechanism[23]. All reaction parameters, including substrate types, precursor types and amounts, relative humidity, reaction time, temperature, etc., can be adjusted for different research purposes. Therefore, the presented general synthetic procedure applies to all the syntheses throughout this project and can provide theoretical support for future studies.

3.2.1 Experimental setup

The experimental setup comprises two parts: (a) external system including gas source and thermostat, and (b) reaction chamber. All the syntheses mentioned in this project were performed in a custom-built desiccator (coating chamber) via the CVD method[1].

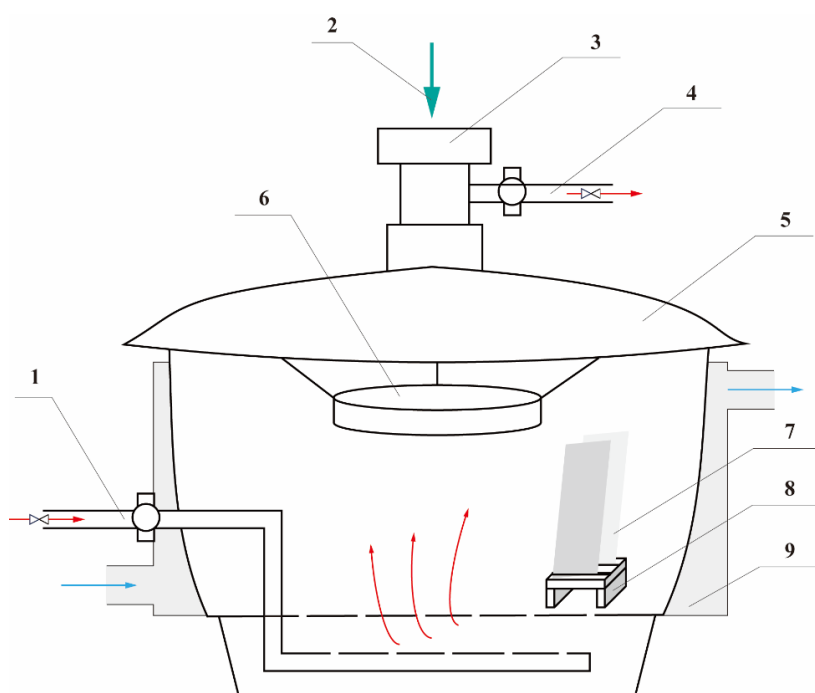


Figure 3.2.1: Scheme of the reaction chamber used for temperature-controlled CVD coatings. The setup basically consists of **1** gas inlet, **2** chemical inlet, **3** septum, **4** gas outlet, **5** reactor lid, **6** chemical holder dish, **7** sample, **8** special designed Teflon sample holder, and **9** water jacket connected with a water circulation system (left) water inlet, (right) water outlet.

The schematic of the main experimental setup (reaction chamber) is shown in **Figure 3.2.1**. A specially modified vacuum desiccator (Schott DURAN) with a rough volume of 6 L was surrounded by a water jacket, which is connected to a thermostat Julabo F34 (Julabo, Germany) to control the environmental temperature¹ inside the reaction chamber. Provided two valves of gas inlet and outlet enable the N₂ gas flow to purge the whole reaction chamber when needed (before or during the reactions). The N₂ gas flow with a specific *RH* was achieved by mixing humidified and dry N₂, supplied by the lab's internal gas source, and adjusted by two gas regulators². A hygrometer EE23 (E Plus E, Germany) was used to monitor the *RH* in real-time. A changeable chemical holder dish was placed in the center of the reaction chamber, which is used to support precursors slowly injected by a syringe through the septum in the middle of the reactor lid. Depending on the number of glass substrates used for each coating reaction, the corresponding number of specially designed Teflon sample holders (one for each glass slide) were placed neatly on the air-permeable shelf inside the reaction chamber. Other samples, such as cellulosic paper pieces, were put upright and symmetrically around the chemical holder dish to allow the chemicals to access both sides of the sample.

3.2.2 Experimental procedure

As shown in the experimental flow diagram (**Figure 3.2.2**), common procedures are comprised of four main steps including: Substrates, Pre-treatment, Reactions, and Post-treatment. Specifically, eight steps from **S1** to **S8** describe the whole procedure as follows:

- **S1**: sample preparations, detailed procedures can be found in section **3.1.2**;
- **S2**: a certain number³ of glass slides or other substrates, after cleaning and activation, were mounted on the specially designed Teflon sample holders. The distance between the samples and the edge of the chemical holder dish is around 10 cm. The reaction chamber needs to be sealed with the help of silicone-free laboratory grease (glisseal N). Both gas inlet and outlet valves were open for N₂ gas flush purposes.

¹ Without other specifications, the constant temperature of 23.0 °C ± 0.2 °C was used for all the syntheses mentioned in this project.

² Constant flow rate 2.5 L·min⁻¹ was maintained throughout the experiments.

³ Maximum 4 glass slides were used for the best coating quality.

- **S3:** switch the thermostat to equilibrate the temperature inside the reaction chamber and leave it on for the whole reaction procedure. Set the desired *RH* by regulating the ratio of the dry and humidified N₂ gas flow, and wait for at least 15 min until the value read from the hygrometer is stable. Depending on the desired nanostructures, the *RH* value is adjusted correspondingly. Before going to the next step, at least 1 h of the purging time is required to thoroughly equilibrate the reaction environment (both *RH* and *T*) inside the reaction chamber.
- **S4:** fully close the gas inlet and outlet valves. The desired precursors (a specific type and amount) were carefully injected into the reaction chamber by a syringe through the septum in the middle of the reactor lid.
- **S5:** the reaction time is counted from the moment of completion of the precursor injection process until the reaction chamber is opened or re-purged for further steps. Depending on the precursor types and the desired nanostructures, the reaction time is adjusted in a targeted manner.
- **S6:** the difference between the conventional DAGS method and the newly developed d-DAGS method is that the d-DAGS method allows multiple segments to be synthesized through the repetitive dynamic adjustment of the growth parameters, concomitant with the periodic re-purging and injection of the same or different precursors.
- **S7:** open both gas inlet and outlet valves, re-purge for a certain time at a certain *RH*, and a new precursor can be injected for the new round growth of the nanostructures. A cycle from **S4** → **S5** → **S6** → **S7** → **S4** is abbreviated as **R_x**, where x represents the number of cycles.
- **S8:** the samples were taken out immediately after reactions and blown by an N₂-gun to cease the reactions and clean up the sample surfaces.

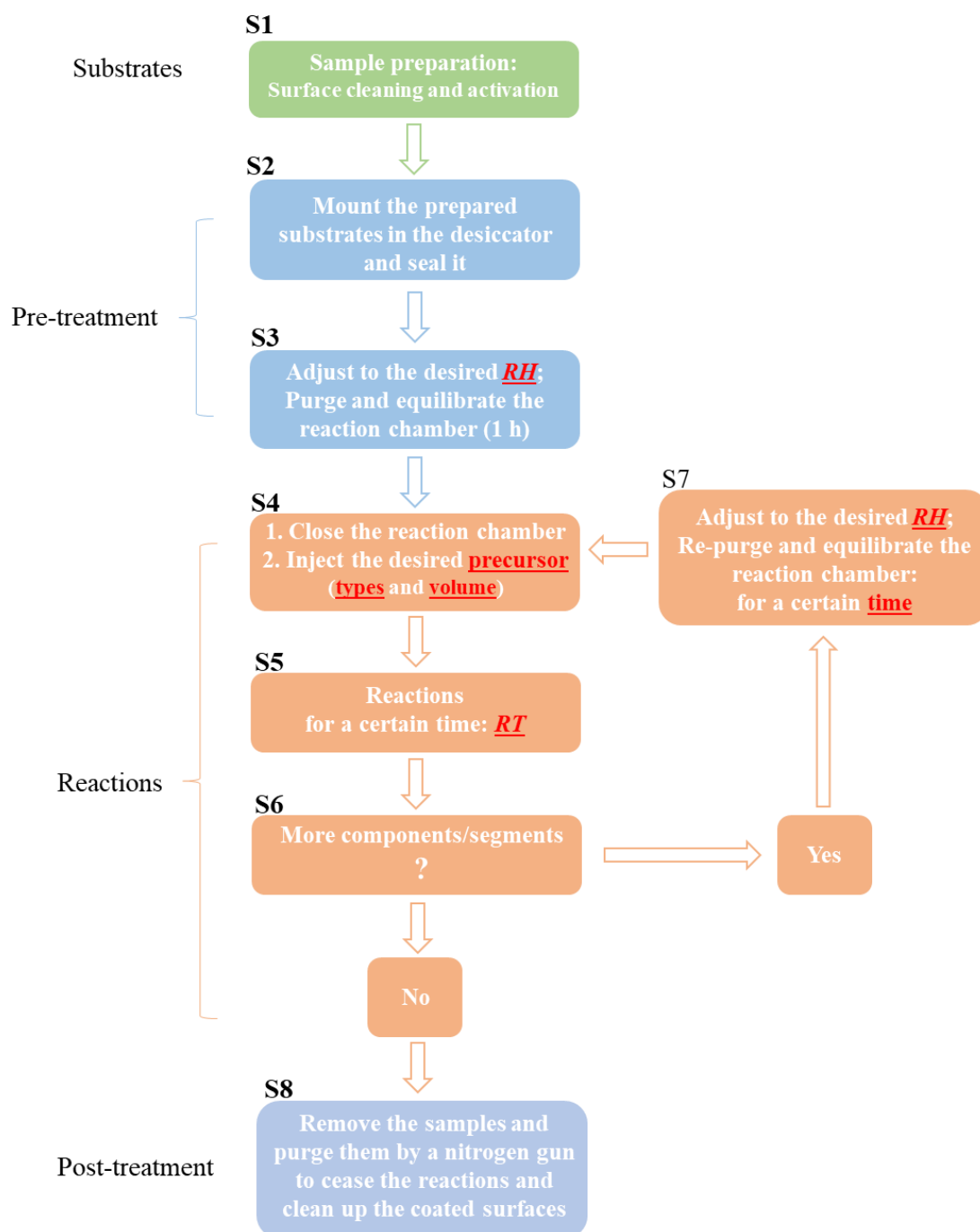


Figure 3.3.2: Experimental flow diagram¹.

¹ Red color with underline style marked parameters are variables.

3.3 Synthesis of SC silicone nanostructures

Single-component silicone nanostructures are synthesized by using only one precursor, but their final shapes may differ because different reaction parameters are applied. Reaction parameter tables only show the steps from **S3** to **S7** due to the steps **S1**, **S2**, and **S8** are the same unless otherwise specified.

3.3.1 Silicone nanofilaments

Conventional SNFs were used as comparisons in some tests. Based on the general synthetic protocol provided in section 3.2.2, its synthesis procedures were summarized in Table 3.3.1.

Table 3.3.1: Synthetic parameters of SNFs.

Seg ¹	S3 RH (%)	S4 (μL)	S5 RT (min)	S6	S7 RH, Time (min)
1	40 ± 0.3^2	ETCS: 400	240	no	-

3.3.2 Silicone nanorods

Short SNRs were synthesized for different purposes. Different growth parameters are summarized from Table 3.3.2 to Table 3.3.5.

To investigate the optimal growth conditions of silicone nanostructures

Table 3.3.2: Synthetic parameters of ETCS-based-SNRs.

Seg	S3 RH (%)	S4 (μL)	S5 RT (min)	S6	S7 RH, Time (min)
1	40 ± 0.3	100	20	no	-
1	50 ± 0.3	100	5	no	-
1	50 ± 0.3	100	20	no	-
1	50 ± 0.3	100	60	no	-
1	50 ± 0.3	400	20	no	-
1	50 ± 0.3	600	20	no	-
1	60 ± 0.3	100	5	no	-

¹ Segment order/number is counted from the bottom of the nanostructure.

² Error bars of the RH represent the range of the presented values.

1	60 ± 0.3	100	20	no	-
1	60 ± 0.3	100	60	no	-
1	60 ± 0.3	400	20	no	-
1	60 ± 0.3	75	20	no	-
1	60 ± 0.3	200	20	no	-
1	60 ± 0.3	600	20	no	-
1	60 ± 0.3	400	5	no	-
1	60 ± 0.3	400	60	no	-
1	70 ± 0.3	100	20	no	-
1	70 ± 0.3	400	20	no	-
1	70 ± 0.3	600	20	no	-
1	80 ± 0.3	100	20	no	-
1	80 ± 0.3	400	20	no	-
1	80 ± 0.3	600	20	no	-

Table 3.3.3: Synthetic parameters of VTCS-based-SNRs.

Seg	S3 RH (%)	S4 (μL)	S5 RT (min)	S6	S7 RH, Time (min)
1	40 ± 0.3	100	20	no	-
1	50 ± 0.3	100	20	no	-
1	60 ± 0.3	100	20	no	-
1	60 ± 0.3	100	5	no	-
1	60 ± 0.3	100	60	no	-
1	60 ± 0.3	100	240	no	-
1	60 ± 0.3	100	720	no	-
1	60 ± 0.3	600	20	no	-
1	60 ± 0.3	75	20	no	-
1	60 ± 0.3	200	20	no	-
1	60 ± 0.3	400	20	no	-
1	70 ± 0.3	100	20	no	-
1	80 ± 0.3	100	20	no	-

Table 3.3.4: Synthetic parameters of ETCS-based-SNRs on cellulosic paper¹.

Seg	S3 RH (%)	S4 (μ L)	S5 RT (min)	S6	S7 RH, Time (min)
1	30 \pm 1	800	120	no	-
1	50 \pm 1	400	120	no	-
1	50 \pm 1	1200	120	no	-
1	80 \pm 1	800	120	no	-

To do the coatings on cellulosic papers**Table 3.3.5:** Synthetic parameters of ETCS-based-SNRs on cellulosic paper.

Seg	S3 RH (%)	S4 (μ L)	S5 RT (min)	S6	Comments
1	50 \pm 1	800	120	no	10 cm x 10cm
1	50 \pm 1	2000	360	no	A4 size ²

For some characterization purposes, pure SNRs were obtained by scraping the surface of the SNRs-coated glass slide. Therefore, eight pieces of glass slides (75 mm x 25mm x 1mm) were coated with SNRs under the same conditions applied to cellulosic papers (10 cm x 10 cm).

3.3.3 Bamboo-shaped silicone nanorods

The optimal growth conditions for synthesizing the bamboo-shaped SNRs were obtained by systematically analyzing the morphology and surface properties of the short SNRs, as shown in **Table 3.3.6**.

¹ For all coatings on cellulosic papers, 2 h of equilibration time was used.

² For all coatings on cellulosic papers with A4 size, a bigger reaction chamber with a rough volume of 12 L was used.

Table 3.3.6: Synthetic parameters of bamboo-shaped ETCS-based-SNRs¹.

Seg	S3 RH (%)	S4 (μ L)	S5 RT (min)	S6 ²	S7 RH, Time (min)
1	60 \pm 0.3	400	10	(yes)	60 \pm 0.3, 10
2	-	400	10	(yes)	60 \pm 0.3, 10
3	-	400	10	(yes)	60 \pm 0.3, 10
4	-	400	10	(yes)	60 \pm 0.3, 10
5	-	400	10	(yes)	60 \pm 0.3, 10
6	-	400	10	(yes)	60 \pm 0.3, 10
7	-	400	10	yes	60 \pm 0.3, 10
8	-	400	10	yes	60 \pm 0.3, 10
9	-	400	10	yes	60 \pm 0.3, 10
10	-	400	10	yes	60 \pm 0.3, 10
11	-	400	10	yes	60 \pm 0.3, 10
12	-	400	10	(yes)	60 \pm 0.3, 10
13	-	400	10	yes	60 \pm 0.3, 10
14	-	400	10	yes	60 \pm 0.3, 10
15	-	400	10	yes	60 \pm 0.3, 10
16	-	400	10	yes	60 \pm 0.3, 10
17	-	400	10	yes	60 \pm 0.3, 10
18	-	400	10	no	-

¹ Table shows the complete synthesis procedure of the ultra-long bamboo-shaped 18-seg-ETCS-SNRs.

² Parentheses indicate that the choice can be either yes or no, because the bamboo-shaped SNRs presented in this work only consist of 1-seg (**R**₀), 2-seg (**R**₁), 3-seg (**R**₂), 4-seg (**R**₃), 5-seg (**R**₄), 6-seg (**R**₅), 12-seg (**R**₁₁), and 18-seg (**R**₁₇). Stop at any point marked in the table would lead to the production of the corresponding sample with a certain number of segments.

3.4 Synthesis of MCH silicone nanostructures

Multi-component hybrid silicone nanostructures are synthesized by using more than one precursor. Due to the different physical and chemical properties of the different types of precursors, the final morphology of the obtained MCH nanostructures has been significantly affected.

3.4.1 Bamboo-shaped nanostructures

Owing to the high similarity between ETCS and VTCS, the bamboo-shaped MCH-SNRs were synthesized when combining them in a specific manner. Reaction parameters were adjusted based on the morphological and chemical properties of the obtained SC-SNRs. Growth parameters were summarized from **Table 3.4.1** to **Table 3.4.3**.

Synthesis of 2-segment EV-MCH-SNRs

Table 3.4.1: Synthetic parameters of EV-MCH-SNRs.

Seg	S3 RH (%)	S4 (μL)	S5 RT (min)	S6	S7 RH, Time (min)
1	55 ± 0.3	ETCS: 400	10	yes	$55 \pm 0.3, 7$
2	-	VTCS: 250	10	no	-

Synthesis of 3-segment EEV-MCH-SNRs

Table 3.4.2: Synthetic parameters of EEV-MCH-SNRs.

Seg	S3 RH (%)	S4 (μL)	S5 RT (min)	S6	S7 RH, Time (min)
1	60 ± 0.3	ETCS: 400	10	yes	$55 \pm 0.3, 10$
2	-	ETCS: 200	10	yes	$50 \pm 0.3, 7$
3	-	VTCS: 300	10	no	-

Synthesis of 3-segment EVE-MCH-SNRs

Table 3.4.3: Synthetic parameters of EVE-MCH-SNRs.

Seg	S3 RH (%)	S4 (μL)	S5 RT (min)	S6	S7 RH, Time (min)
1	55 ± 0.3	ETCS: 400	10	yes	$55 \pm 0.3, 7$
2	-	VTCS: 250	5	yes	$55 \pm 0.3, 5$
3	-	ETCS: 400	10	no	-

3.4.2 Mushroom-shaped nanostructures

We were the first to synthesize the mushroom-shaped silicone nanostructures, known as silicone micro-hoodoos, via the d-DAGS method when a new dichloro-functional-silane, DCMVS, was introduced and combined with a base segment ETCS, which is classified as a kind of trichloro-functional-silane. The optimal growth conditions for well-structured SMHs, as shown in **Table 3.4.4**, were obtained by adjusting the basic reaction parameters, such as *RH*, *RT*, and *VOL*.

Table 3.4.4: Synthetic parameters of MCH-SMHs.

Seg	S3 RH (%)	S4 (μL)	S5 RT (min)	S6	S7 RH, Time (min)
1	60 ± 0.3	ETCS: 400	10	yes	$60 \pm 0.3, 10$
2	-	DCMVS: 400	960	no	-

3.5 Chemical functionalization on MCH silicone nanostructures

The photoinitiated radical-based thiol-ene “click” reactions under UV illumination were employed in functionalizing the multi-component hybrid silicone nanostructures. The photo-initiator DMPA with the concentration of $0.01 \text{ g}\cdot\text{ml}^{-1}$ and $0.005 \text{ g}\cdot\text{ml}^{-1}$ were separately used in reactions when the samples were being functionalized by cysteamine ($0.1 \text{ g}\cdot\text{ml}^{-1}$) and 1,4-butanedithiol ($0.04 \text{ g}\cdot\text{mL}^{-1}$). Before the reactions, the mixture of ethanol/water (v/v at 7:3) was prepared and used to dissolve the reactants and photo-initiator under ultrasonication at 37 kHz for 10 min. Samples were appropriately cut into small pieces and immersed into the as-prepared solution that was transferred into a quartz reactor. The quartz reactor was then carefully placed into a UV chamber (RPR-200, SNE Ultraviolet Co., USA) equipped with four UV lamps ($\lambda = 250 \text{ nm}$), and the reaction was triggered when the UV chamber was switched on. Different reaction times, including 3, 5, 10, 20, 30, 60, and 90 min were investigated, respectively, for further characterizations. After the reactions, the sample was removed and rinsed with EtOH (70%), followed by Milli-Q water for at least 5 min. The freeze-drying machine (CHRIST, Germany) was employed in sample drying treatment.

3.6 Sample evaluation and characterizations

Several tests with respect to the physical and chemical properties of the prepared samples were conducted to evaluate their potential applications in different practical scenarios. Detailed test procedures, application instructions, and characterizations are presented in this section. Notably, according to the particularity of different samples, not all samples synthesized in sections 3.3 and 3.4 were subjected to all of the following tests. The sample used, and their test and application performances can be found in the section of **Results and Discussion**.

3.6.1 Chemical durability test

In order to evaluate the short and long-term chemical durability of the ETCS-based samples, a series of dip tests in some selected solutions were conducted. The solutions used can be briefly classified as (a) aqueous solutions, including HCl (0.1 M)¹ and NaOH (0.1 M); (b) polar and nonpolar organic solvents, including toluene, EtOH, chloroform, and DMF.

Glass-substrate-based samples

Several samples decorated by 6-seg-ETCS-SC-SNRs were cut into small pieces (26 mm x 26 mm) and immersed into the freshly prepared chemical solutions, including HCl, NaOH, EtOH, DMF, and toluene, respectively, for at least 6 days. For acidic and basic aqueous solutions, one month immersion test was performed. At timed intervals, small sample pieces were taken out and dried by freeze drying method, which can help to maintain the original morphology of the samples and will be discussed in section 4. Static water contact measurements on the sample surfaces were conducted, and at least five measurements on different positions of the sample were recorded. After six days and one-month tests, both morphology and chemical compositions of the samples were checked by SEM and FT-IR separately.

Cellulosic-paper-based samples

Paper-based samples were cut into small pieces (30 mm x 30 mm) and immersed into the freshly prepared organic solvents, including EtOH, DMF, acetone, chloroform, and

¹ Corresponding pH values were verified by an inoLab pH electrode (WTW, Germany).

toluene, respectively, for 24 h, and in aqueous solutions of HCl and NaOH for 15, 30, 45, 60, and 90 min, respectively. Static water contact angle was measured after the samples were removed and dried under vacuum at ambient conditions for 6 h.

3.6.2 Mechanical durability test

Linear abrasion test

An abrasion tester (AB5000, TQC, Germany) was employed for all the linear abrasion tests on different samples:

- (a) For glass-substrate-based samples: a 6-seg-ETCS-SC-SNRs coated sample (26 mm x 26 mm) was mounted on the test area with surrounding 4 pieces of the identical untreated glass slides to provide a uniform abrasion contact area. A nitrile glove-covered sponge abradant with weights of a specific weight moved over the sample with a stroke speed of 5 cycles per minute to provide an effective abrasion distance of 8.5 cm. Each one-way tangential sliding was counted as one-time abrasion. Pressures of 0.5, 1.5, and 2.5 kPa were tested separately. Both the θ_{WCA} and θ_{WSA} of the samples were measured after the linear abrasion test.
- (b) For cellulosic-paper-based samples: the same tests described above were applied in cellulosic-paper-based samples, but with different stroke speeds, distances, and loading weights of 10 cycles per minute, 30 cm, and 50 g, respectively. Every time, a back-and-forth sliding was counted as one cycle. The WCA was recorded after the test.

Tensile test

Cellulosic-paper-based samples (10 mm x 100 mm) were used in tensile measurement with a gap of 40 mm by an Instron 3345 Universal Testing Device (US). The moving rate of $1 \text{ mm} \cdot \text{min}^{-1}$ was applied to the device. At least three identical samples were tested to obtain the average maximum stress and strain values. The Bluehill Universal software (US) was used for data analysis.

Adhesive loop tack strength test

In order to test the anti-adhesive performance of the mushroom-shaped SMHs samples, the adhesive loop tack strength test was performed using the Instron 3345 Universal

Testing Device (US). To conduct the test, as shown in **Figure 3.6.1**, a lab-used paper tape (TimeMed) with a width of 19 mm was cut into 20 cm lengths, and both ends were combined together and connected to the movable head of the test device with unstick side facing inward. The glass-substrate-based sample pieces (26 mm x 26 mm) were mounted on a sample holder and stabilized on the unmovable stage of the device. Before the measurement, the movable head was lowered until the tape loop was fully attached to the sample surface with a contact area of around 494 mm². A weight (15 g) was placed on the contact area for at least 1 min to ensure the tight attach. Afterward, the weight was removed, and the movable head was lifted at a constant speed of 300 mm·min⁻¹ until the tape and sample were completely separated. The adhesion force interaction between the tape and the sample was recorded. At least 3 measurements were conducted each time to obtain the average maximum force value.

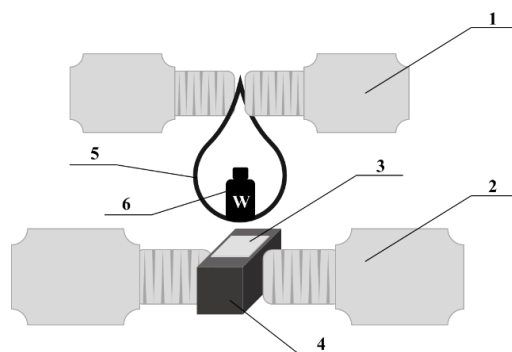


Figure 3.6.1: Scheme illustration of the Adhesive loop tack strength test. The presented image consists of **1** movable head, **2** unmovable stage, **3** stabilized sample, **4** sample holder, **5** tape, and **6** weight.

3.6.3 Environmental durability test

The anti-wetting properties of the as-prepared samples after being exposed to some extreme environments were characterized by θ_{WCA} . These environments consist of UV conditions ($\lambda = 350$ nm), high humidity environment ($RH \approx 90\%$), and extreme temperatures (-196 °C in liquid N₂ and 200 °C in lab oven). The UV-resistance test was performed in the UV chamber equipped with eight UV lamps.

3.6.4 Buoyancy test

In order to measure the buoyancy promotion ability of the bamboo-shaped SNRs with

different numbers of segments (0, 1, 2, 3, 4, 5, 6, 12, 18), the maximum weight that can be loaded on a floating sample was measured. To conduct the test, a small beaker was placed on the floating sample (26 mm x 26 mm) whose surrounding surfaces had been rubbed by sandpaper, and the weight was increased by continuously adding water droplets into the small beaker. The maximum weight was recorded and transferred into the buoyancy force following Archimedes' principle and the balanced force equation.

3.6.5 Biological test

Escherichia coli BL21 strain grown in LB (Luria-Bertani) medium at 37 °C overnight was diluted by LB until the optical density of 0.02 ($\lambda = 600$ nm), namely $OD_{600} = 0.02$, was achieved. Presterilized pristine and decorated cellulosic-paper-based samples were immersed into the respective bacterial cell culture dilution for 50 s and subsequently rinsed with 100 μ L of ddH₂O. All samples were then transferred to the middle position of the LB agar plates and incubated overnight at 37 °C. To verify the result of the anti-microbial activity test, pictures after bacteria incubation were acquired under a Leitz Laborvert light microscope (Germany) with 100x magnification.

3.6.6 Water harvesting

The water harvesting test was conducted with the bare glass slide sample, SNFs coated sample, and bamboo-shaped SNRs with different numbers of segment (1, 3, 6) coated samples, respectively. The setup is shown in **Figure 3.6.2**.

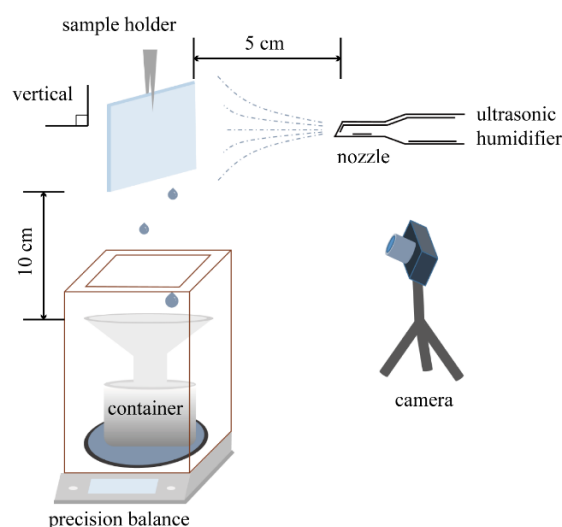


Figure 3.6.2: Scheme of the setup used for water harvesting application.

Reprinted with permission from [23].

All samples were cut into 26 mm x 26 mm pieces and tightly fixed by a vertically placed sample holder. A container equipped with a funnel was stabilized inside a precision balance (resolution: 0.1 mg) to collect the water droplets harvested by glass samples. The distance between the sample and the top of the funnel is 10 cm. A commercial Ultrasonic Humidifier (JS-38-J ultrasonic humidifier, Well Feeling, Switzerland) was stabilized on the same level with the sample center at a distance of 5 cm between the sample surface and the custom-made nozzle and used to generate artificial fog flow ($4.7 \text{ mL}\cdot\text{min}^{-1}$) with tiny water droplets. A minimum 30 min was required for each measurement, and the whole process was recorded by a camera. Tests were performed under controlled conditions: T : $20.0 \text{ }^\circ\text{C} \pm 0.2 \text{ }^\circ\text{C}$ and RH : $\approx 90\%$.

The water collection rate was obtained by:

$$WCR = \frac{m}{St} \quad (3.6.1)$$

Where m is the weighted mass of the collected water droplets in mg, S is the fog capture area in cm^2 , and t is the collection time in min.

3.6.7 Ninhydrin test

The ninhydrin test was considered a quick test to verify the functionalization of multi-component silicone nanostructure samples. The sample functionalized by cysteamine was placed into a Petri dish, and a few droplets of ninhydrin solution were subsequently added until the sample surface was completely wetted. The color change can be checked after 15 min heating in a water bath, from which the temperature was set as $50 \text{ }^\circ\text{C}$.

3.6.8 High-speed camera

A high-speed camera system (MiniVis EoSens, Karlsruhe, Germany) was used to track the trajectory of the water droplet¹ after touching the sample surfaces. Both the water-impacting test and self-cleaning test were performed with the assistance of the high-speed camera system. Frame rate 500 was used during recording. The scheme of the setup is shown in **Figure 3.6.3**.

¹ Unless otherwise specified, the water droplet used throughout the project was $10 \text{ }\mu\text{L}$.

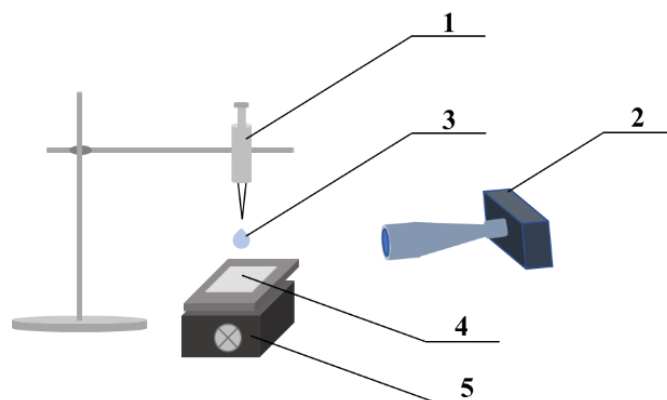


Figure 3.6.3: Scheme of the setup used in high-speed camera test. The setup consists of **1** water droplet dispenser, **2** high-speed camera system, **3** generated water droplet, **4** sample, **5** tilt-angle-changeable sample stage.

Water-impacting test

ETCS-based bamboo-shaped samples with n segments, where $n = 1, 2, 3, 4, 5, 6, 12,$ and $18,$ and MCH-SNRs samples before and after functionalization were separately tested. Water droplet was released from a certain height (1.5 cm) above the sample surface, and the whole process of its free-falling and bounces were recorded. Snapshots for each time the water droplet is at the maximum bounce height were captured for further analysis. Weber number¹ is calculated as:

$$We = \frac{\rho v^2 d}{\gamma} \quad (3.6.2)$$

Where ρ is the density, v is the velocity, d is the diameter of the droplet, and γ is the liquid-air surface tension.

Self-cleaning test

The self-cleaning tests were performed with a 6-seg-ETCS-SC-SNRs coated sample and MCH-SNRs samples before and after functionalization, respectively. The sample was placed on a tilting stage at an angle of 5° before the test. The process of the rolling-off water droplet taking away the dirt² that was placed on the sample surface was recorded by a high-speed camera.

¹ For the water-impacting test presented in this work, $d_{WD} = 2.57$ mm and $v = 0.5$ m·s⁻¹.

² Chalk particles consist of sand and dust.

3.6.9 Contact angle goniometry

The anti-wetting ability of the samples was characterized by a contact angle goniometer (DSA100, Krüss GmbH, Germany) equipped with a PA3220 tilting device. Both θ_{WCA} and θ_{WSA} were tested at $23.0\text{ }^{\circ}\text{C} \pm 0.2\text{ }^{\circ}\text{C}$ using Milli-Q water and calculated using the Laplace-Young fitted routine built into the device software (ADVANCE). Each measurement was performed within 1 min to avoid the undesirable effects caused by water evaporation. At least 3 measurements were repeated on different locations of the sample surface, and all results were presented as means \pm S.D.

3.6.10 Fourier transform infrared spectroscopy (FT-IR)

The FT-IR spectra in the range of 400 cm^{-1} to 4000 cm^{-1} (64 scans) were obtained from the attenuated total reflection (ATR) FT-IR spectrometer equipped with an ATR single reflection crystal (Bruker Optic GmbH, Germany). The background spectra were acquired against air at room temperature.

3.6.11 UV-vis spectroscopy

Transmittance spectra in the range of 300 nm to 800 nm were acquired from the UV-vis spectrometer (Lambda 950, PerkinElmer, Llantrisant, United Kingdom) with the background collected against air.

3.6.12 Scanning electron microscopy (SEM)

The morphology of the samples was checked by a high-resolution SEM (GeminiSEM 450, Zeiss, Germany) equipped with an EDX detector at an acceleration voltage of 10 kV under InLens detector¹ or 5 kV under SE2 detector².

Sample preparation

Both glass-substrate-based and cellulosic-paper-based samples were appropriately cut into small pieces and mounted on the carbon tape that was pre-fixed on the SEM pin stub. Followed to be sputter-coated with a conductive Platinum layer (10 nm for glass-substrate-based samples and 5 nm for cellulosic-paper-based samples) using a CCU-

¹ Used for checking surface structures at a 45° tilt angle.

² Used for checking the side view of surface structures.

010 HV coating unit (Safematic, Switzerland).

3.6.13 Transmission electron microscopy (TEM)

TEM sample characterization (Tecnai G2 Spirit, FEI, Netherlands) was conducted at 120 kV. STEM-EDX¹ was employed to acquire the elemental analysis with the assistance of the system software²: Inca or AZtec.

Sample preparation

Samples were broken into small pieces and immersed in EtOH (≈ 3 mL) solvent in a glass vial (10 mL). After being sonicated at room temperature for 10 min, a droplet (≈ 10 μ L) of the turbid liquid was transferred to a carbon-supported copper grid (Lucerna Chem AG, Luzern, Switzerland) by a pipette. This procedure was repeated 10 times after evaporating solvent to ensure enough silicone nanostructures were evenly dispersed on the sample holder.

3.6.14 Confocal microscopy

Glass-substrate-based samples³ coated by multi-component silicone nanostructures before and after functionalization were characterized by this technique to investigate the influences of the morphology and the functionalization on surface anti-wetting properties. The Leica SP8 automated inverse CLSM (Leica Microsystems GmbH, Germany) was used in acquiring the z-stack 3D confocal images⁴. All measurements were performed at room temperature (≈ 23 °C) with a mild relative humidity ($\approx 50\%$) and completed within 15 min to minimize the effect of water droplet evaporation. 10 μ L of Atto 633-COOH dye-containing water droplet was used during the imaging process to provide fluorescent signals. General system settings are summarized in **Table 3.6.1**.

¹ Equipped with high-angle annular dark field detector.

² The system software (both from Oxford Instruments) used throughout the project was annotated in the section on results and discussion.

³ Thickness of the glass substrate is 1# to ensure good penetration of the laser beam.

⁴ All 2D confocal images presented in this work were extracted from the z-stack 3D images.

Table 3.6.1: Confocal microscopy settings.

General settings		Seq. 1	Seq. 2
Channel	8-bit (0 - 255)	Detector	HyD
resolution	12-bit (0 - 4095)		-
			PMT
Scan mode	XYZ	Beamsplitter	TD 488/52/638
Scan speed	600 Hz	Wavelength	645 – 720 nm
			631 – 644 nm
Zoom factor	x10	Laser intensity	-
			-
Pinhole	95.5 μm	Gain	-
			-
PinholeAiry	999.23 mAU	Z-stack mode	bottom to top
			bottom to top
Objective lens	HC PL APO CS2 63x/1.40 OIL	Z-step	0.16 μm
			0.16 μm

Some explanations for **Table 3.6.1:**

- Some abbreviations were used limited to this table: sequential channel (seq.), hybrid (HyD), photomultiplier (PMT).
- HyD in counting mode was used for acquiring the fluorescent signals; PMT in seq.1 was used to gain a brightfield image, which is manually removed in the following analysis; PMT in seq.2 was used to acquire the reflectance signals.
- The wavelength given in seq.1 is for the HyD detector.
- Laser intensity and gain values were appropriately adjusted for different samples.
- 2D and 3D images presented in this work have been appropriately adjusted using the software Imaris (Oxford Instruments) or Fiji (ImageJ package), and display settings were provided with the images.

4. Results and Discussion

4.1 Synthetic parameters of the regular SC-SNRs

In order to gain a better understanding of the synthesis method and potential application ability of the silicone nanostructures based on the conventional DAGS method, systematic investigations upon the effects of the synthesis conditions on the morphology and surface properties of the single-component-based silicone nanostructures were conducted in this section. Some pivotal synthetic parameters, relative humidity, reaction time, types and volume of the precursors, and substrate type, which can directly affect the growth status of the single silicone nanostructure, were investigated under a constant temperature.

4.1.1 ETCS-based silicone nanostructures¹

As explained by the DAGS method and some previous studies[1, 22, 26], *RH* is considered to play an essential role in determining the base diameter of the silicone structures by influencing the size of water droplets condensed on the activated substrate surfaces. As shown in **Figure 4.1.1.a**, with other conditions remaining constant, an obvious increase tendency of the base diameter of the silicone structures can be observed with increasing the *RH*. The height of the structures decreases resulting from two possible reasons: 1), 20 min of the *RT* is too short to keep the structures growing; 2), higher *RH* leads to a big decrease in the ratio of the molar mass of the precursor and water ($n_{\text{silane}}/n_{\text{water}}$). Considering the other parameter combinations (**Figure 4.1.1.b1-b3**), a general shape change of the silicone structures with respect to the *RH* can be summarized as: filaments → rods → volcanoes → rings. Notably, the mixtures of two shapes are also observed, for example, the mixture of filaments and rods (**Figure 4.1.1.b1**) and the mixture of rods and volcanoes (**Figure 4.1.1.b4**), which further

¹ Some parts of this section have been published: **Kangwei Chen**, Shanqiu Liu, Yuen-Yee Lau & Stefan Seeger, *Small*, **2022**, 18 (40), 2203820.

verifies the slow transition of the silicone shapes relying on the change of RH .

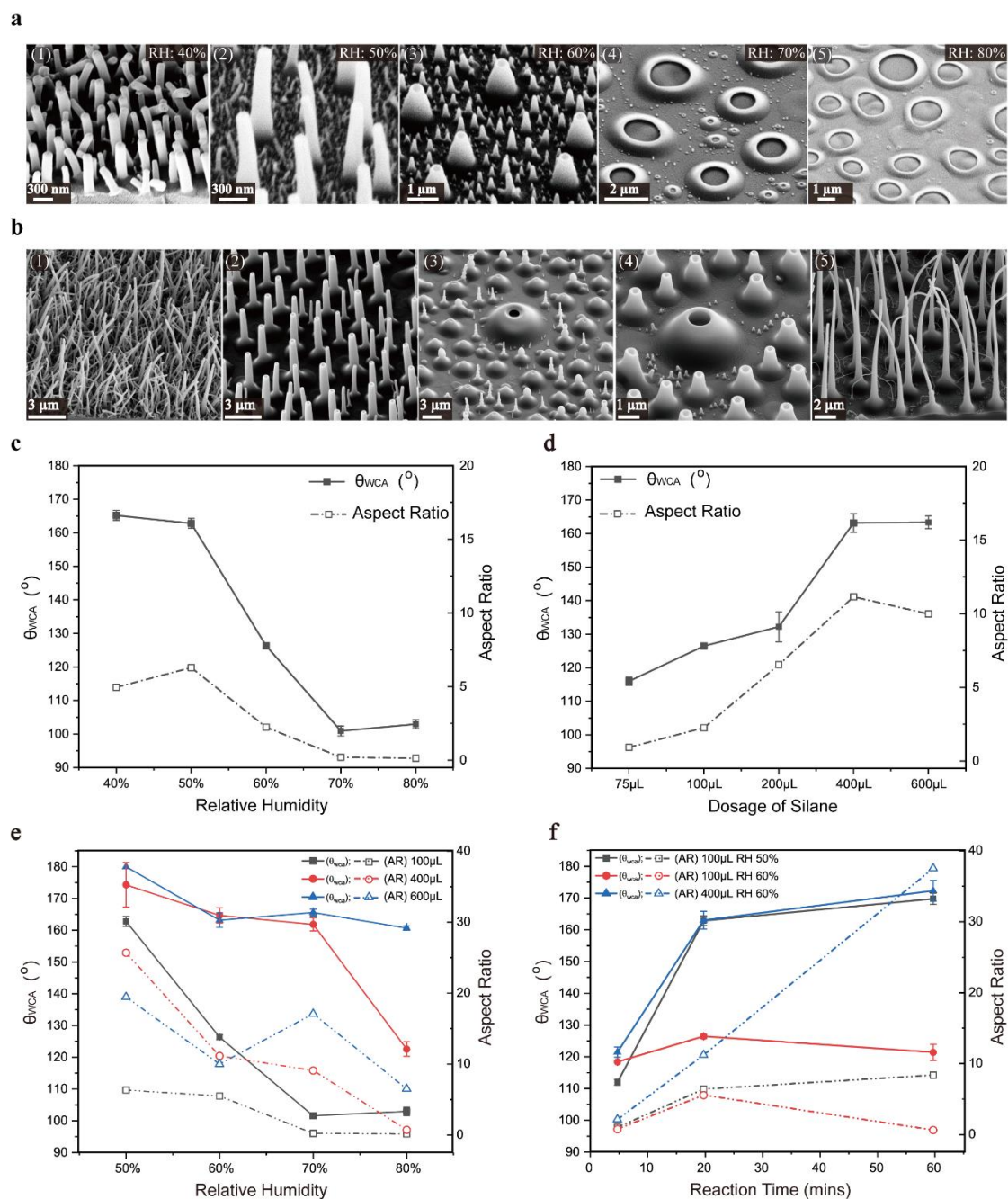


Figure 4.1.1: The effects of growth conditions on ETCS-based silicone structures and their surface properties. (a1-a5) SEM images of silicone structures produced by varying the RH under constant RT (20 min) and a certain amount of precursor (100 μ L). (b) SEM images of the obtained silicone structures under conditions of: (b1) 400 μ L, RH 50%, 20 min. (b2) 400 μ L, RH 60%, 20 min. (b3) 400 μ L, RH 80%, 20 min. (b4) 400 μ L, RH 60%, 5 min. (b5) 400 μ L, RH 60%, 60 min. (c-f) The changes of water contact angle (θ_{WCA}) and aspect ratio with RH , VOL and RT set as (c) 100

μL , 20 min, (d) RH 60%, 20 min, and (e) 20 min. Reprinted with permission from [23].

In addition, with increasing the RH , a similar decrease tendency is observed from both θ_{WCA} and aspect ratio, as shown in **Figure 4.1.1.c** and **Figure 4.1.1.e**, despite the different volumes of precursors applied. It can be concluded that the volcano and ring-shaped structures caused by applying high RH are limited in applications as a functional surface coating due to their less rough morphology and poor performance in water resistance. Conversely, low RH is preferred to fabricate a relatively regular rod or filament structure with an extensive aspect ratio and excellent superhydrophobicity.

During the CVD process, the hydrolysis and condensation reactions of the precursor are deeply affected by the ratio of the reactants, namely, the molar mass of the precursor and water. As discussed above, different water amounts can be obtained by regulating the RH . Changing VOL under the same conditions can also lead to a change of $n_{\text{silane}}/n_{\text{water}}$, resulting in different geometrical parameters. From 100 to 400 to 600 μL , the increase of both θ_{WCA} and aspect ratio can be expected (**Figure 4.1.1.e**). As illustrated in **Figure 4.1.1.a3** and **Figure 4.1.1.b2**, it is clear that the better-shaped SNRs are produced by applying 400 μL precursors. However, due to the size limitation of the reaction chamber, more precursors cannot achieve better performance; for example, similar results in both θ_{WCA} and aspect ratio are obtained from 400 to 600 μL precursors (**Figure 4.1.1.e**). Therefore, finding a proper ratio of the reactants under a certain reaction environment is important in synthesizing the desired silicone nanostructures.

The effects of RT are mainly reflected in the height of the as-prepared structures, as illustrated in **Figure 4.1.1.b4**, **b2**, and **b5**. A longer RT (5 min \rightarrow 20 min \rightarrow 60 min) provides more opportunities for a complete reaction between the reactants, and the deposited silicone nanostructures are able to keep growing even with a tendency towards bent-growth (sharp top) that resulted from the consummation of the water droplet sitting at the top of the structure. Although a long RT enables to improve θ_{WCA} and the aspect ratio (**Figure 4.1.1.f**), RT should be appropriately adjusted to achieve better structural control and a higher reaction efficiency.

In summary, synthetic parameters such as RH , VOL , and RT can jointly determine the morphology of the silicone-nanostructure-based surface coatings. A lower RH ($\leq 40\%$)

and longer reaction time (≥ 60 min) are more suitable for the growth of silicone micro- and nano-filaments with diameters between ~ 60 nm and ~ 250 nm, whereas a higher RH ($\geq 70\%$) and shorter reaction time (≤ 5 min) lead to the formation of silicone volcanoes and rings. Through the comprehensive consideration of morphological characteristics, reaction efficiency, and hydrophobic properties, we selected the optimal conditions of *VOL*: 400 μ L, *RH*: 60%, and *RT*: 10 min for the growth of short single SNRs. As shown in **Figure 4.1.1.b2**, the one-segment rods fabricated under the optimal condition presented a perfectly regular and ordered arrangement.

4.1.2 VTCS-based silicone nanostructures¹

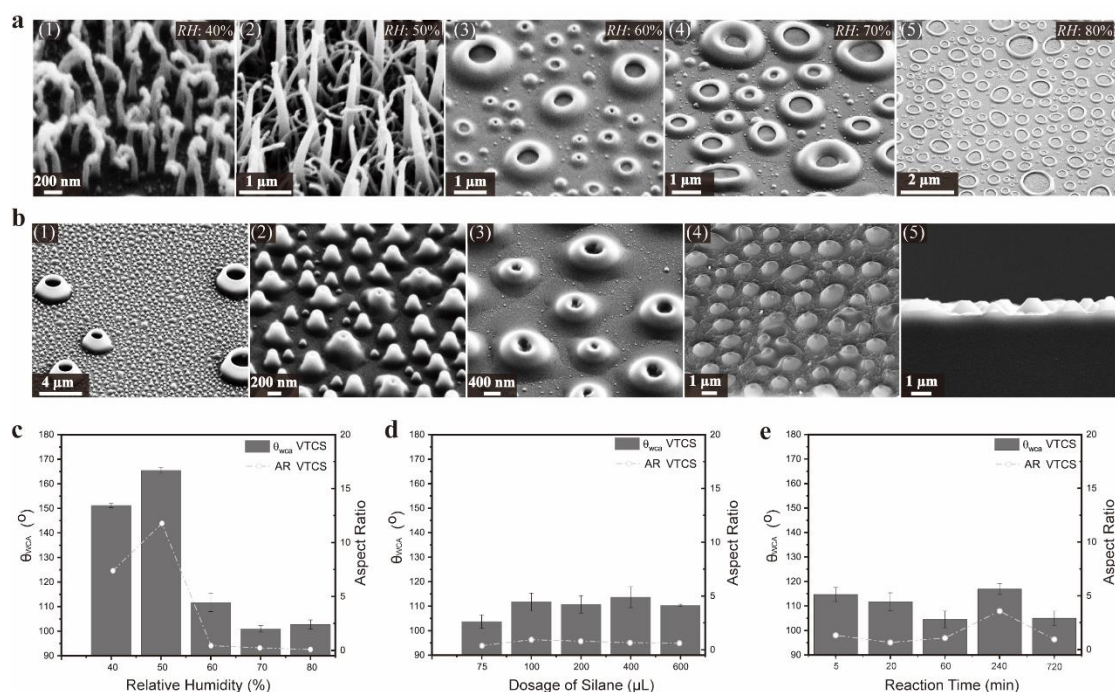


Figure 4.1.2: The effects of growth conditions on VTCS-based silicone structures and their surface properties. (a1-a5) SEM images of silicone structures produced by varying the *RH* under constant *RT* (20 min) and *VOL* (100 μ L). (b) SEM images of the obtained silicone structures under conditions of: (b1-b2) *RT*: 5 min; *RH*: 60%; *VOL*: 100 μ L. (b3) *RT*: 60 min; *RH*: 60%; *VOL*: 100 μ L. (b4-b5) *RT*: 20 min; *RH*: 60%; *VOL*: 600 μ L. (c-e) The changes of water contact angle (θ_{wca}) and aspect ratio with *RH*, *VOL* and *RT* set as (c) *RT*: 20 min and *VOL*: 100 μ L. (d) *RT*: 20 min and *RH*:

¹ Some parts of this section have been submitted for publication: *Heterogeneous Silicone Nanorods with Region-Specific Functionality*.

60%. (e) *RH*: 60% and *VOL*: 100 μL .

The same investigations were also performed on VTCS-based silicone structures, as shown in **Figure 4.1.2**. Previous studies have reported the VTCS-based micro and nano-morphologies, for example, fibers[110] and filaments[138]. A similar trend of shape change from filaments \rightarrow rods \rightarrow volcanoes \rightarrow rings with increasing *RH* can also be observed from VTCS-based nanostructures (**Figure 4.1.2.a**). Especially the mixture of two different shapes, such as filaments and rods, presented in **Figure 4.1.2.a2** further proves that *RH* plays an important role in determining the base diameter of the synthesized silicone structures.

From final morphology (**Figure 4.1.2.a-b**) to θ_{WCA} (**Figure 4.1.2.c-e**) to aspect ratio (**Figure 4.1.2.c-e**), a negligible effect can be seen by adjusting the *RT* (b1, b2 \rightarrow b3: 5 min \rightarrow 60 min) and *VOL* (a3 \rightarrow b4: 100 μL \rightarrow 600 μL) under an unsuitable *RH* value. Additionally, VTCS is similar to ETCS because they are both tri-chloro-functional silane and have similar molecular weight. However, the VTCS-based SNRs require a more careful adjustment upon synthetic parameters, which might be because they bear the more reactive vinyl functional groups. All in all, a dynamic range of synthesis conditions is probably more suitable for the actual operation in fabricating the required VTCS-based nanostructures, that is, *RT* (\approx 10 to 20 min), *VOL* (\approx 250 to 300 μL), and *RH* (\approx 50% to 55%).

4.1.3 Cellulosic-paper-based substrate¹

In order to obtain a versatile protective coating on the cellulosic-paper-based substrate, several combinations of the growth parameters are investigated. Notably, as mentioned in section 3.3, all coatings on cellulosic-paper-based substrate have 2 h of equilibrium time before the reactions. As shown in **Figure 4.1.3.a-b**, some similar conclusions with section 4.1.1 can be obtained that either too low or too high *RH* (30% and 80%) are not helpful in decorating the paper surface texture with ETCS-SC-SNRs. Especially when *RH* is too high, the paper surface is probably fully wetted, and no water droplet, even with a big diameter, can be condensed on the surface. Deposition of 1D silicone nanostructures cannot be triggered without a condensed water droplet. Therefore, no

¹ Some parts of this section have been published in: Shanqiu Liu*, Kangwei Chen*, Alma Salim, Jingguo Li, Davide Bottone & Stefan Seeger, *ACS Nano* **2022**, 16 (6), 9442-9451. (*Co-first author).

visible silicone structures can be found under this condition. In addition, insufficient *VOL* (400 μL), as shown in **Figure 4.1.3.c**, resulting in an ununiform growth of the SNRs, which has a similar morphology with the coatings conducted under low *RH* (**Figure 4.1.3.a**). Therefore, the ratio of n_{silane} and n_{water} is also pivotal and should be adjusted to an appropriate range.

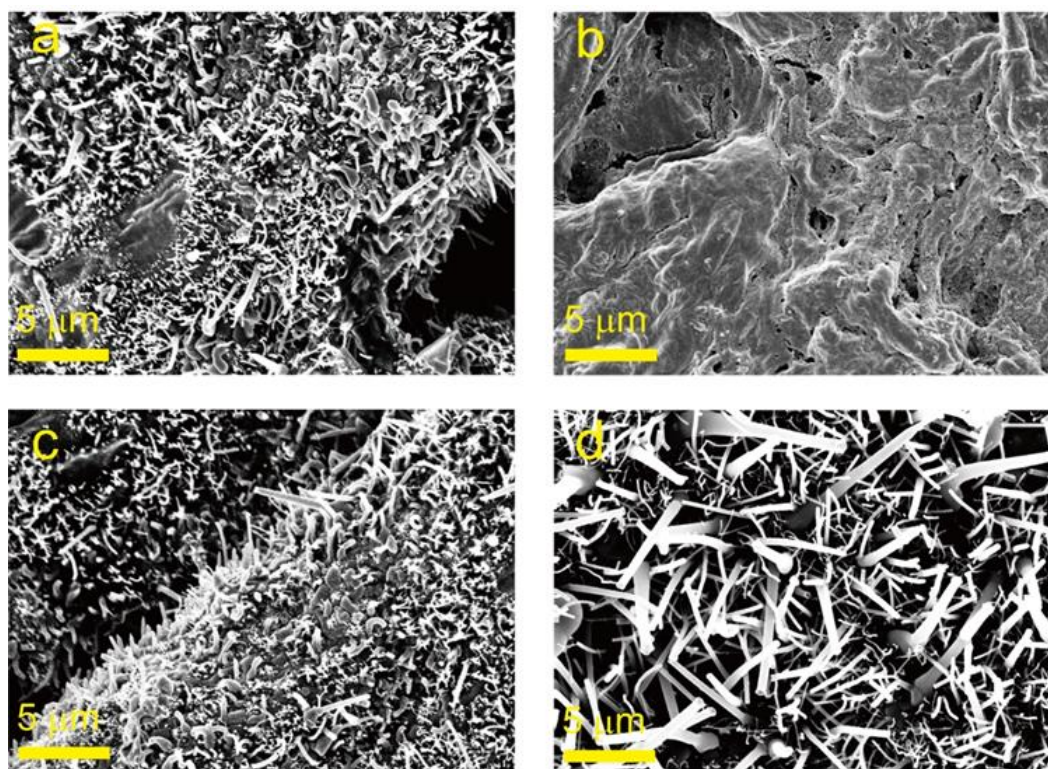


Figure 4.1.3: SEM images of cellulose paper modified by ETCS-based silicone nanostructures under the conditions: (a) *VOL*: 800 μL ; *RH*: 30%. (b) *VOL*: 800 μL ; *RH*: 80%. (c) *VOL*: 400 μL ; *RH*: 50%. (d) *VOL*: 1200 μL ; *RH*: 50%. All above reactions have the same *RT*: 2 h. Reprinted with permission from [25].

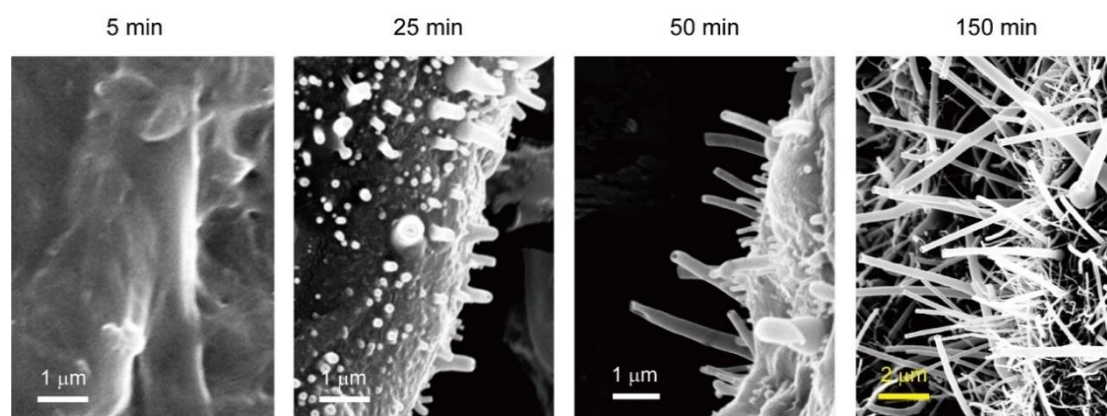


Figure 4.1.4: SEM images of the cellulose paper after being modified by

ETCS-based silicone nanostructures under the conditions of VOL : 800 μL , RH : 50%, and a varying RT from 5 min to 150 min (left \rightarrow right). Reprinted with permission from [25].

The height of ETCS-SC-SNRs (thickness of the coating) can be tuned by adjusting the RT of the CVD process, as shown in **Figure 4.1.4**. As explained in section 4.1.1, a long-time reaction enables to provide more opportunities for a more complete reaction between the reactants (precursors and water), and the deposited SNRs keep growing with a shaper tendency on the top area because of the volume consumption of the water droplet staying at the top cavity.

4.1.4 Summary

All in all, after performing a series of testing experiments under a constant temperature ($23.0\text{ }^{\circ}\text{C} \pm 0.5^{\circ}\text{C}$), some conclusions can be obtained as follows:

(i) RH determines the base diameter of different silicone-based micro- and nanostructures, for example, filaments (d : ~ 60 nm), rods (d : ~ 80 nm to ~ 800 nm), volcanoes and rings (a bigger d). According to the DAGS method, the base diameter of the synthesized silicone structures is dependent on the size of the condensed water droplet on the solid surface, which can be controlled by adjusting the RH in the step of pre-treatment S3.

(ii) Under the same reaction conditions, the height/length of the synthesized silicone structures is determined by RT .

(iii) VOL can be tuned to influence the ratio between reactants ($n_{\text{silane}}/n_{\text{water}}$) and therefore affect the reaction efficiency. Notably, the ratio is determined by both VOL and RH ; in some cases, a certain constant RH is employed for generating the required diameter, VOL is therefore adjusted to reach a high reaction efficiency and produce a perfect micro- and nanostructure.

(iv) Different types of substrates might be used after being activated, but the growth of the structures theoretically follows the above rules (i – iii). Particular adjustment of the synthetic parameters is necessary to gain the required shape of the final silicone micro- and nanostructure.

4.2 Characterizations and applications of ETCS-SC-SNRs on cellulosic-paper-based substrate

Some parts of this section have been published: Shanqiu Liu*, Kangwei Chen*, Alma Salim, Jingguo Li, Davide Bottone & Stefan Seeger, Printable and Versatile Superhydrophobic Paper via Scalable Nonsolvent Armor Strategy. *ACS Nano*, **2022**, 16 (6), 9442-9451. © 2022 The Authors. Published by American Chemical Society. (***Co-first author**)

In this section, some practical applications based on the normal single-component silicone nanorods were explored by replacing the lab frequently-used glass substrate with the cellulosic-paper-based substrate.

4.2.1 Synthesis and characterizations of the ETCS-SC-SNRs coating

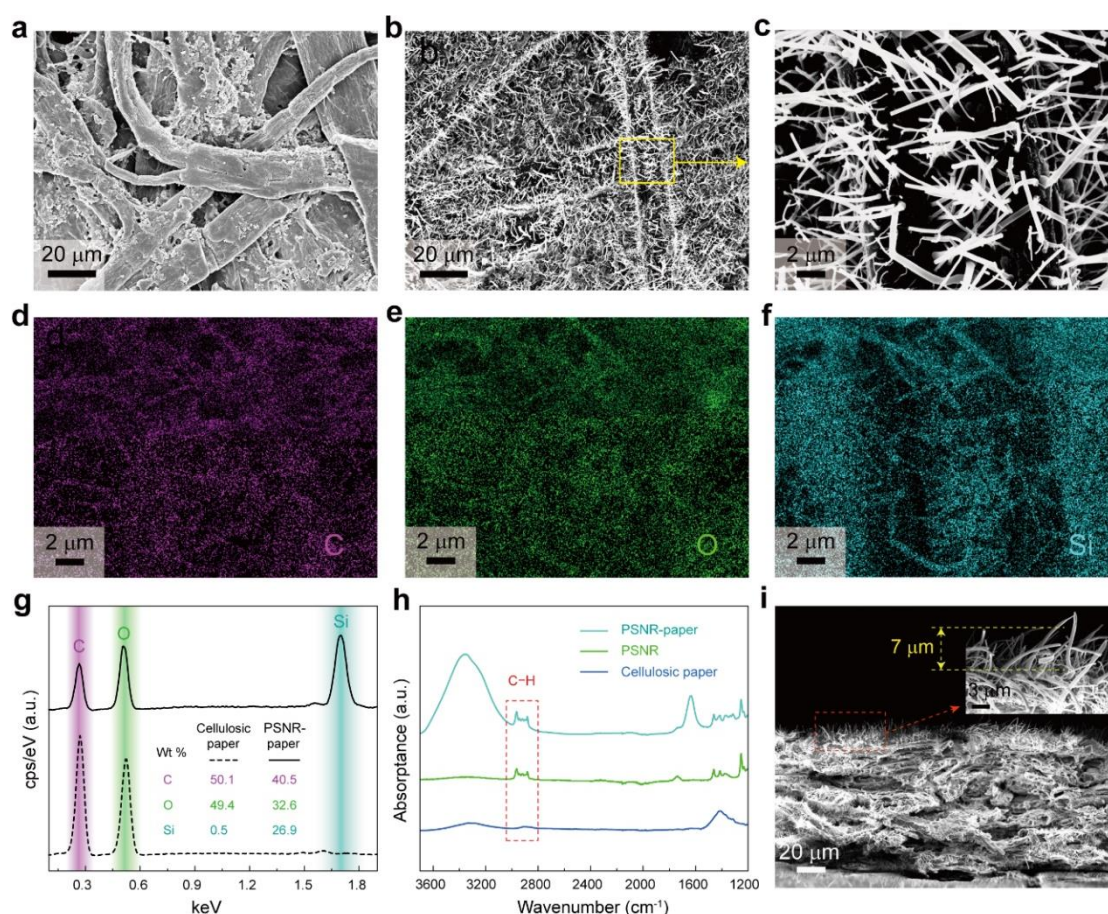


Figure 4.2.1: SEM images of (a) pristine cellulosic paper. (b-c) ETCS-SC-

SNRs¹ on cellulosic-paper-based substrate. (d-f) the corresponding EDX mapping images. (g) EDX spectra of pristine cellulosic paper and ETCS-SC-SNRs coated cellulosic paper. (h) ATR-FT-IR spectra of pristine cellulosic paper, ETCS-SC-SNRs coated cellulosic paper, and pure ETCS-SC-SNRs. (i) SEM images of the cross-section of ETCS-SC-SNRs decorated cellulosic paper. Reprinted with permission from[25].

The optimal growth conditions of *VOL*: 800 μ L, *RH*: 50% \pm 1%, and *RT*: 120 min under room temperature are employed in fabricating ETCS-SC-SNRs on cellulosic-paper-based substrate. The ETCS-SC-SNRs decorated cellulosic paper is abbreviated as SNRs-paper in the following texts. As shown in **Figure 4.2.1.a-c**, SEM images show the surface morphology of both pristine cellulosic paper and SNRs-paper. An obvious improvement of surface roughness at the nanoscale level can be observed from the surface-engineered SNRs-paper compared to pristine cellulosic paper. It is demonstrated that the synthesized ETCS-SC-SNRs coating endows the fibrous texture of pristine cellulosic paper with a micro-nano hierarchical morphology. The homogeneity of the functional coating is further analyzed by acquiring SEM-EDX mapping images (**Figure 4.2.1.d-f**), from where the elements C, O, and Si are proved to be uniformly distributed on the paper surface, especially, the element Si is particularly concentrated on the ETCS-SC-SNRs.

The increase of Si content on the surface of the SNRs-paper can be clearly observed from the SEM-EDX spectra (**Figure 4.2.1.g**). Compared to the pristine cellulosic paper, a new peak (Si) with the element weight percentage value of \sim 27 wt% is proof of successful paper surface decoration by ETCS-SC-SNRs.

In addition, the C-H vibrations of the CH₃ group in the band range of 2950 cm⁻¹ to 2900 cm⁻¹ [139, 140]acquired from the FT-IR spectra (**Figure 4.2.1.h**) can only be observed from the SNRs-paper and pure ETCS-SC-SNRs² samples, which further verifies the ETCS-SC-SNRs are successfully loaded on the surface of pristine cellulosic paper.

The geometrical parameters of the decorated ETCS-SC-SNRs are characterized by performing the cross-sectional SEM images (**Figure 4.2.1.i**), from where the average

¹ ETCS-SC-SNRs is used according to a unified naming standard in this thesis. PSNR is the abbreviation of polysilsesquioxane nanorods used in our published paper, which is the same with silicone nanorods (SNRs) used in this thesis.

² Pure ETCS-SC-SNRs samples were obtained by scraping the surface of the SNRs-coated glass slide, as mentioned in section 3.1.2.

coating layer thickness, $7.0 \mu\text{m} \pm 1.3 \mu\text{m}$, and the average diameter of the single ETCS-SC-SNR, $489 \text{ nm} \pm 71 \text{ nm}$, are obtained separately. In the meantime, the average weight percentage of the grafted ETCS-SC-SNRs, $19.8 \text{ wt}\% \pm 1.1 \text{ wt}\%$, is determined by weighting the cellulosic paper before and after decoration with ETCS-SC-SNRs.

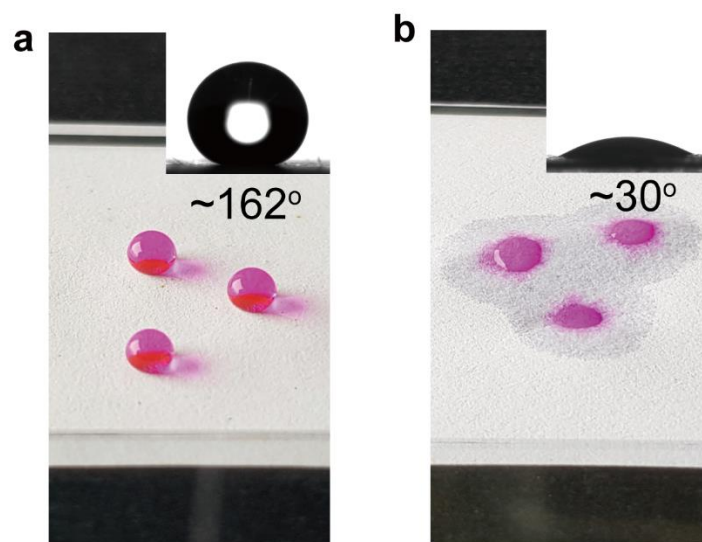


Figure 4.2.2: Picture showing (a) water droplets ($10 \mu\text{L}$) spherically sitting on the SNRs-paper surface and (b) the cellulosic paper wetted by water. The used water was dyed with Rhodamine B. Reprinted with permission from [25].

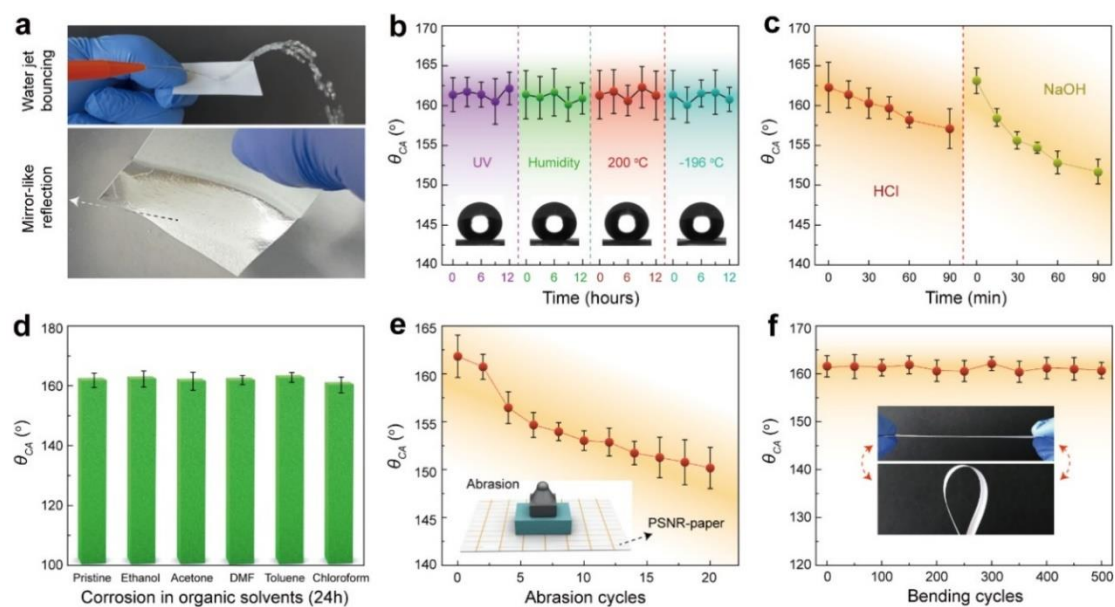


Figure 4.2.3: Robust superhydrophobicity of the SNRs-paper. (a) Water jet bounces on the surface of SNRs-paper and the mirror-like reflection observed from the SNRs-paper when it is immersed in water. (b)

Environmental durability tests of SNRs-paper in the environments of: UV illumination, 90% *RH*, and extreme temperatures (-196 °C in liquid N₂ and 200 °C in lab oven). Insert is the θ_{WCA} measurement after test. (c) Effect of corrosion time in HCl (0.1 M) and NaOH (0.1 M) on water-resistance of SNRs-paper. (d) θ_{WCA} of SNRs-paper after 24 h immersion in different organic solvents. Plot of θ_{WCA} as a function of (e) linear abrasion and (f) bending cycles. Inserts are the schemes of the corresponding tests. Reprinted with permission from[25].

4.2.2 Robust superhydrophobicity of the SNRs-paper

As shown in **Figure 4.2.2**, the surface of the SNRs-paper presents excellent water resistance with a high θ_{WCA} of $162^\circ \pm 2^\circ$ while the pristine cellulosic paper is hydrophilic with a low θ_{WCA} of $\sim 30^\circ$ and can be easily wetted by water droplets. The water jet bouncing test (**Figure 4.2.3.a**) as well as the mirror-like reflection observed when the SNRs-paper is immersed in water, demonstrate the robust superhydrophobicity of the SNRs-paper. Especially, the surface of the SNRs-paper remains un-wetting after being taken out from the water, further indicating the existence of the trapped air-layer[112] at the solid-liquid interface, namely, the contact area between the SNRs-paper surface and water. The high surface roughness resulting from the micro-nano hierarchical structure after decorating by ETCS-SC-SNRs and the inherent low-surface-energy property of the ETCS-based silicone materials may collectively contribute to the excellent water-resistance property of the SNRs-paper surface[141, 142].

Chemical, mechanical, and extreme environmental durability of the functional coatings are considered significant properties in practical applications. Therefore, the as-prepared SNRs-papers were tested in various conditions, and their water-repellent ability was examined at a certain time interval by measuring the surface θ_{WCA} , as shown in **Figure 4.2.3.b-f**. In the environmental durability tests, the SNRs-paper samples were separately placed in some extreme environments, for example, UV illumination with the wavelength of 350 nm, extreme moisture environment with *RH* over 90%, low temperature in the liquid N₂, and high temperature in the lab oven (~ 200 °C). After being exposed to the above environments for 12 h, no obvious change in θ_{WCA} can be detected (**Figure 4.2.3.b**), indicating the excellent environmental durability of the engineered SNRs-paper.

In addition, SNRs-paper shows excellent performance in chemical durability tests. For example, the θ_{WCA} measured from the SNRs-paper samples that have been separately immersed in strong acidic (HCl, 0.1 M) and basic (NaOH, 0.1 M) aqueous solutions for 90 min are still more than 150° in spite of a slight decrease (**Figure 4.2.3.c**). Moreover, the prepared SNRs-paper samples are able to maintain superhydrophobicity with θ_{WCA} even more than 160° after being treated in various polar and nonpolar organic solvents, including acetone, EtOH, DMF, toluene, and chloroform for 24 h as shown in **Figure 4.2.3.d**. SEM images presented in **Figure 4.2.4** exhibit the surface texture of the SNRs-paper after treatment in several harsh chemical conditions. Surprisingly, the morphology of the ETCS-SC-SNRs coating layer remains unchanged after treatment in corrosive HCl and NaOH liquids, although some collapses are observed after being exposed to organic solvents, which can be explained by the capillary force induced by the N_2 -flow drying¹ process[143, 144]. The excellent durability of the ETCS-SC-SNRs layer towards chemical perturbations can be ascribed to their inert low-surface-energy chemical compositions and the cross-linked structures[1, 24].

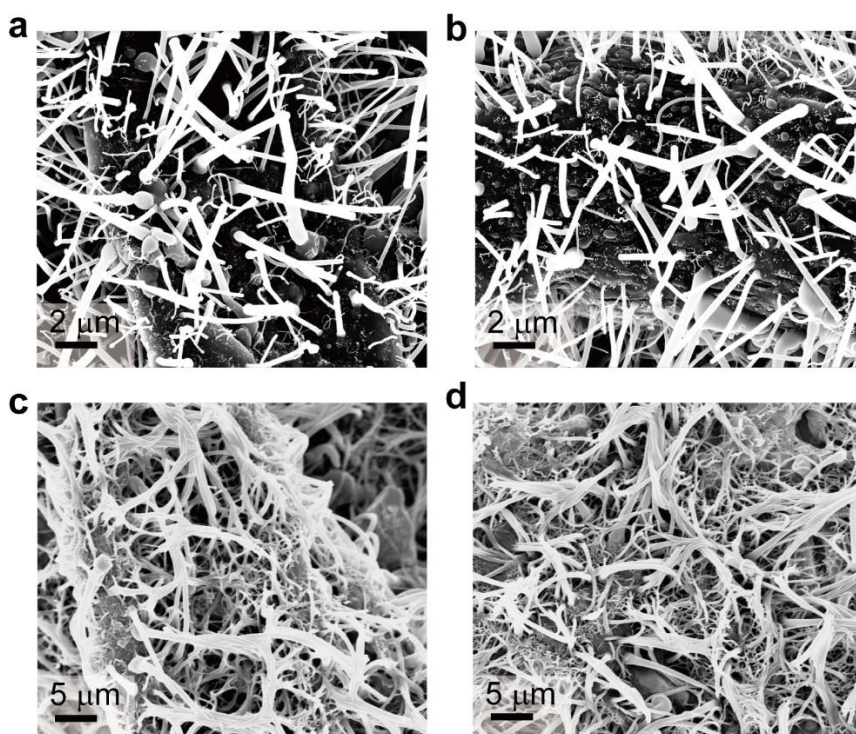


Figure 4.2.4: SEM images of the SNRs-paper surface after treatment with (a) HCl, (b) NaOH, (c) DMF, and (d) toluene. Reprinted with permission

¹ A better drying method that can maintain the surface topology unaffected is necessary for further studies. This will be discussed in section 4.4.

from[25].

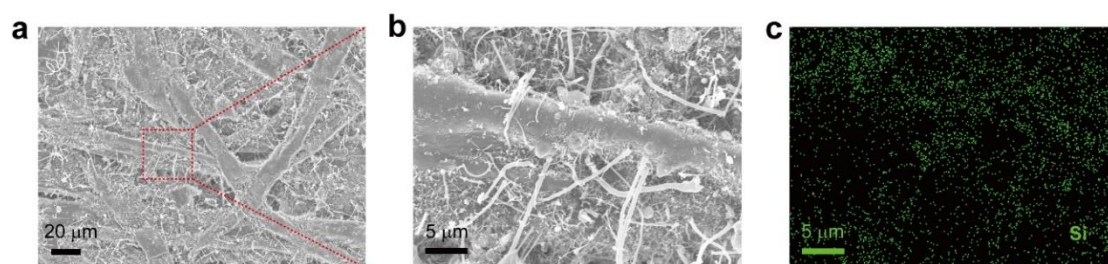


Figure 4.2.5: (a-b) SEM images and (c) corresponding EDX mapping image of the SNRs-paper surface after 20 cycles of linear abrasion. Reprinted with permission from[25].

Linear abrasion and cyclic bending tests were employed to evaluate the mechanical durability and flexibility of the SNRs-paper. As shown in **Figure 4.2.3.e-f**, SNRs-paper remains superhydrophobic after 20 cycles of linear abrasion and 500 cycles of bending test, respectively. Especially after the bending test, even a constant $\theta_{WCA} (> 160^\circ)$ is maintained. Their excellent, durable water-repellent property resulted from the remaining residual ETCS-SC-SNRs layer after mechanical damage, as shown in **Figure 4.2.5**, which is preserved through the protection from inherent micro-cellulose fibers of the cellulosic paper[15].

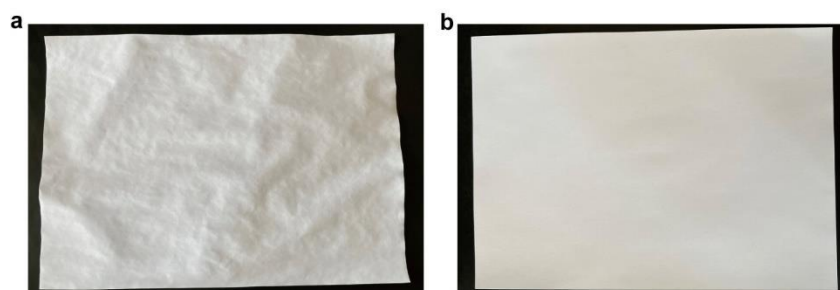


Figure 4.2.6: Superhydrophobic treatment of A4-paper by (a) wet-chemical method and (b) ETCS-SC-SNRs coating. Reprinted with permission from[25].

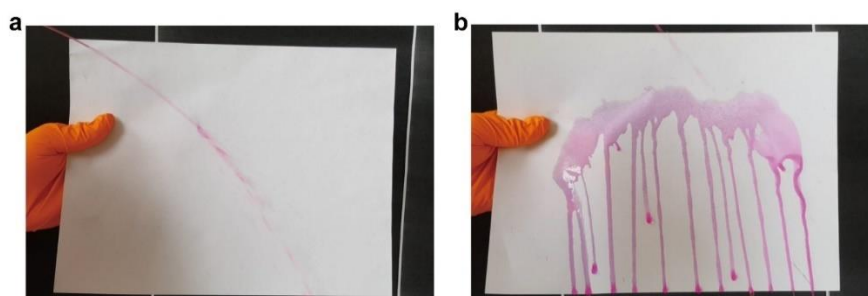


Figure 4.2.7: Water-repellent property of the (a) SNRs-A4-paper and (b) pristine A4-paper. Reprinted with permission from[25].

4.2.3 Scale-up fabrication

In order to extend practical applications of the SNRs-paper, the scale-up coatings were performed using commercial A4-paper (297 mm x 210 mm) in a bigger custom-built reaction chamber (12 L). Corresponding synthetic parameters, more *VOL* (2000 μL) and longer *RT* (360 min) were applied to fit with the new reaction environment. Similarly, the appearance of the cellulosic A4-paper remains the same after decoration with ETCS-SC-SNRs. As a comparison, the surface of A4-paper after superhydrophobic treatment by conventional wet-chemical method¹ is wrinkled and curled after solvent evaporation because of the reduced adhesion and the stretching of the cellulose fibers after soaking in EtOH (**Figure 4.2.6**). Moreover, as shown in **Figure 4.2.7**, the obtained SNRs-A4-paper shows excellent water resistance toward the water jet, whereas the pristine A4-paper is easily wetted.

4.2.4 Printability and writability of the SNRs-paper

Engineered SNRs-A4-paper can be directly utilized in commercial inkjet printer (Expression Premium XP-6100 color inkjet printer with Claria Premium Ink) because their appearance and integrity are well maintained after being armored with ETCS-SC-SNRs. Excellent printability of the SNRs-A4-paper is doubtless as almost no difference can be visually perceived from both SNRs-A4-paper and pristine-A4-paper after being printed with the same content (**Figure 4.2.8.a-b**). Notably, printed SNRs-A4-paper is still able to re-bounce water jet² and exhibits waterproof functionality from the areas both covered and non-covered by oily ink (**Figure 4.2.9**). Similar results can also be observed from the handwritten SNRs-paper (**Figure 4.2.8.c**). An ink diffusion test was therefore conducted to evaluate the protective ability of the SNRs-paper to the handwritten content on its surface. After 12 h exposure to water, the content written with customized-made water-soluble ink³ was perfectly preserved by the engineered SNRs-A4-paper, whereas the ink on untreated cellulosic paper was thoroughly

¹ Hydrophobic SiO₂ nanoparticles dispersed in EtOH with a concentration of 0.1 g·ml⁻¹.

² Muddy water in **Figure 4.2.8**: 10 g of soil dispersed in 200 mL of water.

³ 200 mg of Rhodamine B dissolved in 10 mL of ethanol.

dissolved in water¹ (Figure 4.2.8.d-e). Moreover, measured θ_{WCA} (Figure 4.2.8.f) further demonstrates that the as-prepared SNRs-paper possesses excellent water-resistance, printability, and writability.

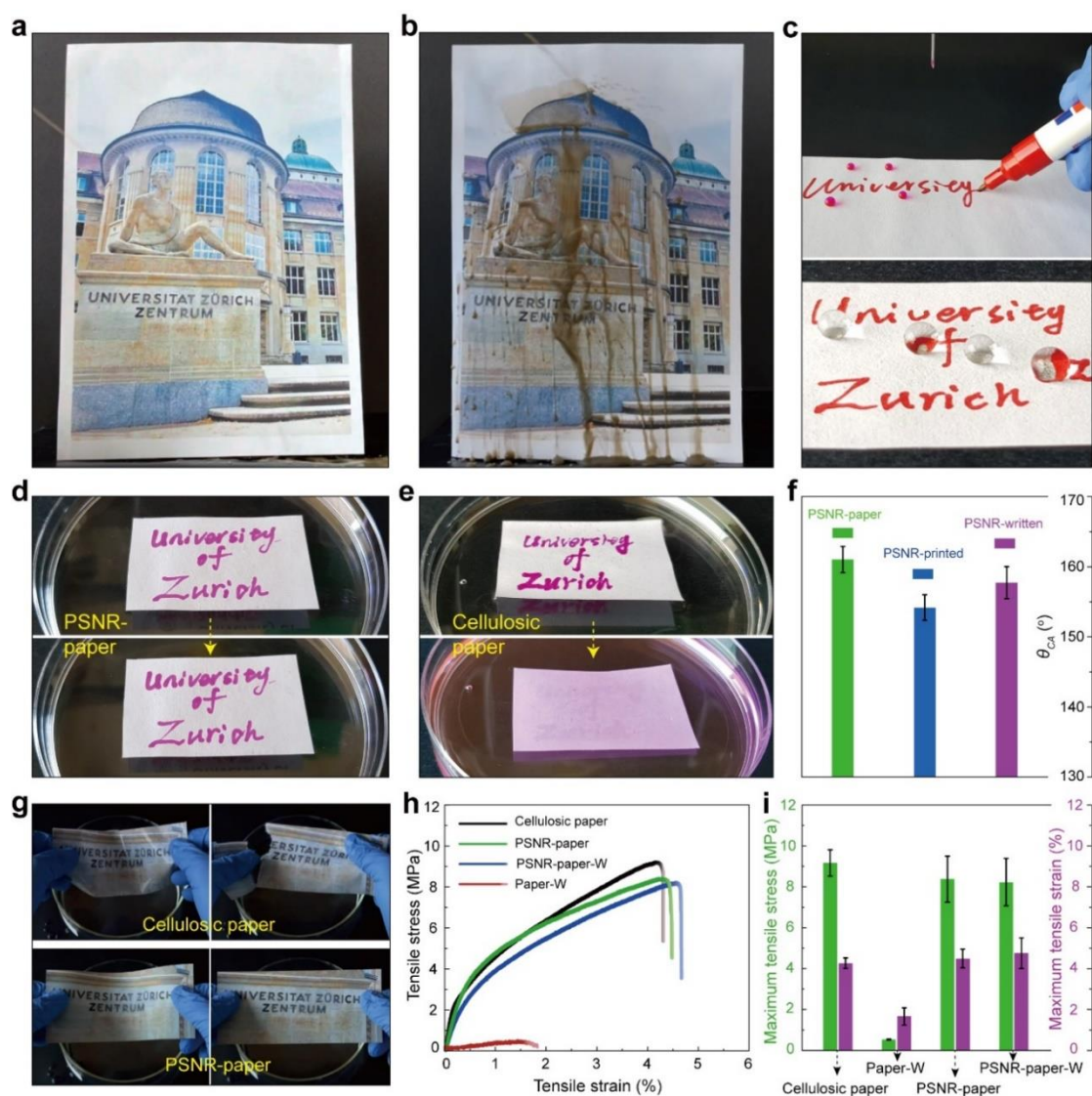


Figure 4.2.8: Pictures showing water jet bounces off (a) SNRs-A4-paper and (b) pristine-A4-paer after being printed with the same content. (c) Writability of the SNRs-paper and its superhydrophobic performance after writing. (d-e) Comparison of water-resistance of handwriting on SNRs-paper and pristine cellulose paper. (f) Measured θ_{WCA} of SNRs-paper after printing and handwriting. (g) Integrity check of the printed SNRs-paper and pristine cellulose paper after being immersed in water. Comparison of (h) tensile tests and (i) calculated maximum tensile stress and strain of the

¹ The process is completed in a few seconds due to the quick infiltration of water.

SNRs-paper and pristine cellulosic paper before and after water-exposure treatment (symbol -W is used to represent the water-exposure treatment). Reprinted with permission from[25].



Figure 4.2.9: Pictures showing water droplets (10 μL) spherically contact with the printed SNRs-A4-paper. Reprinted with permission from[25].

The oleophilic and hydrophobic ETCS-SC-SNRs decorated on cellulosic papers play a significant role in simultaneously keeping the surface superhydrophobic and having excellent printability and writability. The capillary wetting and the air cushion formed when contact with ink and water, respectively, are resulted from the geometrical micro-nano structures together with the inherent oleophilicity of the surface-exposed ethyl groups. As shown in **Figure 4.2.10**, a droplet of ink used in the printer was placed on the surface of the SNRs-paper, and a rapid absorption can occur in a very short time with the final measurement of contact angle very close to 0.

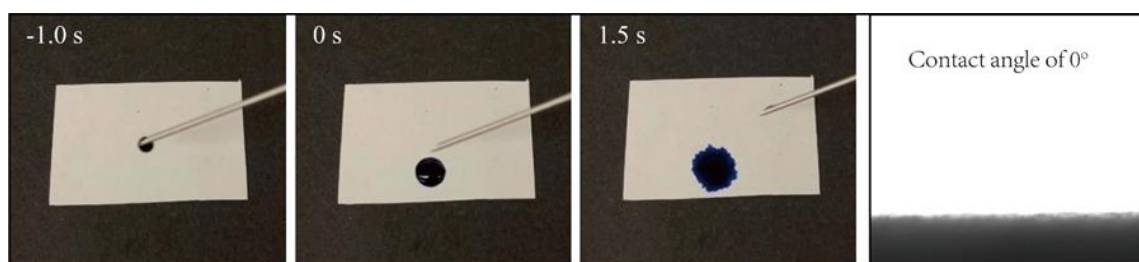


Figure 4.2.10: Rapid absorption and complete wetting of the ink on SNRs-paper surface. Reprinted with permission from[25].

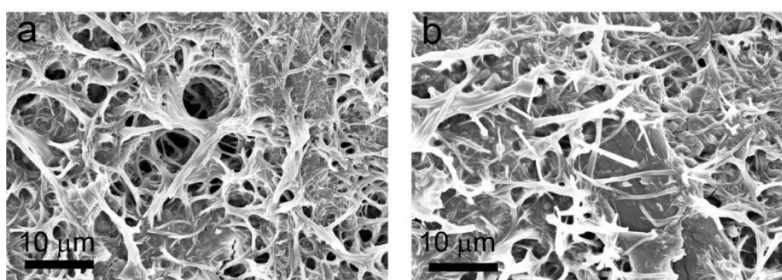


Figure 4.2.11: SEM images of PSNR-paper after (a) handwriting and (b)

printing. Reprinted with permission from[25].

Collapse and entanglement of the ETCS-SC-SNRs observed from SEM images after respective handwriting and printing (**Figure 4.2.11**) are ascribed to the capillary effect induced during the drying process of the ink, but their retention leads to a new roughness at the microscale, which may contribute to the sustained excellent water-repellency and integrity of the printed and handwritten SNRs-papers.

As shown in **Figure 4.2.8.g**, after immersion in water for the same time, the printed pristine cellulosic paper is fully wetted and easily damaged because of its hydrophilic nature, whereas the SNRs-paper that is printed with the same content as the pristine cellulosic paper remains dry and exhibits strong resistance against tearing force. To further evaluate the mechanical properties of the papers that have either or not been treated by water, tensile measurements (introduced in section **3.6.2**) were therefore conducted (**Figure 4.2.8.h-i**). Before contacting with water, a comparable result with tensile strength of ~ 9.0 MPa and strain of $\sim 4.5\%$ is seen from SNRs-paper compared to pristine paper, which illustrates that the decoration of ETCS-SC-SNRs coating has no influence on the mechanical properties. However, after being treated with water, a huge decrease in both tensile strength and strain can be observed from pristine cellulosic paper samples, whereas the SNRs-paper still maintains almost the same tensile measurement results, indicating the enhancement of water-resistance and integrity of the surface-engineered cellulosic papers even after printing.

4.2.5 Applying ETCS-SC-SNRs on preprinted cellulosic-paper-based substrate

To further improve the applicability of the surface-engineered cellulosic paper in the real world, an additional synthesis strategy, synthesizing the ETCS-SC-SNRs coatings on cellulosic paper that has been preprinted with some contents, was developed. Compared to some conventional methods, from which the preprinted contents based on cellulosic paper may be irreversibly damaged after hydrophobic treatment, such as wet-chemical method (**Figure 4.2.12**), or the readability might be unacceptably affected because of the created micro-nano surface rough structures, the method of synthesizing SNRs on preprinted paper (SNRs-p-paper) shows excellent performance in maintaining the appearance and readability of the original materials (**Figure 4.2.13.a-b**).



Figure 4.2.12: Preprinted cellulosic paper treated with wet-chemical method showing deformation and wrinkling of the paper and damage of the printed content due to ink diffusion. Reprinted with permission from [25].

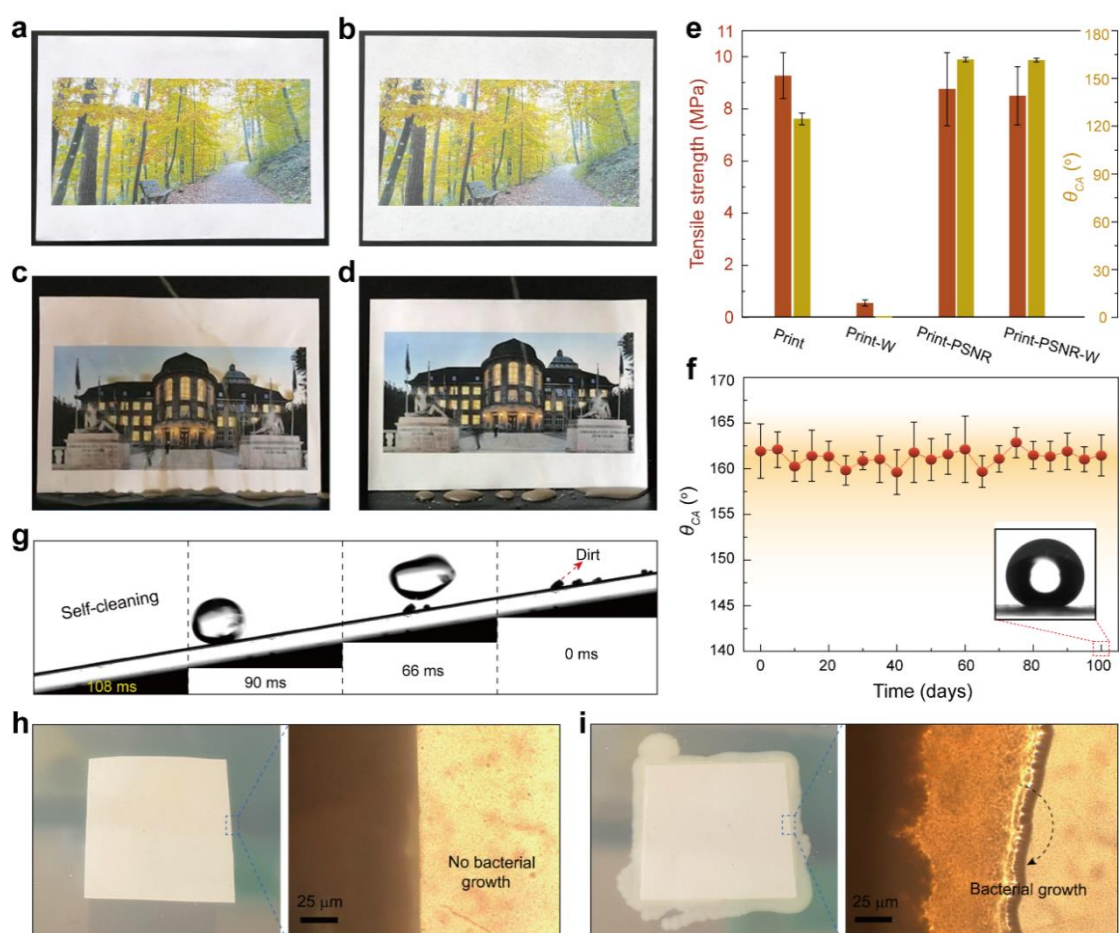


Figure 4.2.13: Preprinted cellulosic paper (a) before and (b) after decorated with ETCS-SC-SNRs coating. Muddy water jet on (c) untreated preprinted cellulosic paper and (d) SNRs-p-paper. (e) Measurement of θ_{wca} and tensile

strength for the preprinted cellulosic paper before and after hydrophobic treatment with ETCS-SC-SNRs (Symbol -W is used to represent the water-exposure treatment). (f) Long-term durability of the SNRs-p-paper under ambient conditions with insert is θ_{WCA} measurement at 100 days. (g) Self-cleaning ability of the SNRs-p-paper after long-term storage (100 days) under ambient conditions. Biological test of the (h) SNRs-p-paper and (i) untreated preprinted cellulosic paper. Reprinted with permission from [25]. Image in (c and d) is used with permission from University of Zurich [145].
© 2010 UZH Ursula Meisser.

The engineered micro-nano surface roughness, as well as the inherent low-surface-energy [146] of the alky-based silicone materials, collectively result in the excellent water-resistance and self-cleaning ability of the ETCS-SC-SNRs modified cellulosic paper prints. As shown in **Figure 4.2.13.c-e**, SNRs-p-paper can hardly be contaminated by muddy water jets and shows a high θ_{WCA} of $\sim 160^\circ$ that can be maintained even after being exposed to water for a very long time. On the contrary, untreated prints with measured θ_{WCA} of $\sim 120^\circ$ can immediately become superhydrophilic after exposure to water.

Tensile measurement was performed again to evaluate the mechanical properties of SNRs-p-paper. Similar conclusions as the SNRs-paper can be drawn that the coated ETCS-SC-SNRs on the surface of preprinted cellulosic papers does not compromise their mechanical properties because a comparable tensile strength can be observed from SNRs-p-paper compared to untreated cellulosic paper samples. Detaching of the cellulose fibers caused by water infiltration is effectively prevented because of the excellent waterproof functionality of SNRs-p-paper. Therefore, the modified cellulosic paper prints exhibit enhanced integrity and strength against water exposure.

In order to investigate the longevity of SNRs-p-paper under normal environment, a sample is stored at ambient lab conditions, and its surface θ_{WCA} is measured periodically. Surprisingly, even after 100 days of exposure, the SNRs-p-paper still shows superhydrophobic properties with a quite stable θ_{WCA} of $\sim 160^\circ$ (**Figure 4.2.13.f**). Meanwhile, its self-cleaning ability is also well preserved, as shown in **Figure 4.2.13.g**, a rolling-off water droplet (10 μL) can easily take away dirt and dust contaminations from the sample surface.

4.2.6 Antimicrobial functionality

The biological test was conducted to prove that the ETCS-SC-SNRs modified substrate surface has excellent antimicrobial functionality. Owing to the intrinsic superhydrophobicity of the SNRs-paper surface, necessary growth conditions for microorganisms, namely, moisture and nutrients, can hardly be created and maintained. Moreover, the adhesion of bacteria on modified paper surfaces is significantly reduced because of less contact area resulting from the hierarchically structured surface[147]. Therefore, after 24 h exposure of SNRs-paper and pristine cellulosic paper to bacterial species under optimal growing conditions, no visible microbial growth can be detected from the modified sample, whereas a large number of bacterial colonies are clearly observed from the perimeter and surface of the untreated cellulosic paper (**Figure 4.2.13.h-i**).

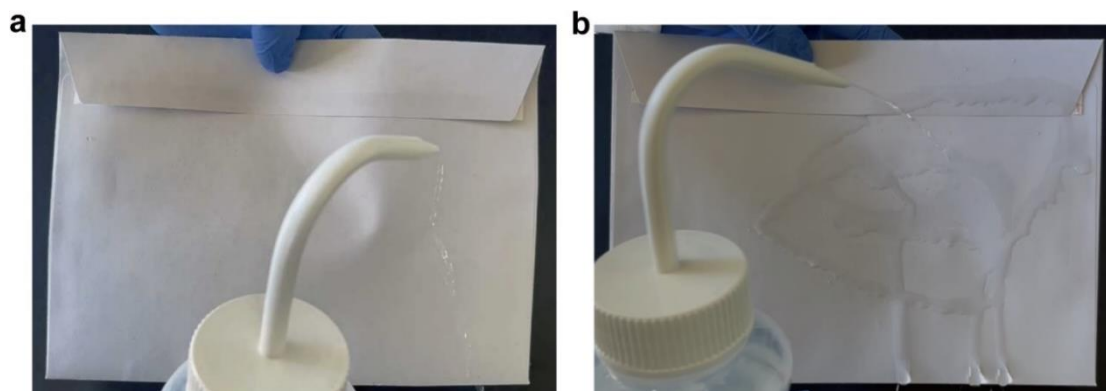


Figure 4.2.14: (a) Water jet bounces off the letter envelope armored with ETCS-SC-SNRs, indicating good waterproof functionality. (b) Water sticks to and penetrates a commonly used letter envelope. Reprinted with permission from[25].



Figure 4.2.15: Water jet bounces off the package box decorated with ETCS-SC-SNRs.

4.2.7 Other cellulosic-paper-based substrates

Replicating ETCS-SC-SNRs coatings on other cellulosic-paper-based substrates such as letter envelopes, papers, printings, and packaging materials to provide surface protection for outdoor use is of practical interest. Some special treatments, e.g., oxygen plasma, might be required before doing coatings on different paper-based items. As shown in **Figure 4.2.14** to **Figure 4.2.15**, the modified envelopes and packaging boxes exhibit well-waterproof functionality. Future applications on more common-used paper-based items in various scenarios can be expected as the chemical, mechanical, and environmental durability, excellent water-resistance, self-cleaning ability, and antimicrobial functionality are potentially able to mitigate aging and decomposition processes and extend the service life of cellulosic-paper-based materials.

4.3 Synthesis and applications of the bamboo-shaped SC-SNRs

Some parts of this chapter have been published: **Kangwei Chen**, Shanqiu Liu, Yuen-Yee Lau & Stefan Seeger, One-Step Synthesis of Dynamically Shaped Stiff Nanorods Using Soft Silicone Materials to Control Water Repulsion and Collection. *Small*, **2022**, 18 (40), 2203820. © 2022 The Authors. Small published by Wiley-VCH GmbH.

As mentioned in previous chapters, surface roughness, more specifically, geometric parameters of the surface structure, are considered one of the key factors in deciding the physicochemical properties of the solid surface[35, 37]. However, limited to the inevitable vulnerability and irregularity of the majority of silicone-based nanomaterials produced by conventional methods, it is still challenging to synthesize morphology-controlled nanostructures on demand and expand their applications to a wider range of fields. In this chapter, a dynamic Droplet Assisted Growth and Shaping (d-DAGS) strategy is developed based on our group's previous studies, and the growth mechanism, physicochemical properties, and potential applications of the newly synthesized bamboo-shaped SC-SNRs are systematically investigated.

4.3.1 d-DAGS mechanism

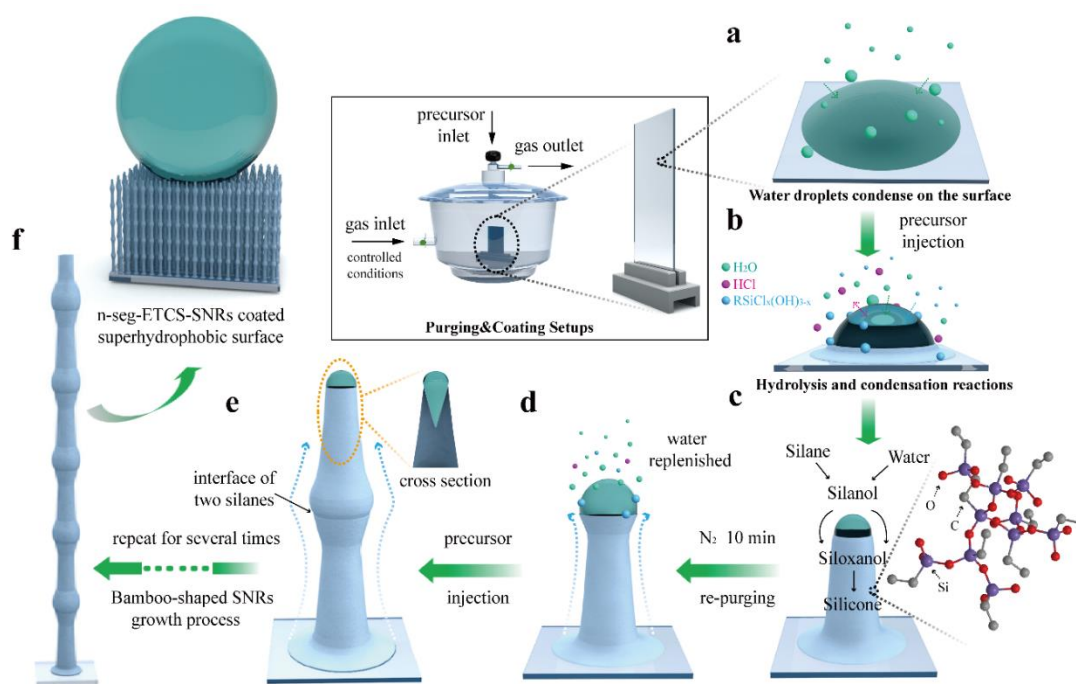
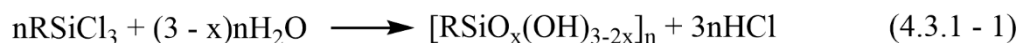


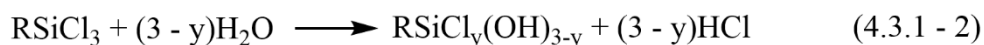
Figure 4.3.1: Schematic illustration of the d-DAGS mechanism. (a) Condensed water droplet on substrate surface after pretreatment-S3. (b) Hydrolysis and condensation reactions triggered after injecting ETCS precursor. (c) Absorption of soluble species by condensed water droplet and the start of the deposition process of insoluble silicone species. (d) Goblet-shape of the SNRs after reactions-S7. (e) Growth of the second segment. (f) Final morphology of the bamboo-shaped SNRs. Reprinted with permission from[23].

Based on the DAGS method that has been introduced in Chapter 2, the d-DAGS mechanism is developed to achieve morphologically controllable synthesis of silicone-based nanostructures. Precise and dynamic control over reaction parameters is significant for the entire growth process. Therefore, to better understand the growth mechanism, a deep investigation focusing on each single growth step was conducted with the help of various electronic microscopies.

The schematic illustration is presented in **Figure 4.3.1**. Micro- and nano-water droplets are able to condense on the activated glass substrate surface after 1 h equilibrium by moisture N_2 gas flow at a certain RH (60% used for bamboo-shaped SNRs growth) inside the custom-built reaction chamber because of the chemical or topographic heterogeneities of the substrate (**Figure 4.3.1.a**) [104, 105, 148]. Liquid precursor ETCS (400 μ L) is then slowly injected into the chemical holder dish through the septum in the middle of the reactor lid, and it is supposed to volatilize immediately to react with water in the gas phase. Soluble reactants and intermediate products are rapidly attracted and dissolved into tiny water droplets. The entire growth process is based on the self-catalytic hydrolysis and deposition reactions[22] as the by-product HCl released during the reactions can be worked as a catalyst due to their high solubility and rapid accumulation in the aqueous phase. As illustrated in **Figure 4.3.1.b**, soluble intermediate species such as silanol and siloxanol that are continuously produced from the hydrolysis reactions (**Eq. 4.3.1**) are further dissolved into the condensed water droplets, leading to the generation of the insoluble polysiloxane and the activity reduction of the water droplet (**Figure 4.3.1.c**).



$$0 < x \leq 1.5$$



R = Ethyl group; y = 0, 1, 2

The diameter of the synthesized 1D silicone material is obviously getting smaller along the growth direction (bottom to top) due to the volume of water droplets sitting at the top cavity being gradually consumed during the deposition and growing process, which indicates the assistance and shaping functionality of the droplet (water) in DAGS mechanism. Although the water droplet at the top can be theoretically replenished from the gas phase because of the thermodynamic equilibration[22], the effect is not significant due to the continuous hydrolysis and condensation reactions and the considerable decrease of *RH* surrounding the samples. A bent-growth tendency can be expected if the growth process continues, which will result in the formation of conventional SNFs with a slightly bigger base diameter. The hydrolysis and condensation reactions will eventually cease until the water droplets are not able to dissolve more soluble silanol and siloxanol species for further depositions. Therefore, an appropriate control over reaction time is important in forming silicone nanostructures on demand.

In order to keep SNRs growing upright, a dynamic adjustment over reaction conditions is developed. After 10 min of hydrolysis and condensation reactions inside the closed reaction chamber, both inlet and outlet gas valves were opened for the second purging process by moisture N₂ gas (*RH*: 60%). A short re-purging time (10 min) is used to avoid bend-growing of the structure. During this time, most of the volatilized unreacted ETCS residues are basically removed from the reaction chamber, and the *RH* inside the reaction environment returns to the initial level and enables to accelerate the replenishment of the water droplet according to the thermodynamic equilibration. Meanwhile, because of the continuous hydrolysis and condensation reactions, the deposition of polysiloxane is ongoing with increasing the volume of the water droplet sitting at the top cavity, resulting in the diameter increase of the deposited silicone nanostructures (**Figure 4.3.1.d**). A goblet-shaped silicone nanostructure is therefore obtained for this reason (**Figure 4.3.2**). Meanwhile, the “tip-growth” model of the

DAGS method can be proved, which illustrates that the water droplet is sitting on the top cavity rather than the bottom of the nanostructure during the whole growing process due to the precipitation of the polysiloxane and weak interactions between solid surface and water droplet[149].

With the injection of the second round of precursor, more reactants are provided for the continuous hydrolysis and condensation reactions. A similar growth process with the base segment can be observed from the second segment after 10 min reaction, i.e., a sharpening growth tendency caused by the consummation of the volume of water droplet (**Figure 4.3.1.e**). The shape, more specifically, the width of the synthesized SNRs, is determined by the diameter of the water droplet staying at the top cavity.

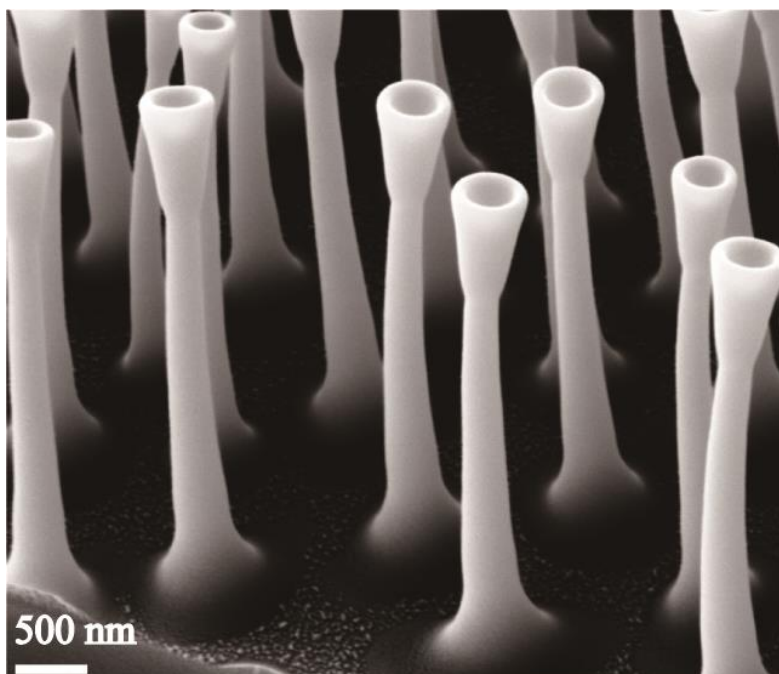


Figure 4.3.2: SEM images of a ‘goblet-shape’ structure of SNRs after re-purging with N₂ gas (RH 70%) for 10 min. Reprinted with permission from[23].

An obvious interface line shown after the second injection of precursor and the formation of the “bamboo-knot” indicates the recovery of the activity of the water droplet after replenishments and also represents the new round deposition of the newly synthesized polysiloxane. Additionally, a clear conical cavity on the top segment of the formed SNRs can be observed from the SEM and TEM images (**Figure 4.3.3**), which illustrates that the deposition process, namely, accumulation of polysiloxane, is from the liquid-air interface towards water droplet center (**Figure 4.3.1.e**).

Finally, the specially designed single-component bamboo-shaped SNRs with the specific number of segments are synthesized by applying the repetitive dynamic regulation strategy to tune the growth conditions on demand accompanied by the periodic purging and injection of precursors (**Figure 4.3.1.f**). Notably, it can be concluded that the shape (volume) of the condensed water droplet plays a decisive role in synthesizing the morphology-controlled silicone nanostructures via the d-DAGS method.

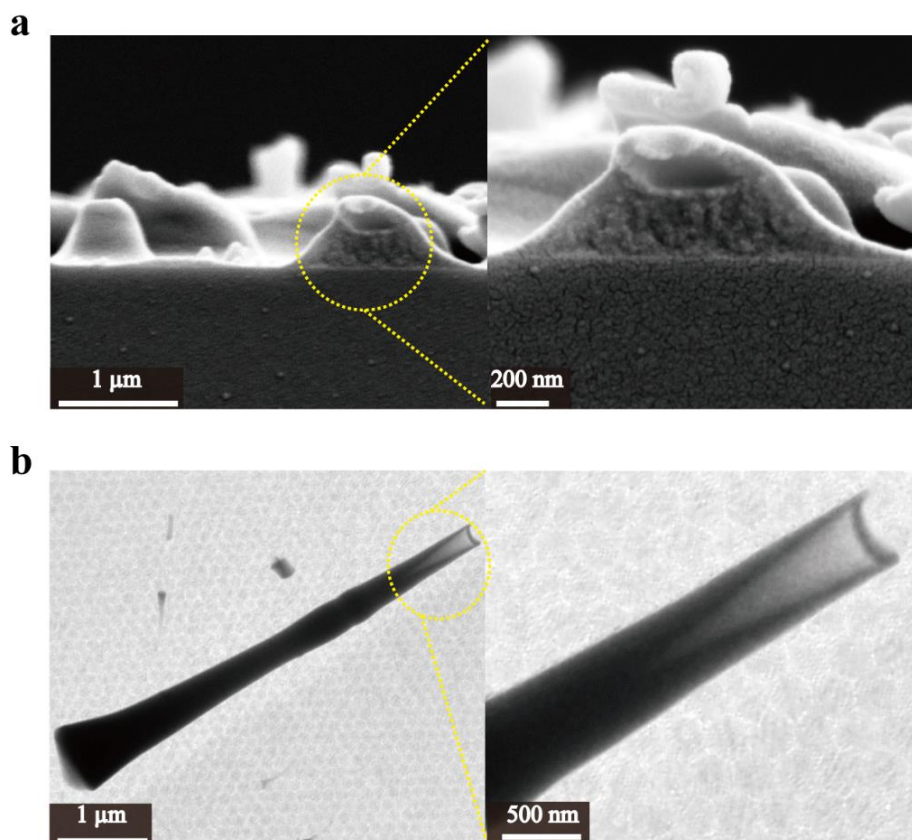


Figure 4.3.3: (a) SEM images of the cross section of ETCS volcanoes, and the magnified image. (b) TEM images of 2-seg-ETCS-SC-SNRs and the magnified image of its tip. Reprinted with permission from[23].

As discussed in section 4.1, synthetic parameters such as RH , RT , precursors, substrates, and temperature[26] collectively affect the morphology of the synthesized silicone nanostructures at micro- and nanoscale when the synthesis is performed in a gas-phase system. The functionalities of each single synthetic parameter have been summarized in section 4.1.4. Optimal reaction conditions of RH 60%, RT 10 min, and VOL 400 μL are eventually employed in fabricating the single segment of bamboo-shaped SNRs after comprehensive considerations regarding topographic characteristics, reaction

efficiency, and surface physicochemical properties.

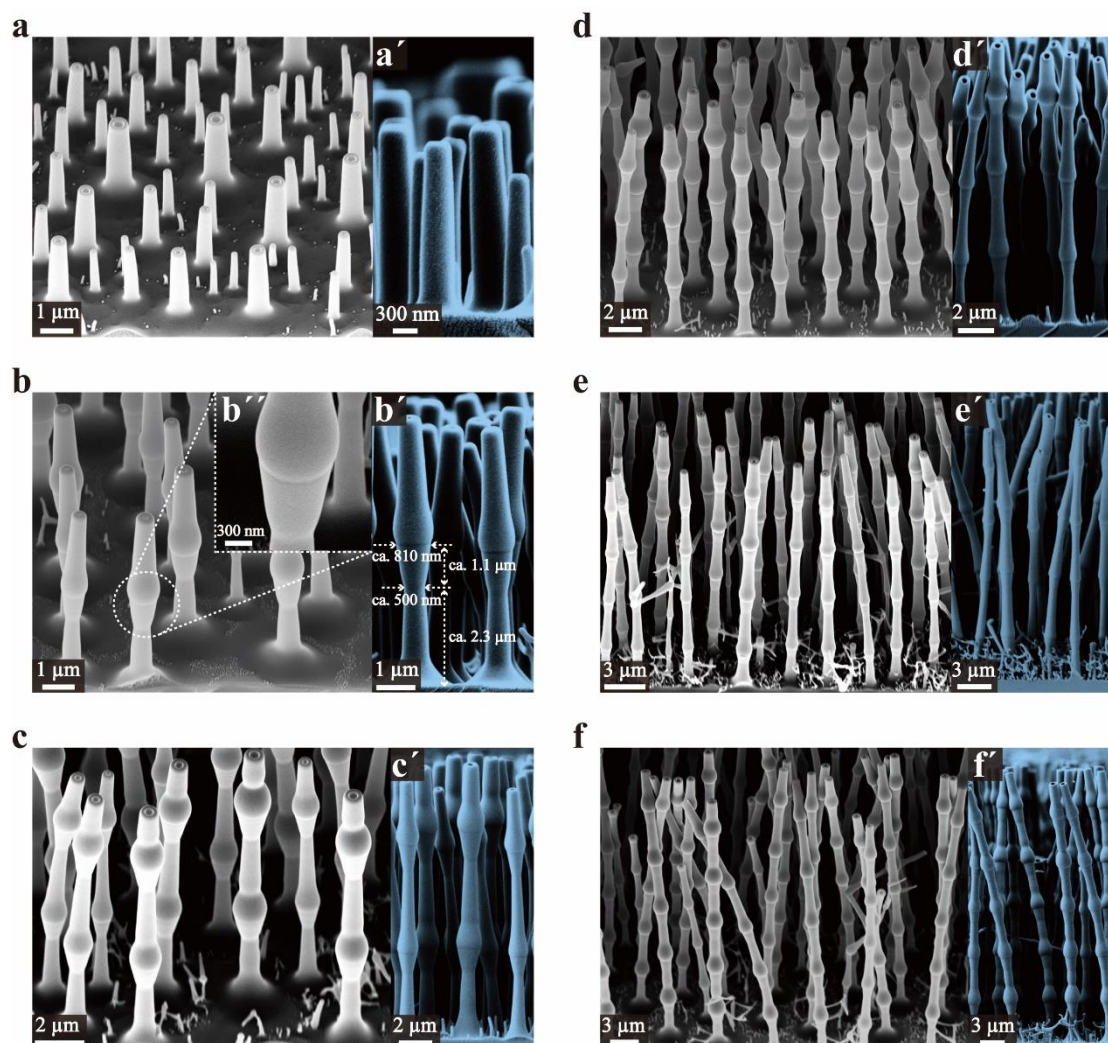


Figure 4.3.4: SEM images of the bamboo-shaped SNRs with segment number of 1 – 6. (a-f) 45° and (a'-f') 90° of tilt angle. Adapted with permission from [23].

4.3.2 Characterizations of the bamboo-shaped SNRs

The uniform arrangement and bamboo shape of the SNRs synthesized via the d-DAGS method are verified by SEM. As shown in **Figure 4.3.4**, an obvious feature of the bamboo-shaped SNRs is that they are able to keep upright compared to conventional filaments, nanowires, fibers, etc. Meanwhile, the “bamboo-knot” (**Figure 4.3.4.b'-b**) can be clearly observed (diameter increase, for example, from 500 nm to 810 nm, is caused by the replenishment of water droplets during the re-purging process), which illustrates the controllability of the segment number of the synthesized bamboo-shaped SNRs as well as the adjustability of the height of the structure, namely, the thickness or

roughness of the surface coating. Every single segment can be clearly distinguished from the SEM images with the diameter varying from ~ 300 nm to ~ 800 nm at the half-height position (**Figure 4.3.5**). The average height is calculated (**Figure 4.3.6**) to be $2.7 \mu\text{m} \pm 0.2 \mu\text{m}$ to $34.6 \mu\text{m} \pm 1.0 \mu\text{m}$ for segments from 1 to 6 as shown in **Figure 4.3.5**.

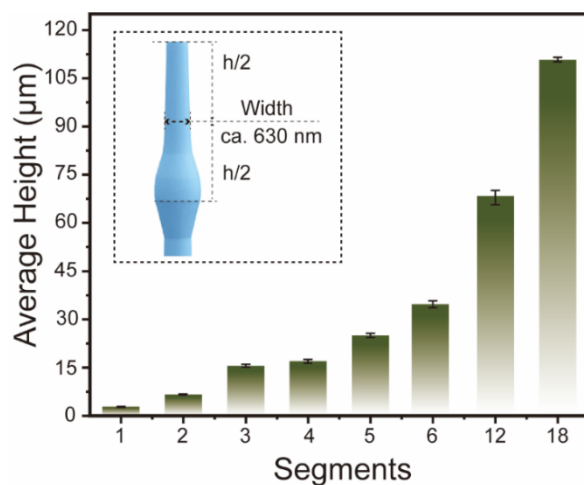


Figure 4.3.5: Average height of the bamboo-shaped SNRs with different number of segments. Insert is showing the diameter measurement at the half height position of the segment. Adapted with permission from[23].

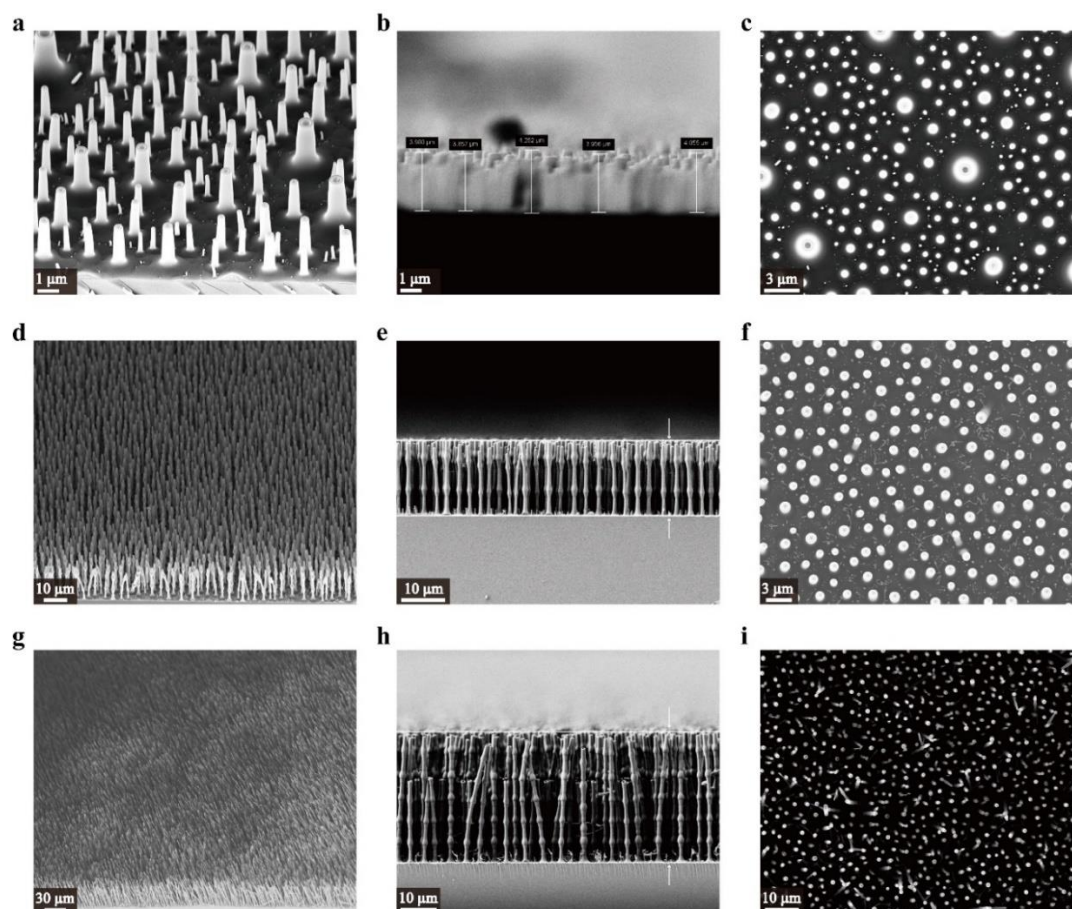


Figure 4.3.6: SEM images of the morphology of bamboo-shaped SNRs. Tilt angle of 45° (a, d, g), 90° (b, e, h), and top view (c, f, i) for 1-seg-ETCS-SC-SNRs (a-c), 3-seg-ETCS-SC-SNRs (d-f), and 6-seg-ETCS-SC-SNRs (g-i), respectively. Reprinted with permission from[23].

Figure 4.3.6 shows the bamboo-shaped SNRs with segment numbers of 1, 3, and 6 from different angles, 45°, 90° (side view), and top view. It is clear that the morphology of all these structures (surface coatings) is extremely regular and uniform. Different numbers of segments are perfectly arranged. STEM-EDX mapping is performed for elemental analysis. As shown in **Figure 4.3.7**, the basic elements, including C, Si, and O, are detected to be uniformly distributed on the segment.

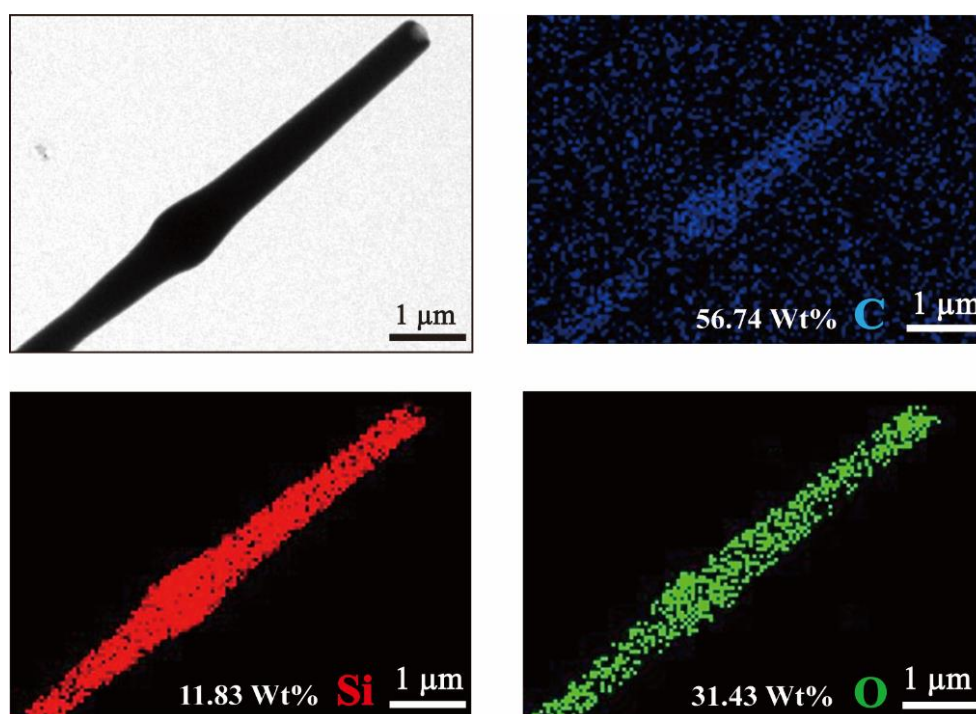


Figure 4.3.7: TEM and corresponding STEM-EDX images of the top segment of 6-seg-ETCS-SC-SNRs. Adapted with permission from[23].

4.3.3 Ultra-long bamboo-shaped SNRs

Ultra-long bamboo-shaped SNRs can be theoretically synthesized via the d-DAGS method to have unlimited length because of the controllability of the segment number. As shown in **Figure 4.3.8**, 12-seg-ETCS-SC-SNRs with an average height of $\sim 67 \mu\text{m}$ (aspect ratio ~ 106) and 18-seg-ETCS-SC-SNRs with an average height of $\sim 111 \mu\text{m}$ (aspect ratio ~ 176) are fabricated through several repeating cycles (\mathbf{R}_{11} and \mathbf{R}_{17}) of

injections and reactions (**Figure 4.3.5**). Despite some collapses and messy branches observed, most ultra-long SNRs can still maintain bamboo-shaped and highly-regular and uniform structure. It is demonstrated that the d-DAGS method possesses the ability to grow much longer straight bamboo-shaped SNRs even though soft silicone materials are used.

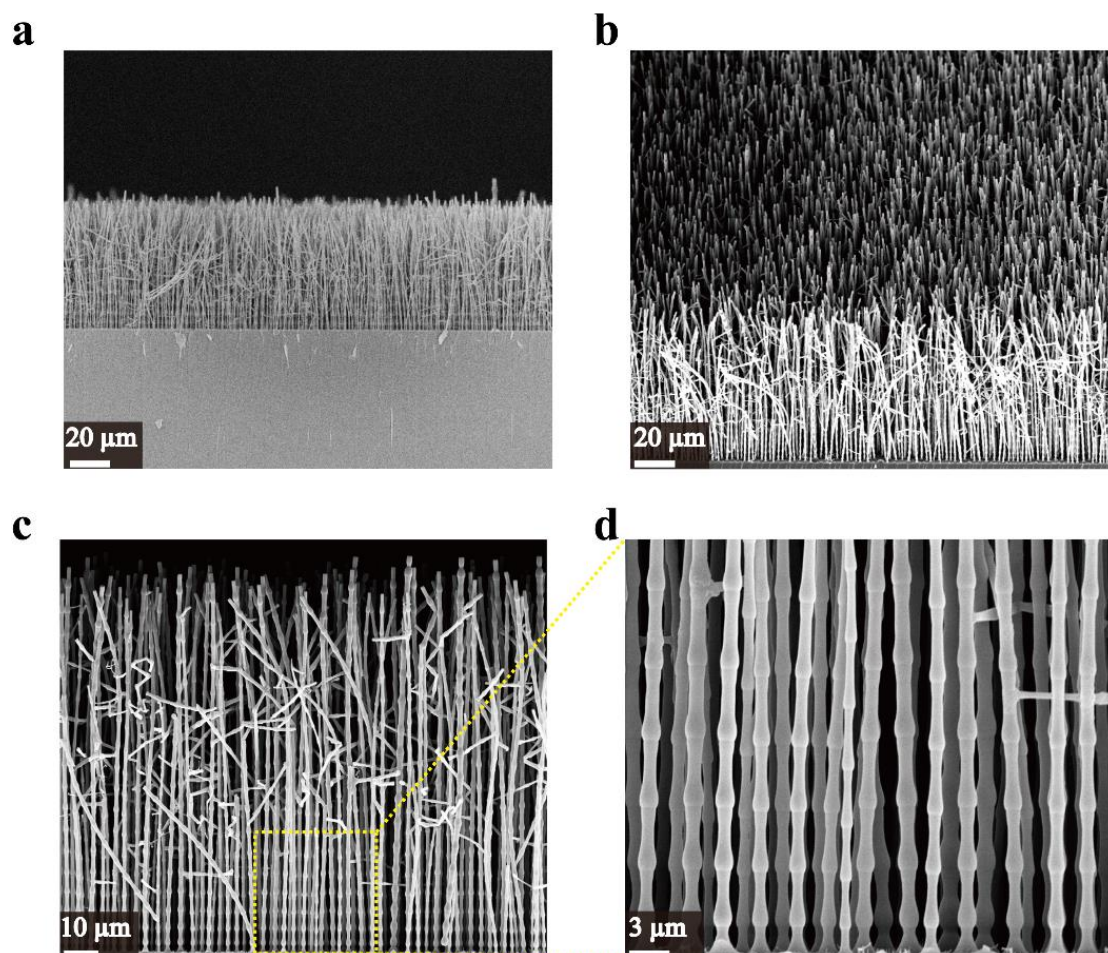


Figure 4.3.8: SEM images of ultra-long ETCS-SNRs. (a) 12-seg-ETCS-SNRs taken at a tilt angle of 90°; (b), (c), (d) 18-seg-ETCS-SNRs taken at a tilt angle of 45° and 90°, respectively. Reprinted with permission from[23].

Therefore, according to the height of the synthesized bamboo-shaped SC-SNRs, all samples can be roughly classified as:

- **Short bamboo-shaped group** ($h < 10 \mu\text{m}$): 1-seg-ETCS-SC-SNRs and 2-seg-ETCS-SC-SNRs;
- **Medium bamboo-shaped group** ($10 \mu\text{m} < h < 20 \mu\text{m}$): 3-seg-ETCS-SC-SNRs and 4-seg-ETCS-SC-SNRs;
- **Long bamboo-shaped group** ($20 \mu\text{m} < h$): 5-seg-ETCS-SC-SNRs and 6-seg-

ETCS-SC-SNRs;

- **Ultra-long bamboo-shaped group:** 12-seg-ETCS-SC-SNRs and 18-seg-ETCS-SC-SNRs.

4.3.4 Robust superhydrophobicity

The surface of glass substrates, after being coated with the bamboo-shaped SNRs, presents different anti-wetting behaviors because of the different segment numbers. As shown in **Figure 4.3.9**, θ_{WCA} varies from $\sim 128^\circ$ to be bigger than 150° , and an obvious tendency can be observed that with increasing the segment numbers in bamboo-shaped structures, θ_{WCA} progressively increases until the perfect static water contact angle ($\sim 180^\circ$) is reached with the ultra-long bamboo-shaped group. Moreover, the θ_{WSA} decreases gradually from $\sim 10^\circ$ (2-seg-ETCS-SC-SNRs) to be smaller than 1° (long and ultra-long bamboo-shaped groups). The enhanced hydrophobicity is related to the increase of thickness of the surface coating, in other words, the roughness of the solid surface because the geometrical parameters play an important role in surface wetting behavior by affecting the adhesive force of the surface structures[35].

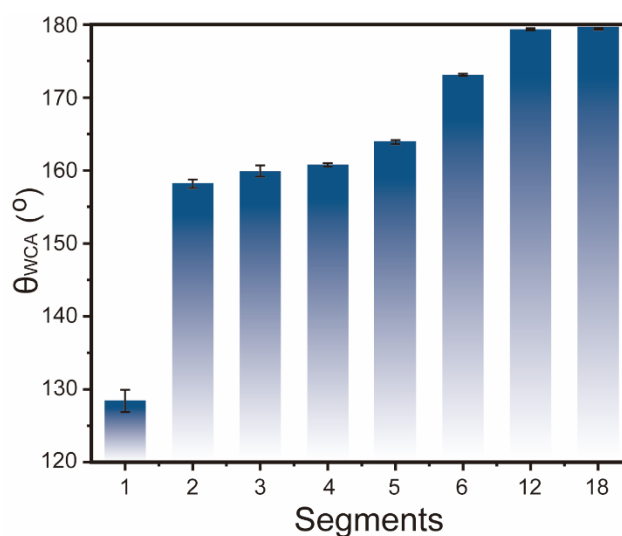


Figure 4.3.9: θ_{WCA} of the bamboo-shaped SNRs with different number of segments. Adapted with permission from[23].

In this case, the diameter of all the samples is considered constant (~ 630 nm) as the RH (60%) is fixed during the synthesis process. The bamboo-shaped SNRs with more segments are higher, and their aspect ratios are therefore bigger, for example, aspect ratios of ~ 4 and ~ 176 can be obtained from 1-seg-ETCS-SC-SNRs and 18-seg-ETCS-

SC-SNRs, respectively. The adhesive force of the bamboo-shaped SNRs with more amount of segments is vastly reduced, leading to the formation of a substantial energy barrier to prevent water droplets from wetting a deeper position[37]. As explained in Cassie's equation:

$$\cos\theta_{WCA}^C = r_f f \cos\theta_e + f - 1 \quad (4.3.1)$$

where θ_{WCA}^C is the apparent contact of the Cassie model, r_f is the ratio of the actual area to the projected area in the liquid-solid contact, f is the area fraction of the solid-liquid contact, and θ_e is the equilibrium contact angle of the liquid droplet on a flat surface.

In the Cassie-Baxter state, more air pockets are trapped in the space between a solid surface and the water droplet because of the higher structure, the air fraction is therefore increased as well as the solid fraction on the horizontal projected plane of the solid-liquid contact is reduced. Therefore, an excellent superhydrophobic solid surface is produced.

To further verify the superhydrophobicity of the bamboo-shaped SNRs decorated samples, the wetting state transitions were investigated under both static and dynamic conditions, respectively.

Wetting state transitions under static wetting conditions

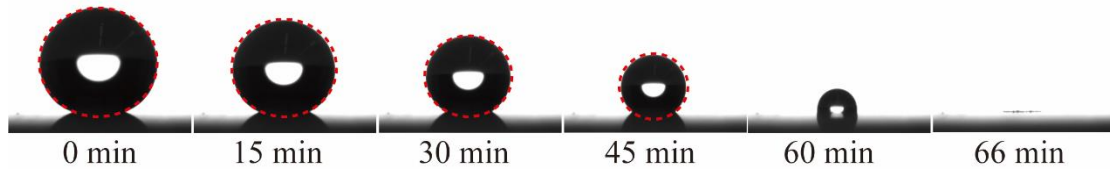


Figure 4.3.10: A static water droplet (10 μL) placed on the 6-seg-ETCS-SC-SNRs coated glass slide gradually shrank with time owing to evaporation. Adapted with permission from[23].

The θ_{WCA} of 173.5° is measured when a water droplet (10 μL) is placed on the glass substrate decorated with 6-seg-ETCS-SC-SNRs. The slow-shrinking process caused by evaporation under lab ambient temperature was recorded, as shown in **Figure 4.3.10**. Three sequential evaporation stages can be observed with decreasing volume of the water droplet[150, 151].

- In the first stage (from 0 min to 15 min), the so-called constant contact line

mode, the contact line between the water droplet and solid surface, is almost constant with a very small change $\sim 0.5\%$, whereas the θ_{WCA} quickly decreases to $\sim 154.2^\circ$.

- In the second stage (from 15 min to 39 min), the so-called constant contact angle mode, an almost constant average value of θ_{WCA} ($\sim 155.1^\circ$)¹ is maintained during the time while the contact line is changed $\sim 14\%$.
- In the third stage (from 39 min to 66 min), the so-called the mixed mode, the decrease of both contact angle and contact line occurs simultaneously.

Notably, the water droplet can maintain its spherical shape for more than 45 min and its superhydrophobicity for 39 min. In the late evaporation stage (~ 60 min), the transitions from the Cassie-Baxter state to the Wenzel state occur, resulting in a small θ_{WCA} of $\sim 99.3^\circ$. Additionally, the glass slide sample coated with 6-seg-ETCS-SC-SNRs also presents anti-wetting properties against other aqueous solutions such as rhodamine, methylene blue, milk, and cola (**Figure 4.3.11**).



Figure 4.3.11: Aqueous droplets (10 μL) of water, rhodamine, methylene blue, milk, and cola on the surface of 6-seg-ETCS-SC-SNRs modified sample. Adapted with permission from [23].

Wetting state transitions under dynamic wetting conditions

Water-impacting test, so-called “dynamic” wetting conditions, is conducted to evaluate the anti-wetting ability of the surface coating. As mentioned in section 3.6.8, all glass samples coated with n-seg-bamboo-shaped SNRs ($n = 1 - 6, 12, 18$) from different height groups were examined. A free-falling water droplet (10 μL) released from the

¹ 155° is considered the receding angle of the Cassie-Baxter state.

height of 1.5 cm above the solid surface is tracked by a high-speed camera, and the time-resolved pictures showing the water droplet at its highest re-bounced position in the first five bounces are presented in **Figure 4.3.12**.

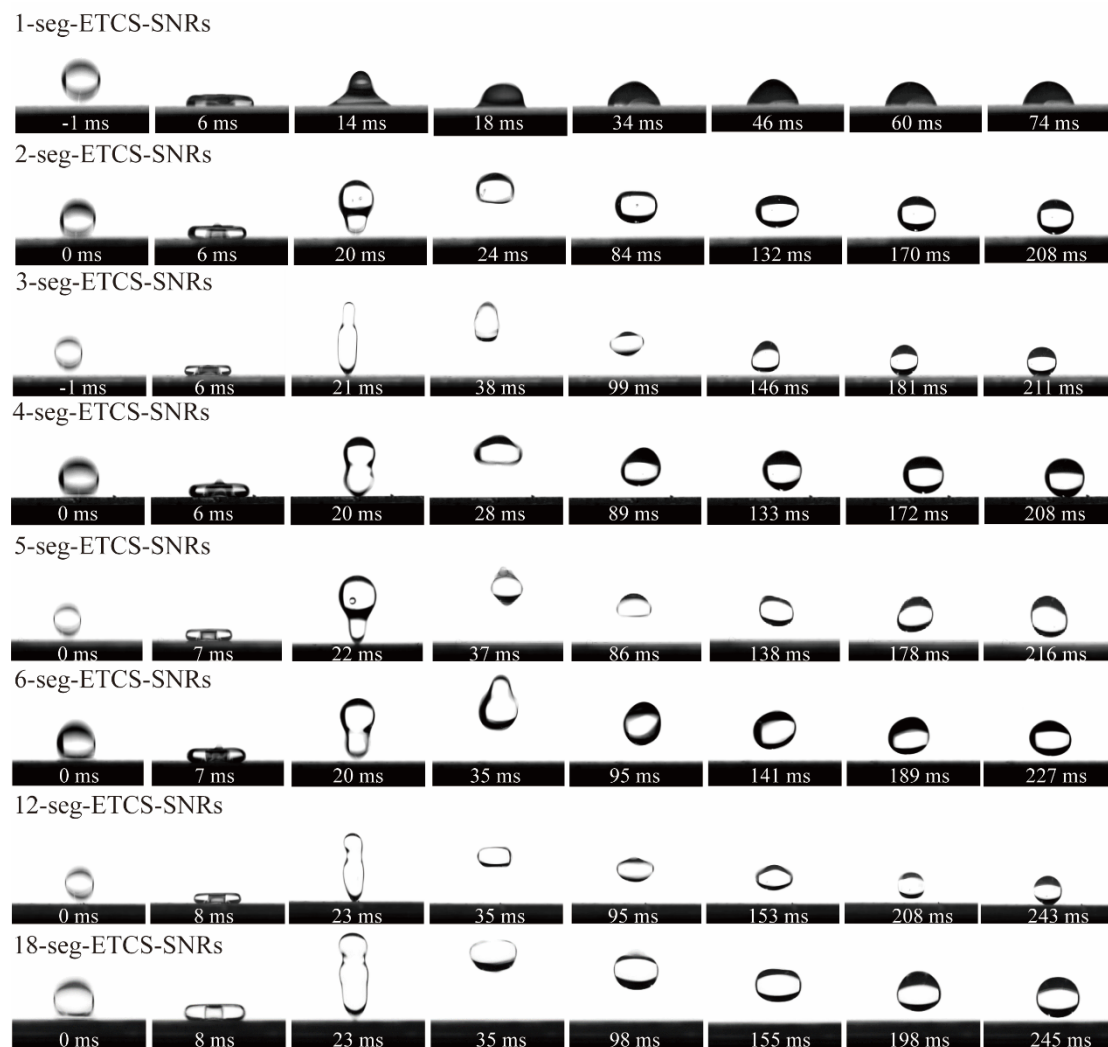


Figure 4.3.12: Time-resolved pictures showing a water droplet (10 μL) bounces on n -seg-ETCS-SC-SNRs ($n= 1 - 6, 12, 18$) coated glass substrates. $We = 9$. Adapted with permission from[23].

It is clear that the water droplet cannot re-bounce on the sample surface decorated with 1-seg-SNRs because of its weak anti-wetting ability (low θ_{WCA} , as shown in **Figure 4.3.9**). For the other superhydrophobic samples, several bounces are observed, and a higher rebounding distance can be expected from the samples coated with more segments of SNRs, which means that the height of the silicone structures or the thickness of the coatings is bigger. As shown in **Table 4.3.1**, the rebounding heights of the samples in their first bounce are summarized, and the subsequent bounces follow

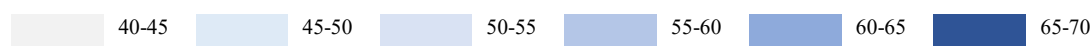
the same trend.

Table 4.3.1: Rebounding heights of the samples in their first bounce.

No. of Segments	1	2	3	4	5	6	12	18
Height (μm)	0	2.5	2.4	2.6	2.6	3.0	4.0	4.1

Table 4.3.2: Bounce periods of the samples.

No. of Segments	1	2	3	4	5	6	12	18
period 1 (ms)	-	58	58	60	58	62	65	64
period 2 (ms)	-	46	56	44	52	52	60	61
period 3 (ms)	-	42	48	44	44	46	50	47



It is observed that the higher rebounding distance is related to the longer bounce period. As summarized in **Table 4.3.2**, longer-time bounce periods are concentrated in the long and ultra-long bamboo-shaped groups. After analyzing the bounce height and period of these samples, a conclusion is obtained that the samples decorated with bamboo-shaped SNRs that have more segments are able to withstand the bigger kinetic energy of the falling water droplet and convert it into elastic potential energy. This can be further understood as the trapped air layer compressed under the water droplet impact, gaining a repelling pressure to reduce adhesion, avoid penetration, and protect the superhydrophobicity of the coated substrates[91]. The wetting state transition from Cassie-Baxter state to Wenzel state cannot occur under this dynamic condition, indicating the robust dynamic water-repelling ability of the bamboo-shaped SNRs, especially the ones with more segments.

4.3.5 Transparency of the bamboo-shaped SNRs coatings

A frosted texture can be observed from the samples coated with bamboo-shaped SNRs (**Figure 4.3.11**). As shown in **Figure 4.3.13**, the transmittance of the glass substrates before and after modifications¹ with respective SNFs and SNRs with different numbers

¹ All samples are only coated by one side.

of segments was compared in the visible range of 300 – 800 nm. Approximate 90% of the transmittance can be seen from the bare glass, whereas the value drops to ~ 80% and ~ 50% for the samples coated with SNFs (Figure 4.3.14) and 1-seg-ETCS-SNRs, respectively. For the samples coated with more than 2 segments of bamboo-shaped SNRs, around 30% of transmittance is observed with slight differences. In summary, the bamboo-shaped SNRs coatings have the potential to be used as waterproof protective shells in some practical scenarios. Future studies about their optical properties are of great significance for developing their applications in a wider range of fields.

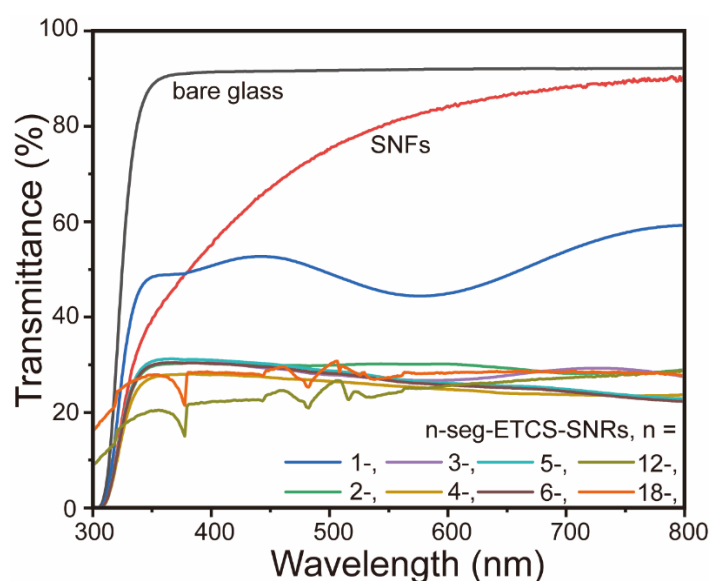


Figure 4.3.13: Transmittance of bare glass slide, SNFs, and n-seg-ETCS-SNRs ($n = 1-6, 12, 18$) coated glass slides for wavelength between 300 – 800 nm. Adapted with permission from[23].

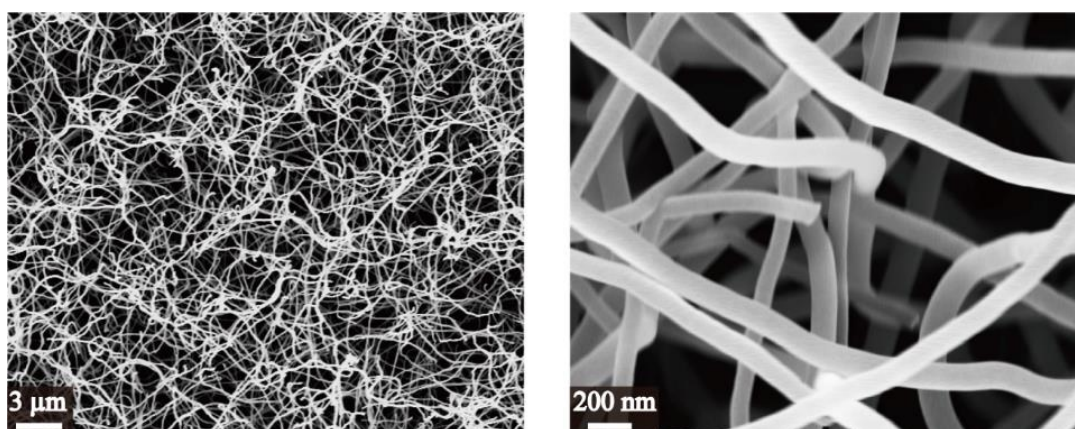


Figure 4.3.14: SEM images of the SNFs samples used as comparisons in this thesis. Reprinted with permission from[23].

4.3.6 Enhanced chemical, environmental, and mechanical durability

Chemical and environmental Durability

6-seg-ETCS-SC-SNRs coated sample is selected in the following tests. As shown in **Figure 4.3.15.a**, the θ_{WCA} of the sample is periodically measured and plotted as a function of immersion time in various corrosive solutions. It clearly shows that the polar and nonpolar organic solvents, including toluene, DMF, and EtOH, have ignorable effects on the surface wetting properties, whereas the corrosion effect of the HCl and NaOH solutions is relatively strong at pH values of 1 and 13. The samples lose their superhydrophobicity after 12 h immersion in such strong acidic and basic solutions.

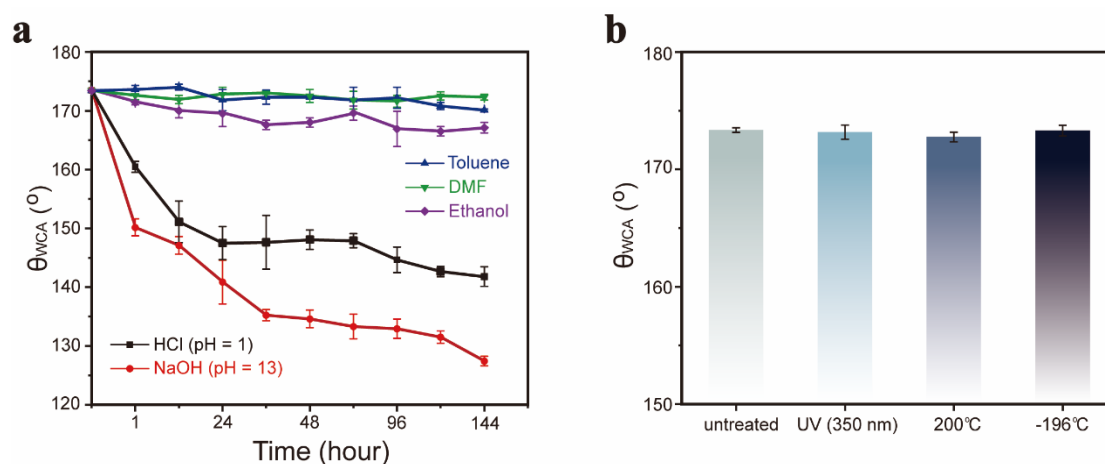


Figure 4.3.15: (a) Plot of θ_{WCA} as a function of corrosion time in HCl (0.1 M), NaOH (0.1 M), toluene, DMF, and ethanol. (b) Environmental durability tests of the sample. Adapted with permission from[23].

However, SEM images (**Figure 4.3.16**) indicate that the morphology of the samples is almost fully maintained after 144 h of immersion in different solutions, except some collapses occurred at the top segment because of the capillary force (adhesion) induced by surface tension during the drying process¹. In addition, the FT-IR spectra (**Figure 4.3.17**) of the samples before and after doing the chemical durability test are recorded, showing no obvious chemical changes resulting from the chemical corrosion. Moreover, **Figure 4.3.15.b** shows that the samples are hardly affected by some extreme environments, such as UV light (350 nm) and temperatures ranging from $-196\text{ }^{\circ}\text{C}$ to $200\text{ }^{\circ}\text{C}$ for 24 h. It is demonstrated that the bamboo-shaped SNRs coated samples have

¹ Samples were removed from solutions and dried by freeze-drying machine before doing static WCA measurements.

excellent chemical and environmental durability.

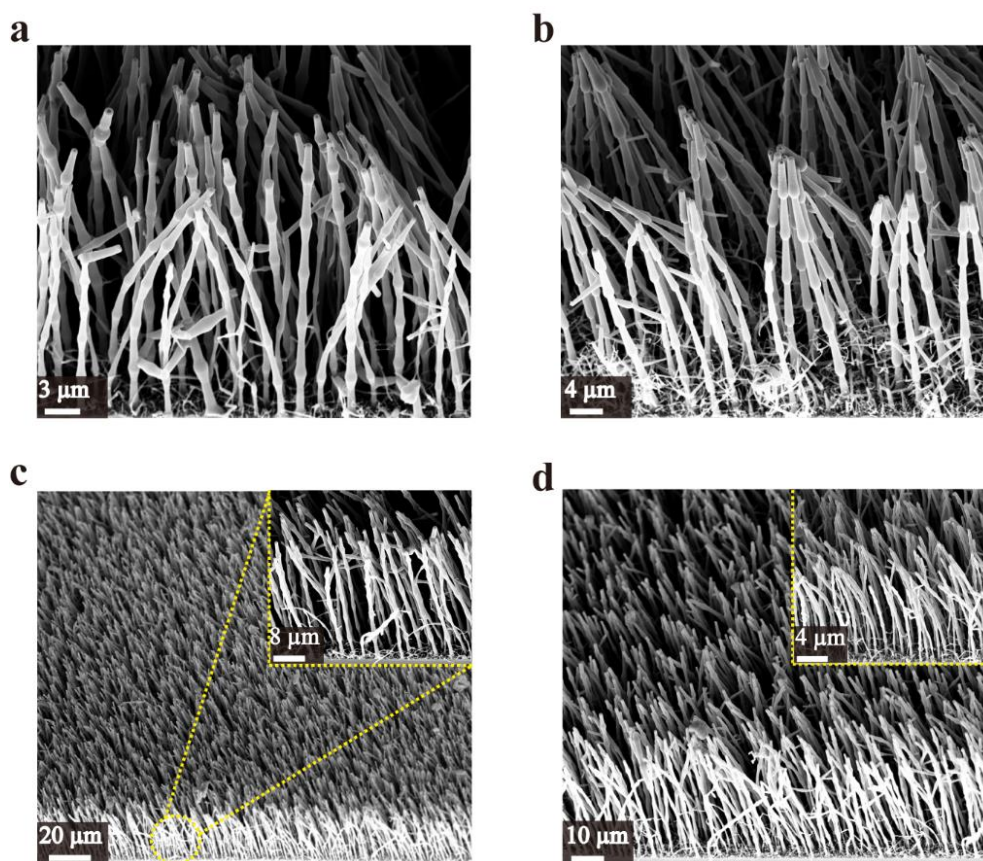


Figure 4.3.16: SEM images of the samples after chemical corrosion (144 h) from (a) HCl (0.1 M), (b) NaOH (0.1 M), (c) Toluene, and (d) Ethanol, insert is the magnified images. Reprinted with permission from [23].

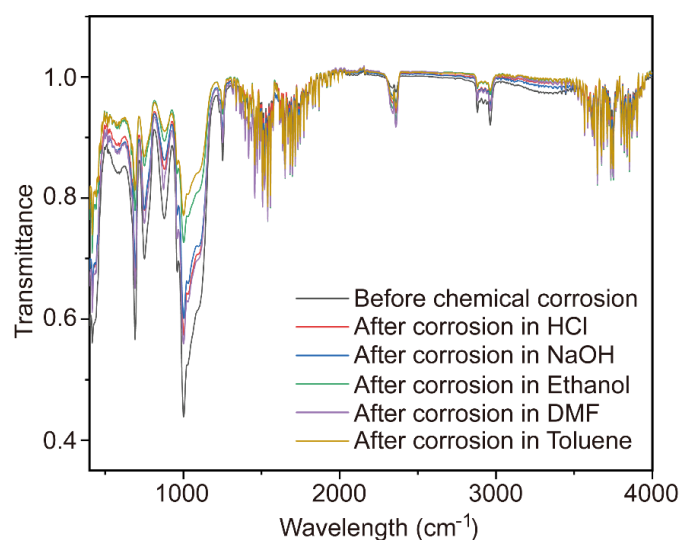


Figure 4.3.17: FT-IR spectra of the sample before and after chemical corruptions (144 h) from HCl (0.1 M), NaOH (0.1 M), toluene, ethanol and DMF, respectively. Reprinted with permission from [23].

Mechanical durability

The geometrical parameters of the superhydrophobic materials are very important in deciding their mechanical stability, which is considered to be mutually exclusive with the surface hydrophobicity because of the vulnerability of nanostructures to abrasion. Therefore, the geometrical parameters are highly concerned with designing, fabricating, and applying the surface rough micro and nanostructures[2]. As mentioned above, conventional SNFs with θ_{WCA} of $162.1^\circ \pm 1.7^\circ$ and θ_{WSA} of $8.0^\circ \pm 1^\circ$ (**Figure 4.3.14**) are used as comparison or reference control throughout this thesis. As shown in **Figure 4.3.18**, after 10 times of linear abrasion under load of pressure of 0.5 kPa, 1.5 kPa, and 2.5 kPa separately, the anti-wetting property of the SNFs sample is significantly influenced, showing a big decrease in θ_{WCA} and unmeasurable θ_{WSA} ($> 90^\circ$) especially after the tests with 1.5 kPa and 2.5 kPa loading pressures. In contrast, the sample decorated with 6-seg-ETCS-SC-SNRs is able to maintain its high θ_{WCA} ($> 160^\circ$) and its small θ_{WSA} ($< 5^\circ$) even with a slight increase. Additionally, the pictures and SEM images (**Figure 4.3.19**) demonstrate that some obvious scratches and damages show up on the SNFs sample after linear abrasion tests even under very small pressure (0.5 kPa), indicating the weak wear-resistance of the conventional SNFs structures. On the contrary, even a high loading pressure (2.5 kPa) has an ignorable effect on the 6-seg-ETCS-SC-SNRs coatings. Their hierarchical structure and morphology are well maintained, although some small scratches and collapses can be observed from the magnified SEM images (**Figure 4.3.20**).

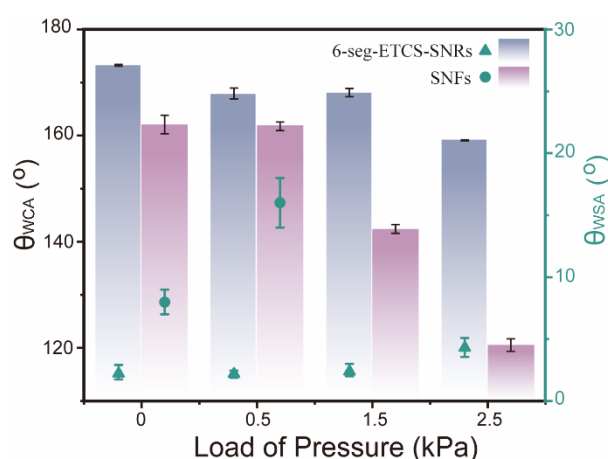


Figure 4.3.18: θ_{WCA} (left y-axis) and θ_{WSA} (right y-axis) of samples after 10 linear abrasion times under different load of pressure. Adapted with permission from[23].

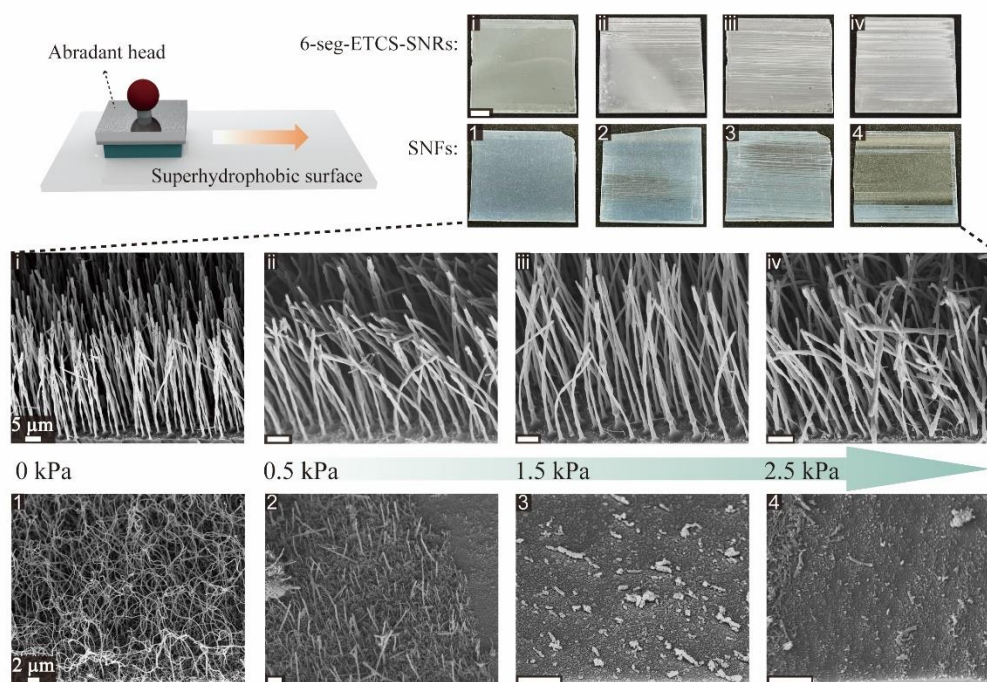


Figure 4.3.19: Scheme of the linear abrasion test (top-left) and pictures (scale bar: 50 mm) and the corresponding SEM images of glass substrates coated with 6-seg-ETCS-SC-SNRs (i - iv) and SNFs (1 - 4), respectively. Adapted with permission from[23].

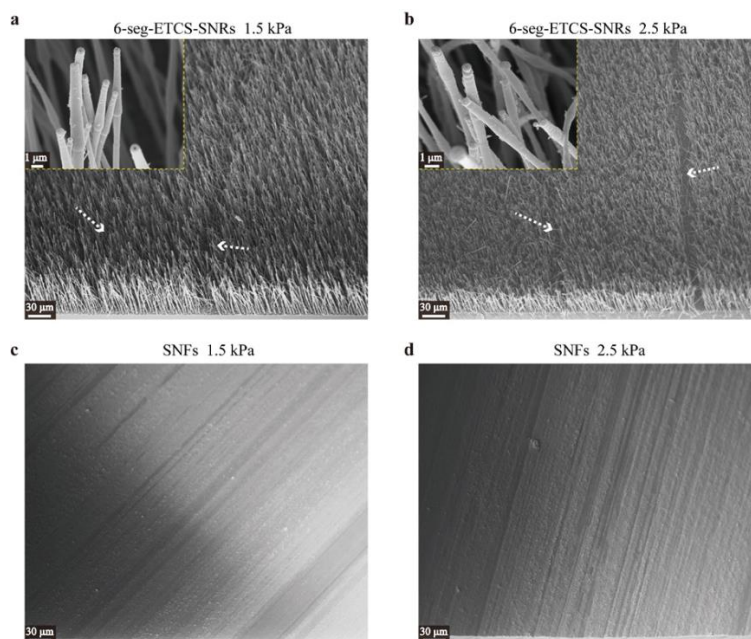


Figure 4.3.20: SEM images of (a-b) 6-seg-ETCS-SC-SNRs and (c-d) SNFs structures after mechanical linear abrasion test, insert is the magnified image of the rubbed SNRs, white arrows indicate the scratches shown on the surface. Reprinted with permission from[23].

4.3.7 Buoyancy promotion and self-cleaning

Buoyancy promotion

The main support for the floating stuff is the surface tension, which is determined by the material surface energy[152]. Therefore, decreasing the substrate surface energy to reduce the molecular attraction between water and the solid surface is considered a promising way to increase the load-bearing capacity of the floating glass substrate. As schematically illustrated in **Figure 4.3.21**, the maximum bearing weight of different samples is measured and converted into the buoyancy and buoyancy promotion (in % regarding bare glass) separately. An obvious increase tendency of both buoyancy and buoyancy promotion is observed with increasing the number of SNRs segments. As explained in section 4.3.4, a higher structure (more segments) is able to provide more space in the solid-liquid interface to trap more air plastrons in the cavities, thereby reducing the touch possibilities of water surface and substrate and further maximizing the use of water surface tension to promote the load-bearing capacity of the floating substrates. Therefore, the bamboo-shaped SNRs can be used as “armor” on devices such as floating platforms and deep-water detector to promote buoyancy, save energy, and protect the material surface in contact with water.

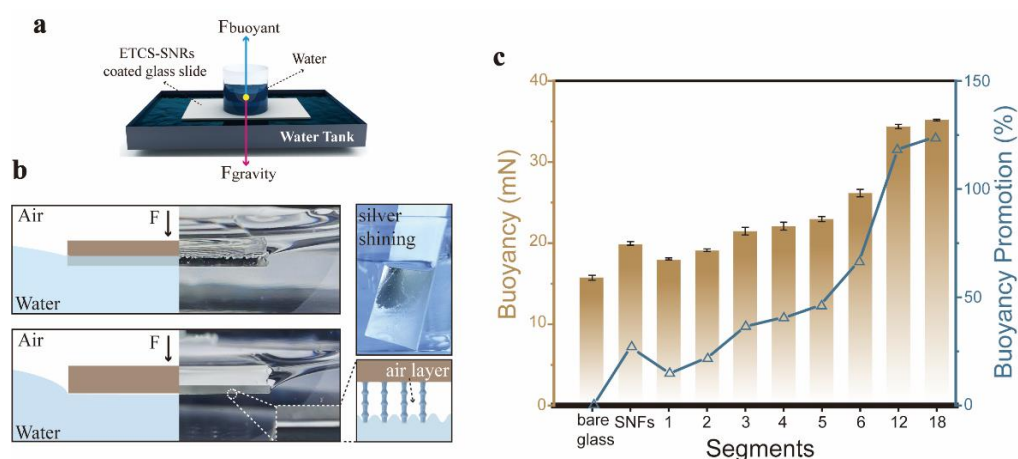


Figure 4.3.21: (a) scheme of buoyancy measurement and (b) the difference at the solid-liquid-vapor interface of a floating bare glass slide (top) and bamboo-shaped SNRs coated glass slide (bottom). (c) measurements of buoyancy (left y-axis) and buoyancy promotion as a percentage (right y-axis) of different samples. Bare glass is used as the reference. Adapted with permission from[23].

Self-cleaning

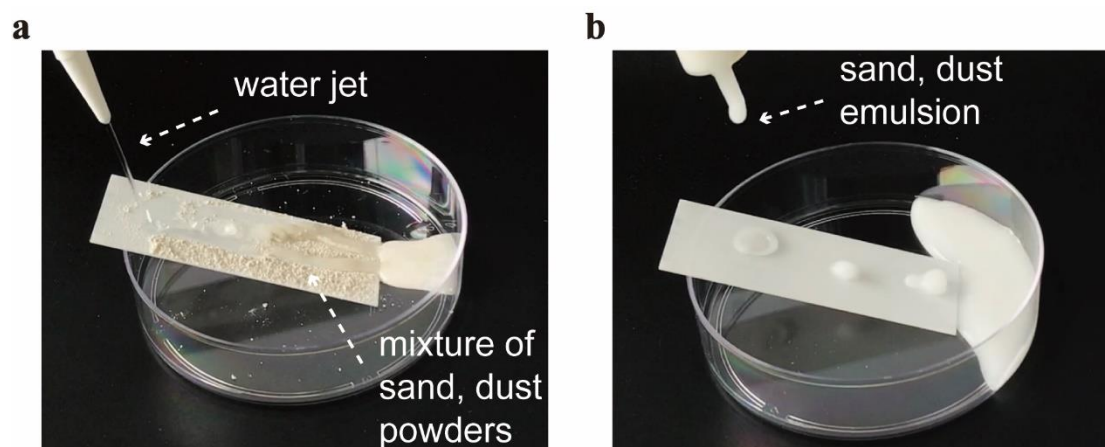


Figure 4.3.22: Self-cleaning test with (a) chalk particles (dry mixture of sand and dust) on sample surface and (b) sand and dust emulsion jet. Samples coated with 6-seg-ETCS-SC-SNRs were used. Adapted with permission from [23].

Self-cleaning tests on the samples modified by 6-seg-ETCS-SC-SNRs were performed to evaluate the ability of bamboo-shaped SNRs coatings to reduce general and bacterial contaminations (discussed in section 4.2.6) [5]. As presented in Figure 4.3.22.a, the dry mixture of small particles, for example, sand and dust, are easily taken away by rolling-off water droplets, leaving a clean and unaffected sample surface. In addition, the sample surface can remain uncontaminated even after being flushed by the emulsion jet of chalk particles (Figure 4.3.22.b), further indicating the excellent antifouling functionality of the coated samples.

4.3.8 Water-harvesting

Because of the rapid population growth, over-consumption, environmental pollution, and global climate change, the incessant water scarcity problem needs to be solved urgently [38-40, 153]. Harvesting water from fog or atmospheric humidity is considered a promising solution to it. Many materials used in water-harvesting applications either have unique structures or have special wettability-patterned surfaces, owing to the inspirations from natural cases, for example, spider silk [154-156], cactus [157], and desert beetle [158, 159]. As one of the most important practical applications of superhydrophobic/philic materials, the water-harvesting functionality, which has been rarely reported from other silicone-based micro and nanostructures, was evaluated on

the obtained bamboo-shaped SNRs coated samples with segment numbers of 1, 3, and 6. Bare glass slide and SNFs modified sample were used as comparison products.

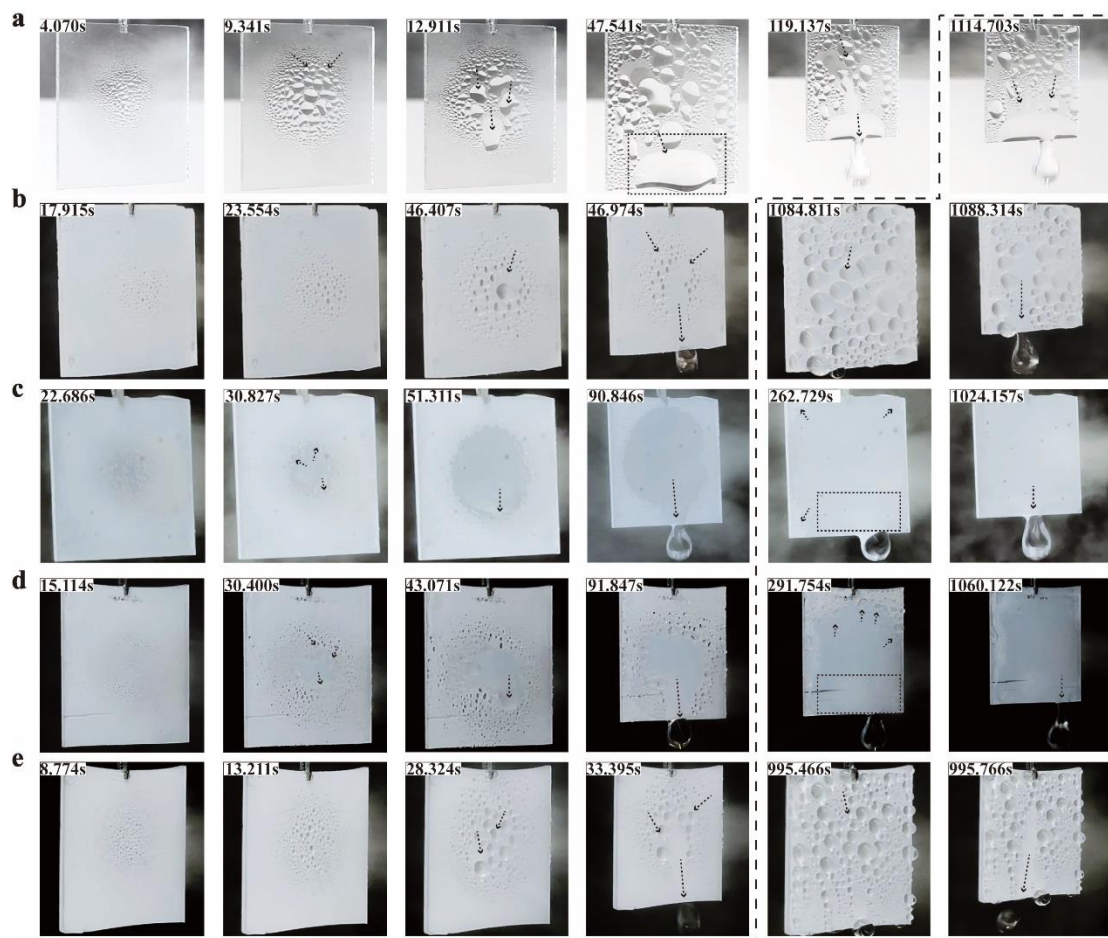


Figure 4.3.23: Water-harvesting test on different samples (size: 26 x 26 mm): (a) bare glass, (b) SNFs, (c) 1-seg-ETCS-SC-SNRs, (d) 3-seg-ETCS-SC-SNRs, and (e) 6-seg-ETCS-SC-SNRs. The dotted line separates the images captured in the early and middle stage of the process. Adapted with permission from [23].

The whole process of water-harvesting, including condensation, growth, and shedding, is presented in **Figure 4.3.23** using the first collected water droplet as an example, namely, the early stage. The middle stages¹ of the respective measurements are also shown and circled by the dotted line. Tiny water droplets are able to quickly condense on the solid surface once water vapor is ejected from the nozzle of the ultrasonic humidifier, and then coalesce to be bigger droplets and keep growing by merging with

¹ As introduced in section 3.6.6, 30 min is the minimal time used in the water-harvesting measurement. Therefore, the middle stage is around 15 min.

neighboring small water droplets, eventually resulting in the formation of large water droplets. The large water droplet cannot stay on the surface with increasing its size/weight¹. Once the critical size is reached, the large water droplet rolls off and takes all the water droplets on its rolling path away. A new round of water-harvesting process is therefore triggered due to the fresh solid surface being exposed to the condensation of other tiny water droplets. The processes of water droplet coalescence, growth, and transport have been marked in **Figure 4.3.23** by dashed arrows.

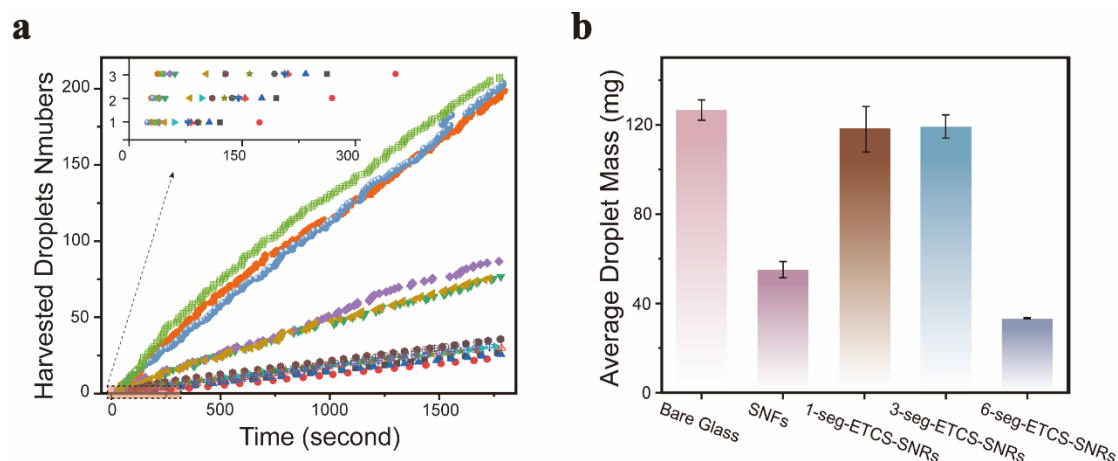


Figure 4.3.24: (a) Number of harvested water droplets as a function of time, three results were collected for each sample, *i.e.*, bare glass (■ ● ▲), SNFs (▼ ◆ ◀), 1-seg-ETCS-SC-SNRs (⊕ ⊕ ⊕), 3-seg-ETCS-SC-SNRs (▶ ⊙ ★), and 6-seg-ETCS-SC-SNRs (⊙ ⊙ ⊕). (b) Average droplet mass of the different samples. Adapted with permission from [23].

Each single water droplet was collected and analyzed to gain more information about the water collection efficiency of the solid surface. As shown in **Figure 4.3.24.a**, the harvested water droplet number as a function of collecting time is investigated based on three measurements of each sample. For the samples coated with 6-seg-ETCS-SC-SNRs, SNFs, 3-seg-ETCS-SC-SNRs, and 1-seg-ETCS-SC-SNRs, the average number of harvested water droplets are 203, 79, 31, and 31, respectively, and the average collecting time for the first water droplet are 29.66s, 42.25s, 81.67s, and 83.98s, respectively, whereas only 24 droplets and a longer collecting time 133.62s are obtained from the bare glass sample. The average droplet mass is shown in **Figure 4.3.24.b**, it is obvious that the bare glass sample, 1-seg-ETCS-SC-SNRs, and 3-seg-ETCS-SC-SNRs modified samples have similar average droplet mass, which is much bigger than the

¹ They can stay on the surface only if the balance between gravity and adhesive force is kept.

values from the samples that coated with SNFs, and 6-seg-ETCS-SC-SNRs. The above results demonstrate that the shorter time used in the nucleation \rightarrow growth \rightarrow removal process is positively correlating to the bigger number of harvested water droplets. The bigger adhesive force between the solid surface and water droplets can result in a bigger average size of water droplets collected during the process. This can also be explained by **Figure 4.3.23**, the hydrophilic bare glass sample exhibits a higher affinity for water, whereas for the samples decorated with 1-seg-ETCS-SC-SNRs and 3-seg-ETCS-SC-SNRs, due to the coating structures are linear and short ($2.7 \mu\text{m} \pm 0.2 \mu\text{m}$ and $15.5 \mu\text{m} \pm 0.4 \mu\text{m}$, respectively), tiny water droplets can easily penetrate the coating structures and wet the substrate surface, the samples can therefore lose their hydrophobic/superhydrophobic properties, and eventually show the similar water-harvesting performance with bare glass sample.

Samples coated with SNFs and 6-seg-ETCS-SC-SNRs behave similarly in the water condensation process. Even though the SNFs structures are able to prohibit penetration of tiny water droplets, the high adhesive force promotes the threshold for water droplets to roll off the sample surface, eventually leading to a relatively larger average mass and less amount of harvested water droplets.

Additionally, the space/distance between adjacent bamboo-shaped SNRs may also affect the water-harvesting efficiency by influencing the tiny water droplets penetration process. For example, the sample coated with 6-seg-ETCS-SC-SNRs has relatively small value of $2.82 \mu\text{m} \pm 0.98 \mu\text{m}$ when compared to 3-seg-ETCS-SC-SNRs and 1-seg-ETCS-SC-SNRs samples ($3.49 \mu\text{m} \pm 0.74 \mu\text{m}$ and $2.31 \mu\text{m} \pm 0.74 \mu\text{m}$ respectively), notably, the distance values between two adjacent SNRs are randomly measured from the top view SEM images (**Figure 4.3.6**). Even though the 1-seg-ETCS-SC-SNRs sample has the smallest distance value between two adjacent SNRs, it is still not as good as the 6-seg-ETCS-SC-SNRs sample in water-harvesting application because the height of the structures (thickness of the coating) is also an important parameter. 6-seg-ETCS-SC-SNRs sample presents smaller θ_{WSA} , namely, the smaller adhesive force between water droplets and solid surface, resulting in a better ability to maintain the non-wetting state and discharge very small water droplets during the water-harvesting process.

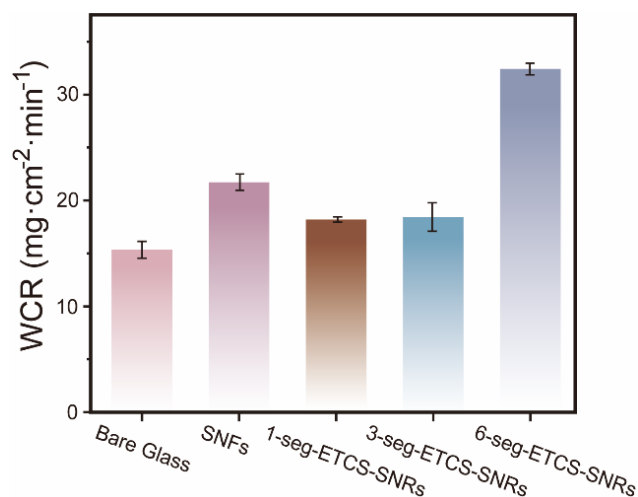


Figure 4.3.25: WCR of different samples. Adapted with permission from [23].

The WCR , which represents the average weight of water collected in a particular area over a fixed period, is normally used to evaluate the water-harvesting efficiency of the materials. As shown in **Figure 4.3.25**, the maximum WCR achieved from the tested samples is $32.3 \pm 0.6 \text{ mg}\cdot\text{cm}^{-2}\cdot\text{min}^{-1}$ for 6-seg-ETCS-SCSNRs, which is around 2.11, 1.49, 1.78, and 1.76 times bigger than the samples of bare glass, SNFs, 1-seg-ETCS-SC-SNRs, and 3-seg-ETCS-SC-SNRs, respectively. This is a very high value even compared with other related studies, as shown in **Table 4.3.3**. It is demonstrated that the superhydrophobic surface featured with specially designed bamboo-shaped SNRs, owing to their excellent performance in fast vapor deposition, high-speed growth, and the quick removal of droplets [160], is very useful in the field of water-harvesting to solve water scarcity problems realistically.

Table 4.3.3: Literature comparisons. Adapted with permission from [23].

Substrate	Structure/Method	Wettability	Distance ¹ (mm)	Tem. (°C)	RH (%)	Fog Flow/velocity (mL·min ⁻¹)	WCR ² (mg·cm ⁻² ·min ⁻¹)	Reference
glass	bamboo-shaped 6-seg-ETCS-SNRs; d-DAGS method	superhydrophobic	50	20.0 ± 0.2	~ 90	4.7	32.3 ± 0.6	this work
glass	Silicone nanofiber made from methyltrialkoxysilane; cooler used on sample	Perfectly hydrophobic	-	20 - 35	60 - 90	Humidity chamber	0.5 – 5.3	[4]
glass	Laser-induced backward transfer	superhydrophilic/superhydrophobic patterned	50	20 ± 1	80 ± 5	3	15.68	[159]
Poly(methylmethacrylate) (PMMA)	micro-nano hierarchical PMMA surface; Plasma deposition	superhydrophobic	-	20	100	0.42	19.5	[161]
Copper foils	nano-needles and micro-flowers covered surface; alkaline oxidation etching and low surface energy treatment	hydrophilic/superhydrophobic patterned	70	25	80	15 cm·s ⁻¹	5.5 ± 0.2	[162]
Titanium sheets	Hierarchical Micro/Nanostructures; Femtosecond Laser and Hydrothermal	hydrophobic layer with hydrophilic sites	100	25	28	5.2	9.06	[153]
Copper sheets	P25 TiO ₂ nanoparticles and candle soot mixed with polydimethylsiloxane; spray-coating	superhydrophilic/superhydrophobic patterned	70	25	80	15 cm·s ⁻¹	14.9 ± 0.2	[163]
Copper mesh	Liquid modification	Hydrophobic/hydrophilic patterns and Janus asymmetric wettability	20	18	90	4.2	36.7	[164]
silicon wafers	Arrays/Plasma etching, machine-drilled with regular square array	hydrophilic-hydrophobic patterned surface	-	-	-	11000 (N ₂)	~ 28 (maximum)	[165]
silicon wafers	micropatterned surfaces/ dewetting thin polymer films (spin coating)	hydrophilic bumps on a hydrophobic background	-	0	80 – 85	9800	~ 5.7	[166]

¹ Distance between the sample surface and outlet of the fog flow.² WCR is not used as a criterion for comparing the water-harvesting capabilities of different materials due to the reported water-collection experiments are conducted under different conditions.

4.4 Synthesis and functionalization of the MCH silicone nanostructures

Some parts of this chapter have been submitted for publication: Heterogeneous Silicone Nanorods with Region-Specific Functionality, and some parts of this chapter are involved in the manuscript under preparation: Mushroom-Shaped Silicone Nanostructure as a Functional Coating in Anti-Adhesive Application.

The d-DAGS method paves the way to design and synthesize versatile silicone micro and nanostructures with unique shapes and chemical compositions. Previous chapters have systematically investigated the synthetic parameters, shape-controllable growth, and practical applications of different silicone-based structures, including SNFs, short SNRs, and bamboo-shaped SNRs. Even though the obtained products have exhibited enhanced physicochemical properties in the subjects of surface and material sciences, they are still limited in realistic applications in a wide range of fields due to the lack of the feature to be simply and controllably modified on demand. Therefore, in this chapter, based on the d-DAGS mechanism, a novel type of MCH silicone nanostructures is designed and synthesized to achieve tunable region-selective functionalization. Several methods are employed to verify the success of the functionalization and the region-selective distribution. Moreover, surface and interface wetting property has been investigated and, visually revealed by using confocal microscopy. A novel hypothesis with respect to the CVD method is developed to explain the formation of unique mushroom-shape (SMHs) when the DCMVS precursor is introduced. The potential anti-adhesive application of this new type of functional coating is subsequently studied.

4.4.1 Synthesis of the MCH structures

As explained by the d-DAGS mechanism, each single segment of the bamboo-shaped SNRs is independent[23]. During the growth process, both unreacted precursors and intermediates that have not been absorbed by the condensed water droplet located at the top of formed structures are ideally assumed to be completely swept out of the reaction chamber because of the re-purging of N₂ gas flow. Notably, the volume of the reaction chamber is 6 L, whereas the flow rate of N₂ gas is ~ 2.5 L·min⁻¹, and the minimum re-purging time is 5 min. Therefore, the precursor used in the subsequent injections can be either the same or different from the first-time injected precursor, for example, as

mentioned in section 4.3, the use of the same precursor ETCS in synthesizing each single silicone segment results in the formation of highly regular and shape-controllable bamboo-shaped SNRs. However, the ETCS-SC-SNRs can only be modified by some conventional methods, such as UV[21, 167], oxygen plasma[168, 169], and water plasma[77], without any selectivity. The term selectivity indicates that the fabricated micro and nanostructures are homogenous in chemical compositions, so they cannot be precisely and partially tuned via chemical methods. Further regulating the chemical property of the silicone structures by introducing new precursors to adapt them in more complex application scenarios is therefore developed and discussed in this section.

ETCS-VTCS MCH structures

VTCS is the first-time used in synthesizing the new type of MCH structures because it has many similar physical and chemical properties with ETCS, such as MW ($161.48 \text{ g}\cdot\text{mol}^{-1}$ to $163.50 \text{ g}\cdot\text{mol}^{-1}$), vapor density (5.61 to 5.60, relative to air), and chemical structures (both are **tri**-chloro-functional-silane). Synthetic parameters for the normal VTCS-based SNRs have been analyzed in section 4.1.2, demonstrating that a flexible adjustment to the reaction conditions (as mentioned in section 3.4.1 and 4.1.2, conditions of *RT* (5 min - 10 min), *VOL* (250 μL - 300 μL), and *RH* (50% - 55%)) are used in fabricating VTCS-based SNRs) is required during the synthesis of different types of VTCS-based MCH structures.

The detailed growth process is presented in **Figure 4.4.1**, all MCH structures presented in this thesis are started with the same base ETCS segment. After re-purging the reaction chamber for a certain time with appropriate *RH* and re-injecting a certain amount of precursor for a certain *RT*, both 2-seg-ETCS-SC-SNRs and 2-seg-EV-MCH-SNRs are synthesized according to different precursors used in the second injection (**Figure 3.3.2: S7 – S5**). 3-seg structures are obtained by repeating one more time re-purging and re-injection operation (**R₂**) under specific conditions based on the 2-seg structures. According to the order/arrangement of the independent ETCS/VTCS segments, 3-seg-EEV-MCH-SNRs, and 3-seg-EVE-MCH-SNRs are eventually synthesized.

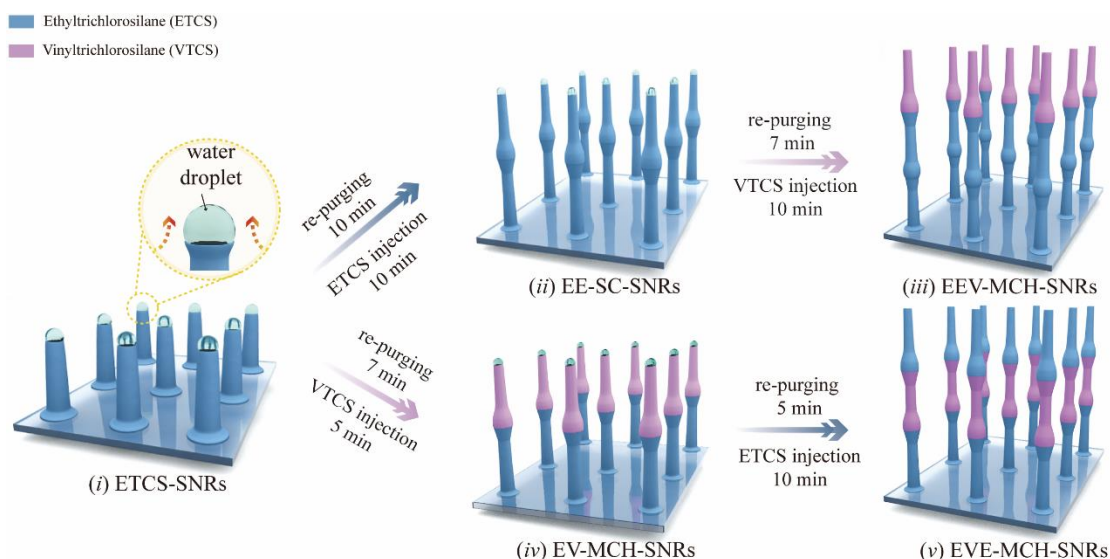


Figure 4.4.1: Schematic illustration of the synthesis of the bamboo-shaped MCH structures including EV-MCH-SNRs, EEV-MCH-SNRs, and EVE-MCH-SNRs.

ETCS-DCMVS MCH structure (SMHs)

The new type of mushroom-shaped (SMHs) structure is obtained by introducing the precursor DCMVS (MW: $141.07 \text{ g}\cdot\text{mol}^{-1}$) on the ETCS base segment. DCMVS is a kind of VTCS-containing chlorosilane whose one chlorine is replaced by the methyl group. Compared to the **tri**-chloro-functional-silanes (ETCS and VTCS), which are commonly used in synthesizing the structures such as filaments, rods, and bamboo-shaped rods, the **di**-chloro-functional-silane DCMVS is the first time used as a precursor in fabricating silicone micro and nanostructures via d-DAGS method (**Figure 4.4.2**).

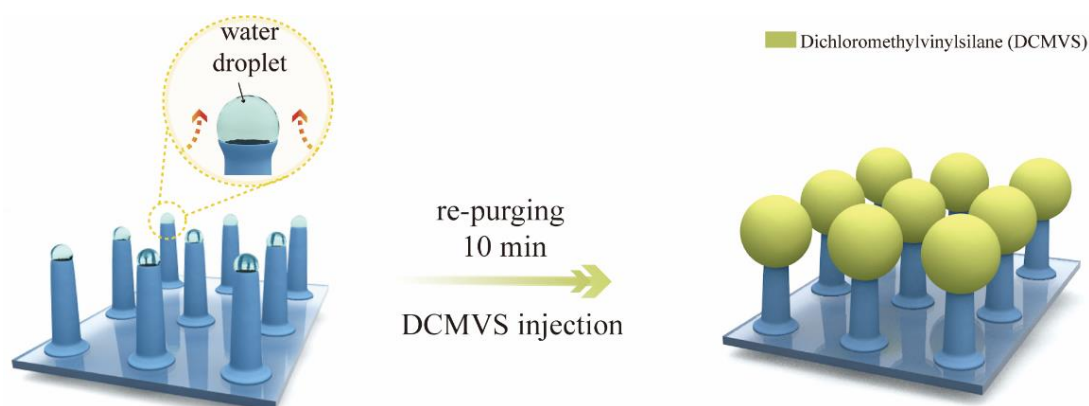


Figure 4.4.2: Schematic illustration of the synthesis of the MCH-SMHs.

The growing process of the DCMVS segment is obviously different from the normal

structures, including filaments and rods, because the cavity on the top of the normal structures (location of the condensed water droplet) is very clear after the reaction and deposition process ceased (**Figure 4.3.3**), especially after the structure being re-purged (**Figure 4.3.2**). However, as shown in the yellow box in **Figure 4.4.3.a**, it is obvious that the cavity on the top is quickly closed after the injection of DCMVS precursor ($RT \sim 1$ min).

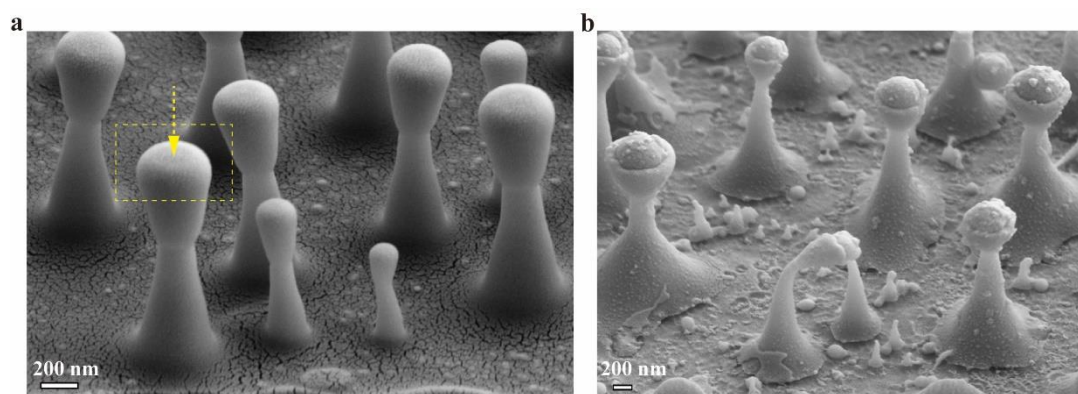


Figure 4.4.3: SEM image of SMHs showing that (a) the closed cavity after injection of DCMVS for RT of 1 min and (b) chemical etching with NaOH for 7 days on normal MCH-SMHs sample (RT : 16h).

In addition, the SEM image of the MCH-SMHs sample after being chemically etched with NaOH for 7 days (**Figure 4.4.3.b**) shows that the DCMVS layer is partially removed from the structure because of the etching-caused damage[12], indicating that the solid sphere on the top is synthesized layer-by-layer.

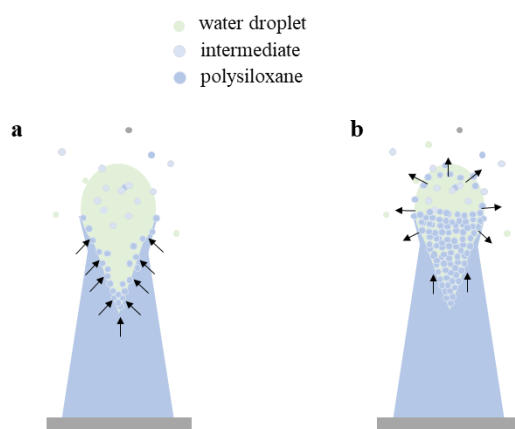


Figure 4.4.4: Schematic illustration of (a) deposition process of the ETCS/VTCS-based silicone structures and (b) possible deposition process of the DCMVS-based silicone structure. Arrows indicate the growing direction of the formed polysiloxane.

Some explanations to growth process

Therefore, A hypothesis concerning the CVD method is developed to explain the formation of the top-sphere segment.

First of all, to our knowledge, the chemical structures of the formed silsesquioxanes, which are subspecies of polysiloxanes, with **tri**-chloro-functional-silanes (ETCS and VTCS) as monomers are possible to be from random disordered structures to the extended ladder-like structures and to the ordered cage-like structures as mentioned in Chapter 2[55]. All of these structures, $[\text{CH}_3\text{CH}_2\text{SiO}_x(\text{OH})_{3-2x}]_n$, $[\text{CH}_2\text{CHSiO}_x(\text{OH})_{3-2x}]_n$, and the mixed copolymer structure, $[(\text{CH}_3\text{CH}_2\text{SiO}_x(\text{OH})_{3-2x})_k(\text{CH}_2\text{CHSiO}_y(\text{OH})_{3-2y})_l]_m$, where $0 < x < 3/2$, $0 < y < 3/2$, are able to expand in 3D space because of their tri-chloro feature ($3x$ siloxane bonds). Even though the molecular weights of the formed silsesquioxanes can hardly be determined due to their 3D nature[55], it can be derived that large molecules deposit and accumulate at the solid-liquid interface (deposited structure-water interface), further resulting in the “tip-growth” of the silicone structure with an inverted triangular conical cavity at the top[23] as illustrated in **Figure 4.4.4.a**.

On the contrary, **di**-chloro-functional-silane DCMVS can only be applied in linear polymerization, $[\text{CH}_3\text{CH}_2(\text{CH}_3)\text{SiO}_x(\text{OH})_{2-2x}]_n$, where $0 < x < 1$, and the chemical structure of the final product is therefore constrained. As shown in **Figure 4.4.4.b**, relatively light molecular weights of the final products because of the inherent connection of two functional groups (methyl and vinyl) on silicon atom, and the lack of 3D spatial structures collectively lead to the situation that the condensation of intermediates (silanol and siloxanol species) and the deposition of polysiloxanes firstly occur inside the condensed water droplet to fill the entire droplet, and the top-sphere-segment continues to be expanded layer by layer via continuous deposition of polysiloxanes that formed in surrounding suspended tiny water droplets. The whole process is self-organized.

4.4.2 Microscopic characterizations of the MCH structures

SEM images of the synthesized MCH-SNRs are shown in **Figure 4.4.5.a** indicate their highly uniform and well-arranged bamboo-shaped structures. The features of the bamboo-shaped MCH-SNRs include that they are able to keep upright, each single segment can be distinguished, and the “bamboo-knot” caused by the replenishment of

water droplets in the re-purging process can be clearly observed. These features indicate the controllability of the segment number as well as the type of segments.

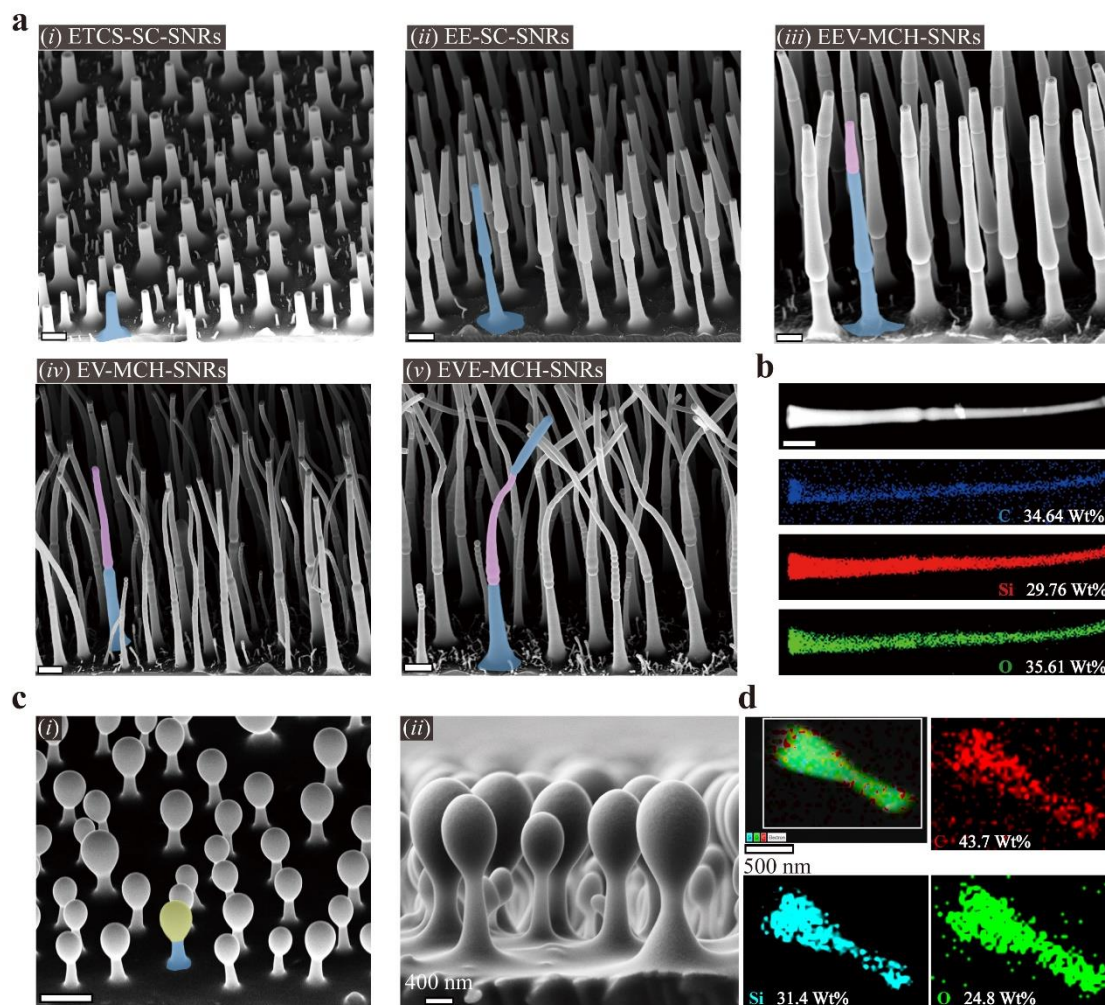


Figure 4.4.5: (a) SEM images of the bamboo-shaped MCH-SNRs. (b) STEM-EDX images of the EV-MCH-SNRs. (c) SEM images of SMHs with tilt angle of (i) 45° and (ii) 90°. (d) STEM-EDX images of the SMHs sample. Manually colored areas (segments) indicate the corresponding precursors applied with blue: ETCS, pink: VTCS, and yellow: DCMVS. Unlabeled scale bar, 1 μm .

STEM-EDX images shown in **Figure 4.4.5.b** indicate the distribution of the constituent elements of the EV-MCH-SNRs sample. Due to the chemical compositions of the precursors applied (ETCS: $\text{C}_2\text{H}_5\text{Cl}_3\text{Si}$; VTCS: $\text{C}_2\text{H}_3\text{Cl}_3\text{Si}$), it is obvious that the main elements C, Si, and O are uniformly distributed among the structures. Distinguishment between ETCS and VTCS-based segments can hardly be achieved through this method.

SEM images of SMHs, as shown in **Figure 4.4.5.c** in the respective tilt angles of 45°

and 90° demonstrate their distinct mushroom-shaped structure consisting of a spherical top segment and a normal short base SNRs. Corresponding STEM-EDX images (Figure 4.4.5.d) show similar results with the bamboo-shaped structures, DCMVS ($C_3H_6Cl_2Si$) based segment is also hardly recognized because of the uniform distribution of the C, Si, and O elements on the whole structure.

4.4.3 Geometrical parameters

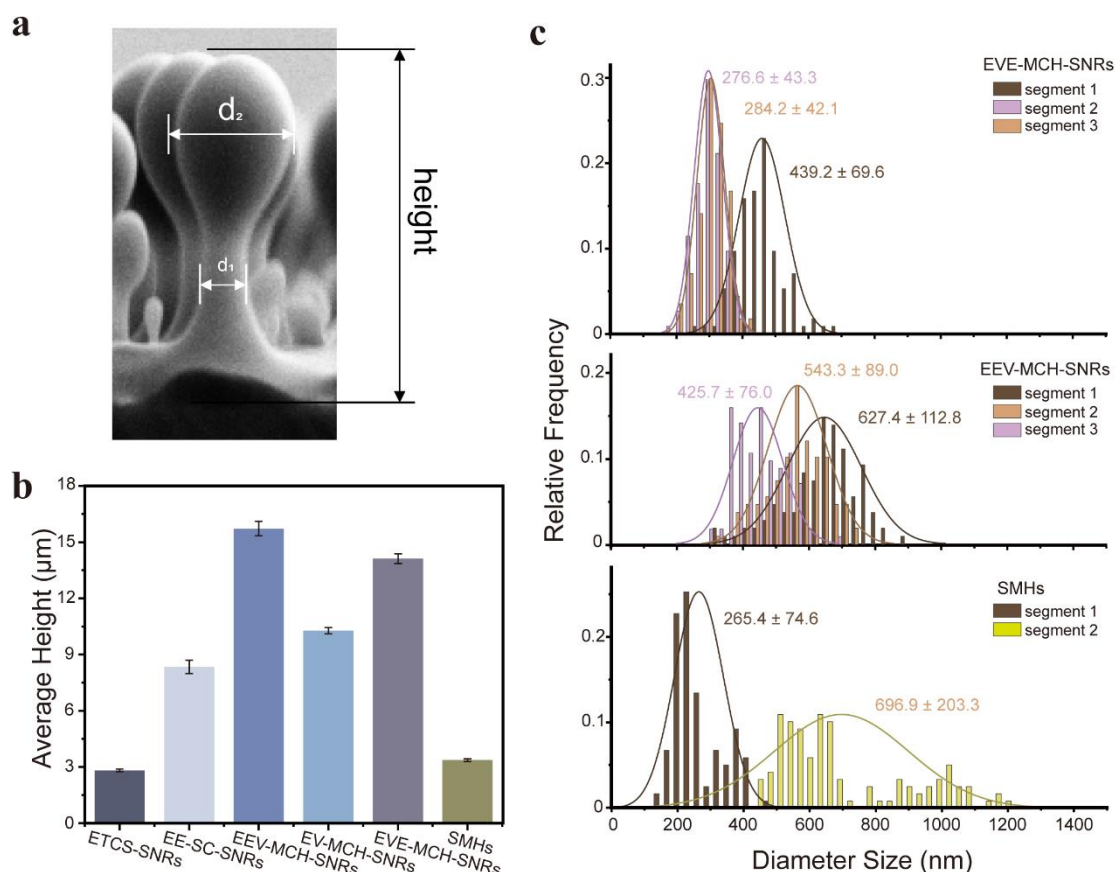


Figure 4.4.6: (a) Scheme image illustrating the measurement of height and diameter of the structures. (b) Average height and (c) Histogram of the diameter distribution with normal distribution curve, mean value, and S.D. and for EVE-MCH-SNRs, EEV-MCH-SNRs, and SMHs samples.

Geometrical parameters of the as-prepared MCH structures were measured as illustrated in Figure 4.4.6.a. Heights of the structures are obtained from the SEM images taken at the tilt angle of 90°, average values are shown in Figure 4.4.6.b. It is obvious that the structures are getting higher with the increasing number of segments except for the SMHs sample, which has a unique growth pattern: expansive growth rather than upward growth (DCMVS-based segment).

Due to the special morphologies of the MCH structures, i.e., bamboo-shaped and mushroom-shaped, their diameters are measured specific to each single segment, namely, the diameter of each segment at their half-height position (**Figure 4.4.6.a**). At least 100 measurements were conducted. The results were presented as the histogram of the diameter distributions (**Figure 4.4.6.c**), which perfectly match the dynamic adjustments of the reaction conditions during the synthesis process:

- For $E_1E_2V_3$ -MCH-SNRs, the decreasing diameter sizes from the bottom to up segments are observed, which result from the change of RH values, from 60% (E_1) to 55% (E_2) to 50% (V_3), during the purging and re-purging process. The replenishment of the water droplet located at the top cavity is controlled in this way, and the growth of the correspondent segment (diameter) is, therefore, affected by the volume of the water droplet.
- For $E_1V_2E_3$ -MCH-SNRs, even though the RH is maintained constant for the whole synthesis process, dynamic adjustments on the RT and the re-purging time have also influenced the replenishment of water droplet, resulting in the smaller diameter of the VTCS segment than the base/top ETCS segment.

SMHs samples are slightly different from the bamboo-shaped MCH samples in geometrical characterization because all SMHs samples were synthesized in an independent reaction chamber to avoid undesirable contaminations by other different types of precursors. A significant difference in diameter size can be observed between the DCMVS segment and the ETCS segment (**Figure 4.4.6.c**), which is caused by the unique growth pattern when using the DCMVS precursor, as explained above. In the meantime, the mushroom-shape of the ETCS-SCMVS MCH structures is verified by this measurement.

4.4.4 Preliminary proof of the MCH property

In order to prove the MCH property of the as-prepared samples, FT-IR spectroscopy is applied. Surface coatings of the selected samples, including ETCS-SC-SNRs, VTCS-SC-SNRs, and EV-MCH-SNRs, were scratched off the glass substrates before the test to ensure a high-quality spectrum.

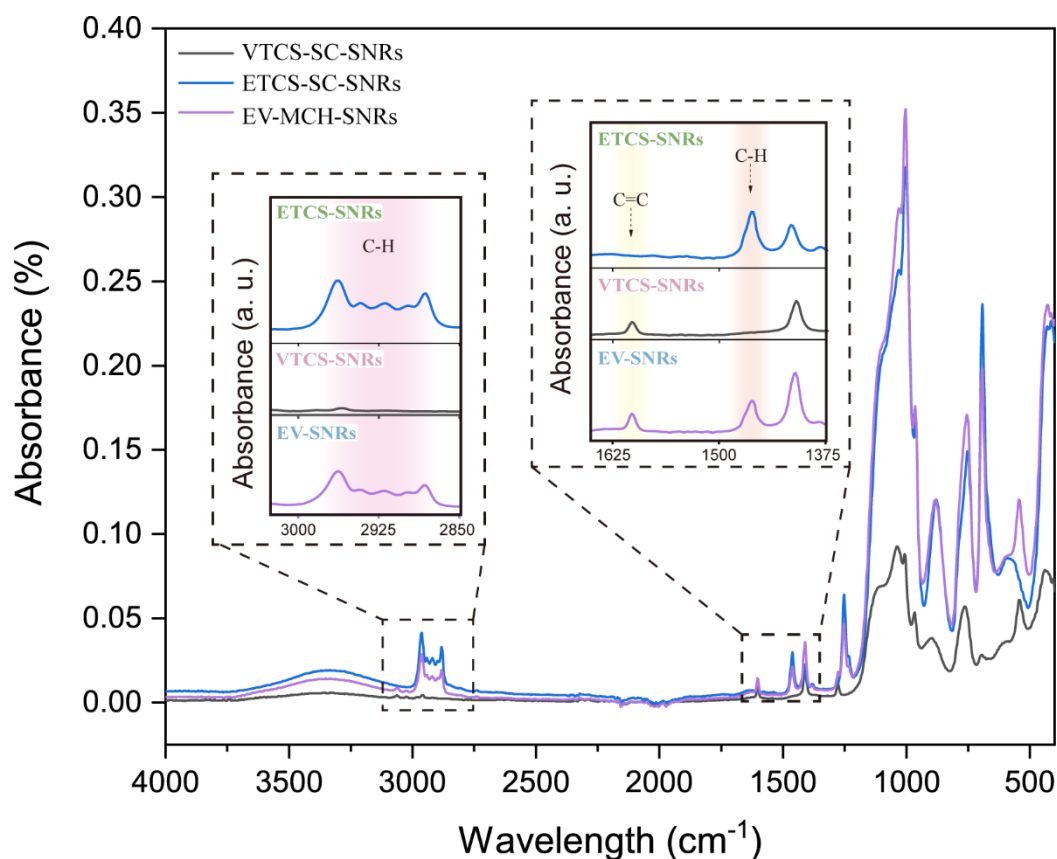


Figure 4.4.7: FT-IR spectrum of the ETCS-SC-SNRs, VTCS-SC-SNRs, and EV-MCH-SNRs samples.

As shown in **Figure 4.4.7**, the respective peaks of C-H bend and stretch at ca. 1460 cm^{-1} and ca. 2960 cm^{-1} [170] are shown only in ETCS-SC-SNRs and EV-MCH-SNRs samples, whereas the peak of C=C stretch at around ca. 1600 cm^{-1} [171] can only be observed from the VTCS-SC-SNRs and EV-MCH-SNRs samples. The results demonstrate that the EV-MCH-SNRs sample has characteristics from the ETCS-SC-SNRs and VTCS-SC-SNRs samples, respectively, which is able to preliminarily verify the MCH property of the newly synthesized structures using two different precursors.

4.4.5 The RSF mechanism

As mentioned in Chapter 2, the functional groups are able to rotate toward the polymer surface due to the flexible siloxane backbones (Si-O-Si)[172]. Compared to the inert alkyl groups such as methyl and ethyl groups, the vinyl group, which is reactive, provides the opportunity to be functionalized via photoinitiated radical-based thiol-ene click reaction, leading to the modifications of the chemical properties at the surface and interface of the materials[110, 114, 138, 173].

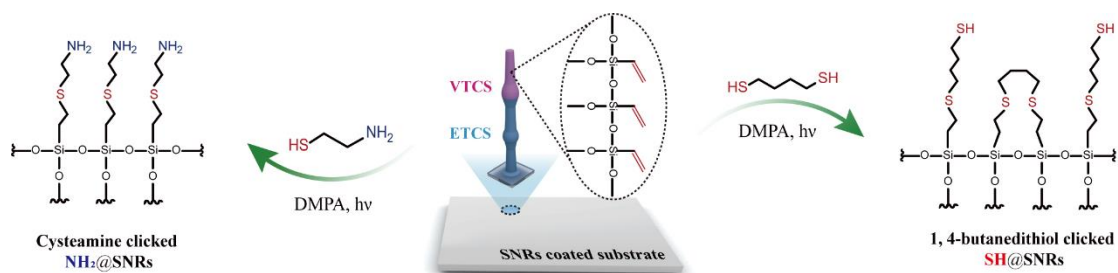


Figure 4.4.8: Scheme of the chemical modifications on EV-MCH-SNRs (as an example) via thiol-ene click reactions with reactants of cysteamine ($\text{NH}_2@$) and 1,4-butanedithiol ($\text{SH}@$), respectively.

As illustrated in **Figure 4.4.8**, the exposed vinyl groups on the surface of the VTCS-based segment are reacting with different thiol derivatives such as cysteamine and 1,4-butanedithiol with the help of a kind of cleavage photoinitiator, DMPA, under the UV condition with λ of 250 nm. Notably, DMPA plays an important role in producing highly reactive thiyl free radical ($\text{RS}\cdot$)[117], which enables to attack vinyl groups, thereby loading terminal groups such as $-\text{NH}_2$ and $-\text{SH}$ to the specific areas on-demand.

Because of the controllable growing sequence of the individual segment of bamboo-shaped nanostructures, the position of the modifiable VTCS segment can be customized, e.g., top segment: EEV-MCH-SNRs and middle segment: EVE-MCH-SNRs. The chemical functionalization can be selectively applied to the specific regions composed of VTCS-based structures on the bamboo-shaped MCH-SNRs, resulting in the tunable modification of the silicone surface properties at the micro and nanoscale. Therefore, this is defined as the region-selective functionalization.

The chemical functionalization on MCH-SNRs samples via thiol-ene click reactions with reactants of cysteamine and 1,4-butanedithiol are named $\text{NH}_2@$ and $\text{SH}@$, respectively. The MCH-SNRs samples modified by 1,4-butanedithiol offer side evidence that some other thiol derivatives can also be used in region-selective functionalization in the future to meet the various needs of different fields.

4.4.6 Proof of the RSF and the MCH property

Different techniques were applied to prove the successful functionalization of the specific region (VTCS segment) of the MCH-SNRs. Indeed, the proof of the RSF can also verify the MCH property of the as-prepared samples, so-called mutual corroboration.

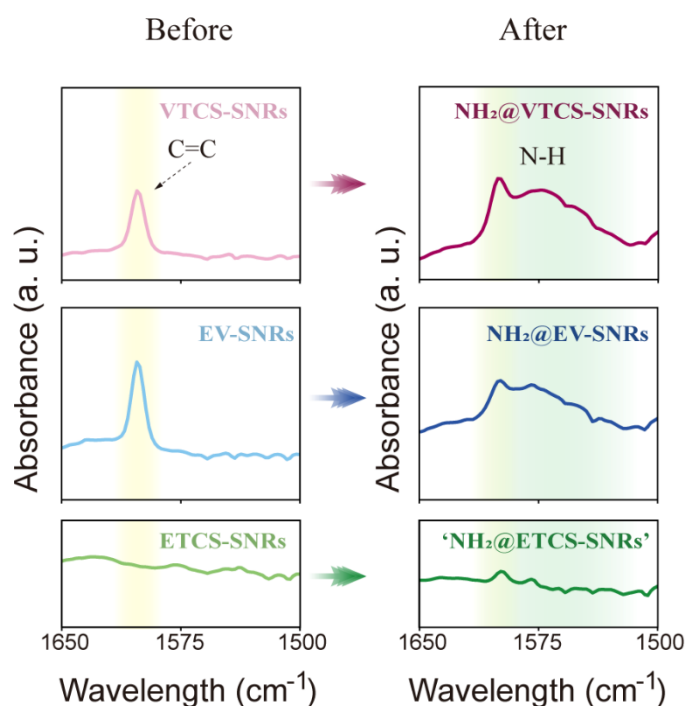
FT-IR spectra

Figure 4.4.9: FT-IR spectrum of the ETCS-SC-SNRs, VTCS-SC-SNRs, EV-MCH-SNRs, ‘NH₂@ETCS-SC-SNRs’, NH₂@VTCS-SC-SNRs, and NH₂@EV-MCH-SNRs in the wavelength range of 1650 to 1500 cm⁻¹.

FT-IR spectrums of the samples before and after the RSF have been collected and shown in **Figure 4.4.9**. No significant difference can be detected from the ETCS-based samples as the exposed inert ethyl groups cannot participate in the reactions with cysteamine. Therefore, quotation marks are used to indicate that the NH₂ groups cannot be really added to the ‘NH₂@ETCS-SC-SNRs’ sample. However, for the samples that consist of the VTCS-based segment, VTCS-SC-SNRs, and EV-MCH-SNRs, sharp -C=C stretching peak[171] at around 1600 cm⁻¹ (highlighted by yellow marks) presents in both samples before chemical modifications. After the thiol-ene click reactions, the broad -N-H bending band[174] of primary amine in the range of ~ 1540 to 1610 cm⁻¹ (highlighted by green marks), which is corresponding to NH₂ deformation mode[174], can be observed on both NH₂@VTCS-SC-SNRs and NH₂@EV-MCH-SNRs samples. These results collectively demonstrate that the RSF can only be applied in the VTCS-based-segment-including MCH-SNRs, and the ETCS-based segment cannot be chemically functionalized because of the lack of the reactive sites. The MCH property of the EV-MCH-SNRs sample is also proved.

Ninhydrin tests

A quick and simple test, the ninhydrin test, is also applied to verify the covalent connection of the introduced functional groups and the MCH structures. As shown in **Figure 4.4.10**, after the reaction between the ninhydrin molecule and the primary amino group, a blue-purple complex is formed, and the color change result can be obtained.

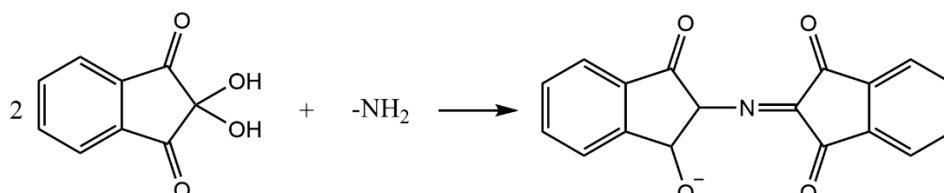


Figure 4.4.10: Scheme of the reaction between ninhydrin molecule and the primary amino group.

For comparison, the samples ETCS-SC-SNRs, VTCS-SC-SNRs, and EV-MCH-SNRs are placed into the same reactor and functionalized by cysteamine for 30 min. Rinsing of the samples after the RSF is important to ensure that no solute residuals adhere to the sample surfaces. Therefore, ethanol/water (v/v at 7:3) and followed by ultrapure water are used in the sample-cleaning process for at least 5 min. Samples are then dried via the freeze-drying method to avoid the collapse of the nanostructures caused by the capillary force that is formed during the solvent evaporation process (**Figure 4.4.11**).

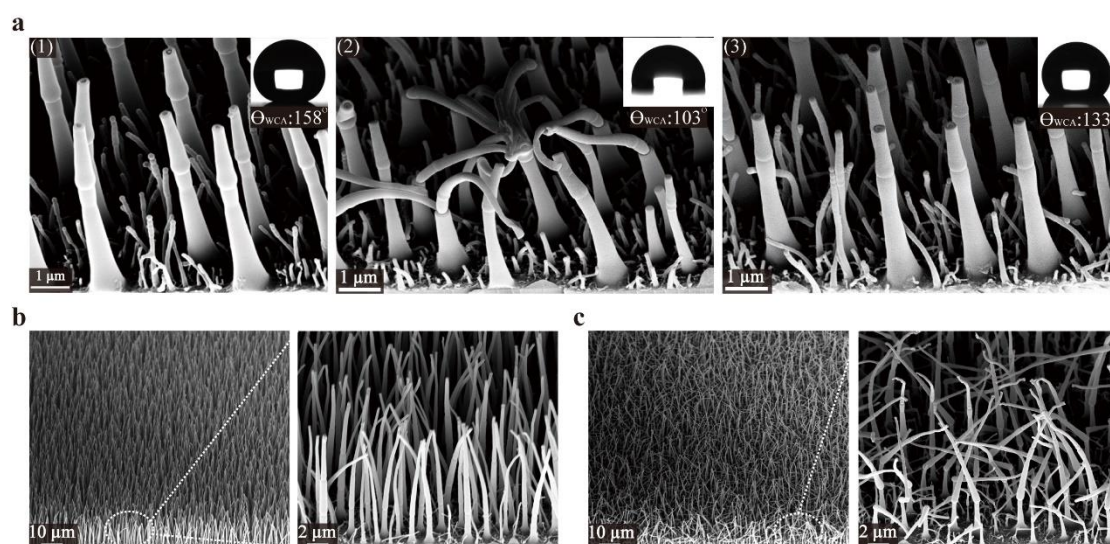


Figure 4.4.11: (a) SEM images of the original (1) EV-SC-SNRs and after drying by (2) N₂-gun and (3) freeze-dryer. SEM images of EEV-MCH-SNRs dried by (b) freeze-dryer and (c) N₂-gun.

The liquids used in the first and last cleaning rounds of the samples are tested with ninhydrin reagents first. As shown in **Figure 4.4.12**, after adding ninhydrin reagents, the first round used liquid changed the color, whereas the last round used liquid remained as clear and transparent as it was initially. The results demonstrate that all the cysteamine residues on the sample surface are entirely washed off. The remaining $-NH_2$ groups that caused the color change on the sample surfaces are covalent-bonded to the MCH-SNRs, not the removable chemical residues.

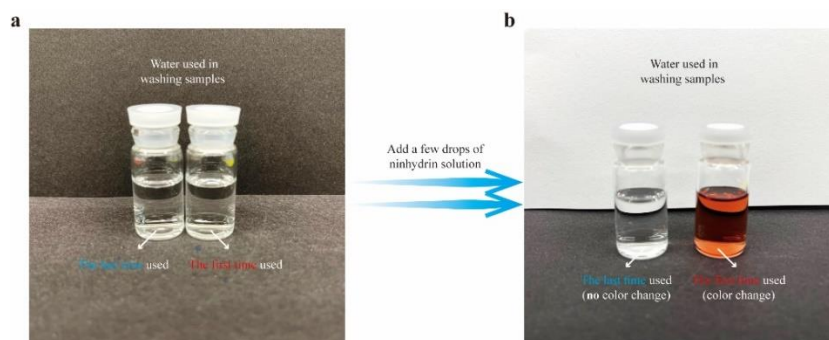


Figure 4.4.12: Collected liquid from the cleaning process (a) before and (b) after adding ninhydrin reagent.

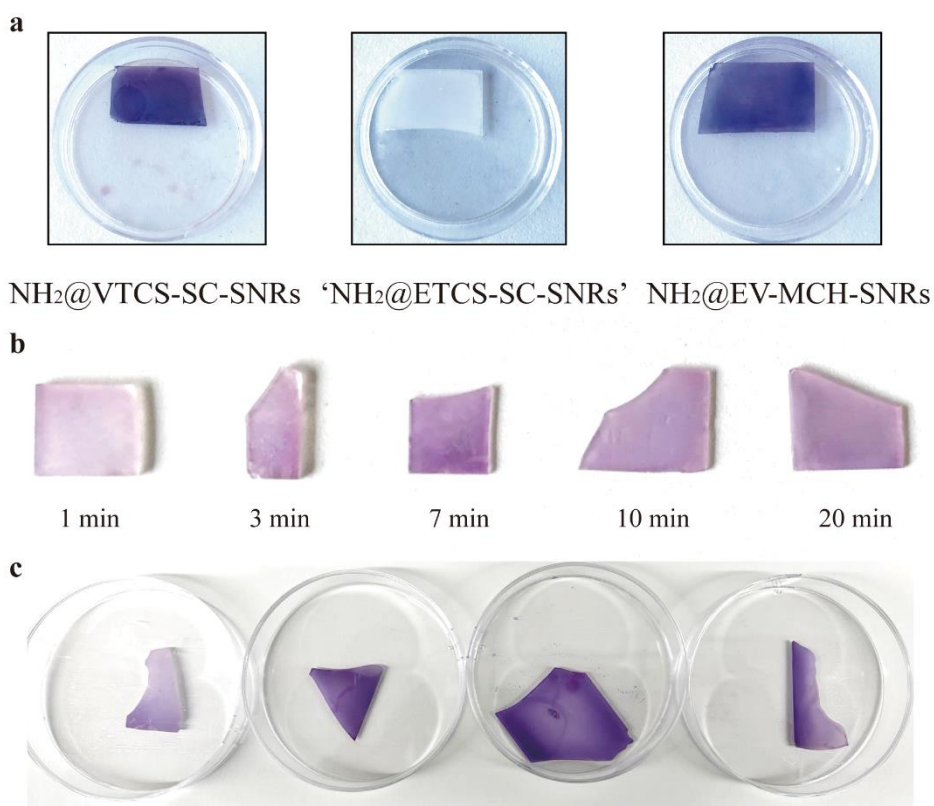


Figure 4.4.13: Ninhydrin test with (a) $NH_2@ETCS-SC-SNRs$, $NH_2@VTCS-SC-SNRs$, $'NH_2@EV-MCH-SNRs'$ samples, (b)

NH₂@EEV-MCH-SNRs sample after the RSF by cysteamine for 1, 3, 7, 10, and 20 min, and (c) several pieces of NH₂@EVE-MCH-SNRs sample after the RSF by cysteamine for 30 min.

Eventually, the samples were separately placed into three Petri dishes and tested with the ninhydrin reagents as described in section 3.6.7. The color change (purple) can be obviously observed from the NH₂@VTCS-SC-SNRs and NH₂@EV-MCH-SNRs samples, as shown in **Figure 4.4.13.a**, whereas the ‘NH₂@ETCS-SC-SNRs’ sample remains its initial color.

Notably, for the EEV-MCH-SNRs samples that have been functionalized by cysteamine under different reaction times (**Figure 4.4.13.b**), from 1 min to 20 min, the difference in color change can hardly be visually distinguished. Conversely, several pieces from the sample (EVE-MCH-SNRs) that are modified for 30 min (**Figure 4.4.13.c**) may respond slightly differently in ninhydrin tests. Therefore, the ninhydrin test can only be used to quickly and simply confirm the occurrence of the thiol-ene click reactions.

The results are consistent with the FT-IR test that the RSF only occurred on the VTCS-based-segment-included SNRs, such as VTCS-SC-SNRs, EV-MCH-SNRs, EEV-MCH-SNRs, and EVE-MCH-SNRs samples.

TEM confirmation

To further prove the region-selectivity of the chemical functionalization on MCH-SNRs, TEM and STEM-EDX techniques are used to visually reveal the areas in which the RSF can occur. The characteristic element, sulfur (“S”), is used as the representative of the successful RSF (from the bond -R-S-R-), and its distribution is able to indicate the areas that have been functionalized. From **Figure 4.4.14**, it is clear that the S element is mainly concentrated on the VTCS segment, some sporadic weak signals observed from the ETCS-based segments might result from the random deposition of small VTCS-based siloxane species on the side surface of the existed ETCS rods during the hydrolysis and condensation reactions in the gas phase as explained by the d-DAGS mechanism (section 4.3.1)[23].

In addition, the RSF was also successfully applied to the SMHs samples, as shown in TEM and STEM-EDX images (**Figure 4.4.14.e**).

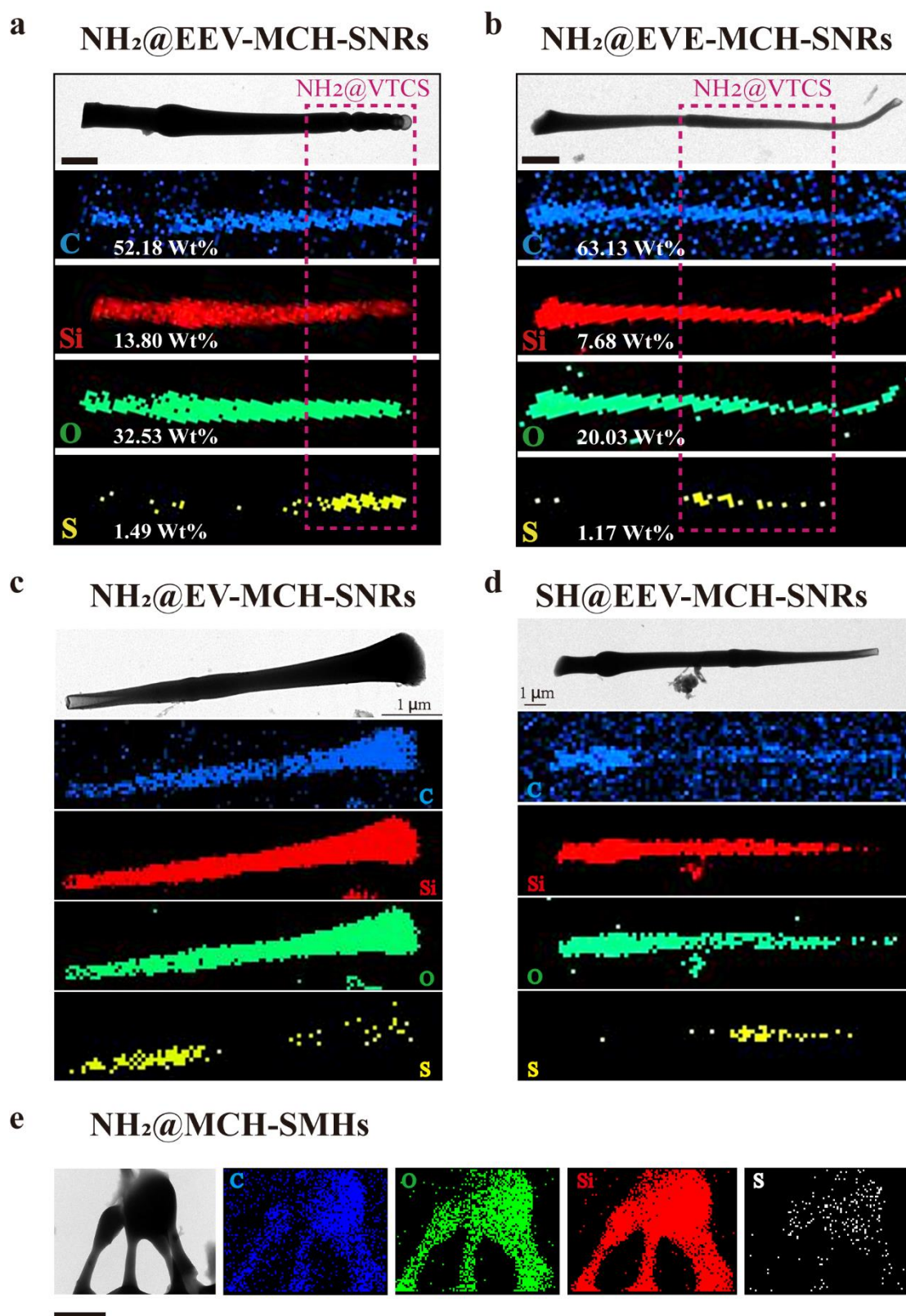


Figure 4.4.14: TEM and the corresponding STEM-EDX images of (a) $\text{NH}_2@$ EEV-MCH-SNRs, (b) $\text{NH}_2@$ EVE-MCH-SNRs, (c) $\text{NH}_2@$ EV-MCH-SNRs, and (d) $\text{SH}@$ EEV-MCH-SNRs samples. Unlabeled scale bar, 1 μm .

All in all, the above three different methods lead to the following conclusions:

- The RSF can be successfully conducted only on the VTCS segment from different types of MCH samples.
- ETCS segment cannot be functionalized because of its inert chemical properties. A small number of weak signals detected from the ETCS segment surface are from the random deposition of the VTCS-based polysiloxanes in the gas phase.
- The MCH property of the bamboo-shaped nanostructures synthesized via the d-DAGS method with two different precursors is proved. Depending on the position of the modifiable regions, which bear the reactive sites on the surface, different parts of the MCH structures can be selectively functionalized.

4.4.7 Surface wetting properties and the RSP theory

Because the MCH-SNRs are behaving as a kind of functional coating on the solid surface, some surface properties, for example, the hydrophobicity of the obtained samples, are evaluated. As shown in **Figure 4.4.15**, the samples that have 2 or 3 segments are superhydrophobic with a low θ_{WSA} ($< 10^\circ$), whereas the ETCS-SNRs sample is just hydrophobic due to its less rough property, which is consistent with the conclusions derived in section 4.3.4 that the hydrophobicity of the bamboo-shaped structure is dependent on their height, more specifically, the number of segment[23].

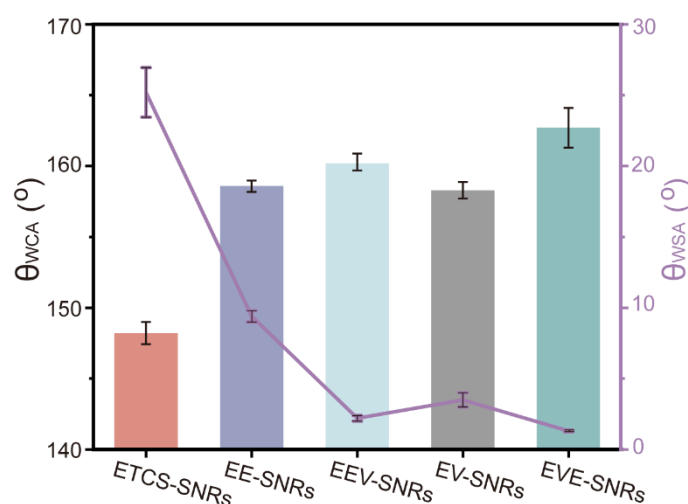


Figure 4.4.15: θ_{WCA} and θ_{WSA} of the as-prepared samples.

However, the RSF treatment on MCH-SNRs is able to modify the surface chemistry and the surface wetting properties of the samples because the added functional groups,

such as -NH_2 and -SH , are polar and can make the sample surface more hydrophilic. We proposed that the accumulation of the terminal groups is dependent on the number of reactive sites on the modifiable region and the reaction time. On the one hand, it is difficult to calculate the exact number of reactive sites on the surface of the bamboo-shaped MCH nanostructures. On the other hand, because the number of reactive sites, namely, the exposure of the vinyl groups, is decided from the geometrical parameters of the VTCS-based segment, we may assume it is constant in an individual MCH-SNRs sample due to the homogeneity of the bamboo-shaped morphology. Therefore, the reaction time is considered a perfect variable when investing the effects of the RSF on surface wetting behaviors.

Some literatures have reported that similar thiol-ene click reactions can be completed in a few seconds or minutes [110, 114], the loading of -NH_2 groups is therefore evaluated by measuring the θ_{WCA} of the $\text{NH}_2@EV\text{-MCH-SNRs}$, $\text{NH}_2@EEV\text{-MCH-SNRs}$, and $\text{NH}_2@EVE\text{-MCH-SNRs}$ samples for the reaction time of 3, 5, 10, 20, 30, 60, and 90 min, respectively.

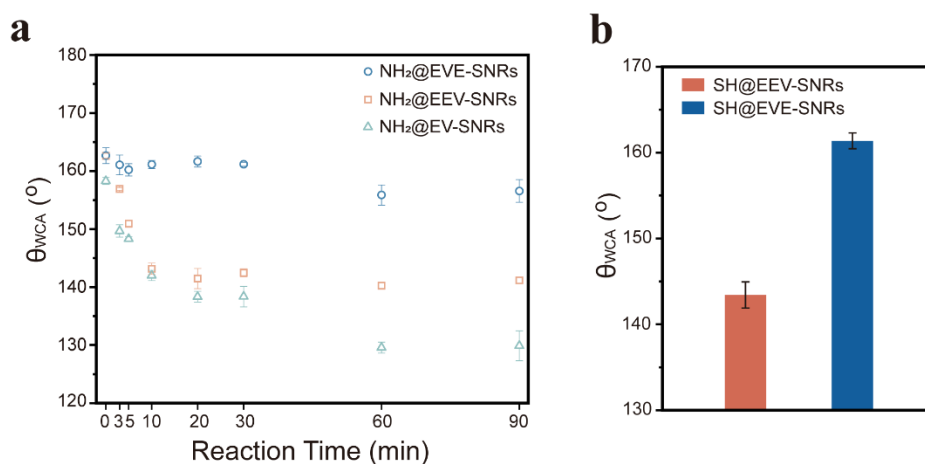


Figure 4.4.16: (a) Plot of θ_{WCA} of $\text{NH}_2@EV\text{-MCH-SNRs}$, $\text{NH}_2@EEV\text{-MCH-SNRs}$, and $\text{NH}_2@EVE\text{-MCH-SNRs}$ samples after being functionalized for a specific reaction time. (b) θ_{WCA} of SH@EEV-MCH-SNRs and SH@EVE-MCH-SNRs samples after being functionalized by 1,4-butanedithiol.

$\text{NH}_2@EV\text{-MCH-SNRs}$ and $\text{NH}_2@EEV\text{-MCH-SNRs}$ samples perform similarly in the first 20 min of the RSF, where a significant decrease of θ_{WCA} from $\sim 160^\circ$ to $\sim 140^\circ$ can be observed from **Figure 4.4.16.a**. Notably, both samples lose their superhydrophobicity after ~ 3 to 5 min chemical modifications, indicating the

unignorable effects on surface anti-wetting properties caused by the loading of terminal functional groups. However, from 30 min to 90 min reactions, a relatively steady θ_{WCA} is maintained by the $NH_2@EEV-MCH-SNRs$ sample, whereas the θ_{WCA} of the $NH_2@EV-MCH-SNRs$ sample shows a slow downward trend. Even though the maximum value of the loaded amino groups can hardly be estimated, their accumulation process over reaction time is reflected in the θ_{WCA} measurements.

On the contrary, the $NH_2@EVE-MCH-SNRs$ sample is able to maintain superhydrophobic ($\sim 160^\circ$) for 90 min (**Figure 4.4.16.a**). The same results are derived from the reactions with 1, 4-butanedithiol for 30 min as well (**Figure 4.4.16.b**). Compared to the decrease of θ_{WCA} as seen from the $SH@EEV-MCH-SNRs$ sample, θ_{WCA} of the $SH@EVE-MCH-SNRs$ sample stays at $\sim 160^\circ$. As the success of the RSF on EVE-MCH-SNRs samples has been proved from previous tests (section 4.4.6), a new theory, so-called region-selective protection (RSP), is therefore proposed to explain this phenomenon:

- ❖ When the modifiable VTCS-based segment located between two or more inert ETCS-based segments on MCH-SNRs, namely, (m)E-V-(n)E-MCH-SNRs, where m and $n \geq 1$, the loaded terminal functional groups after the RSF can be selectively protected by the ETCS-based segments through physically blocking their contact with water or other solvents.

To further evaluate the surface wetting behaviors of the MCH-SNRs samples, especially the RSP mechanism, both self-cleaning properties and the ability of water droplets bouncing off the substrate surface of the $NH_2@EEV-MCH-SNRs$ and $NH_2@EVE-MCH-SNRs$ samples are characterized.

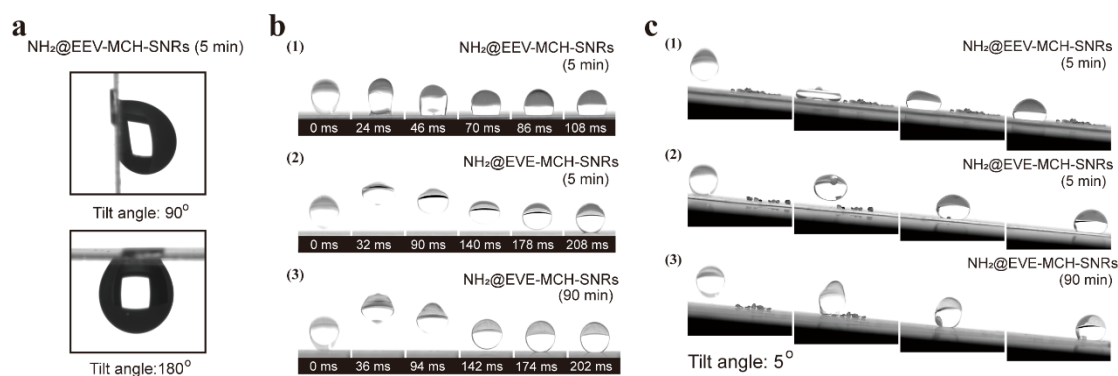


Figure 4.4.17: (a) Images of water droplet (10 μ L) staying on the $NH_2@EEV-MCH-SNRs$ sample (RT: 5 min) surface at a tilt angle of 90°

and 180°, respectively. (b) Snapshot of water droplet (10 μ L) bouncing (maximum position) on the NH₂@EEV-MCH-SNRs (*RT*: 5 min), NH₂@EVE-MCH-SNRs (*RT*: 5 min), and NH₂@EVE-MCH-SNRs (*RT*: 90 min) samples. $We = 9$. (c) Self-cleaning test of NH₂@EEV-MCH-SNRs (*RT*: 5 min), NH₂@EVE-MCH-SNRs (*RT*: 5 min), and NH₂@EVE-MCH-SNRs (*RT*: 90 min) samples at a tilt angle of 5°.

As shown in **Figure 4.4.17.a**, the pinning effect of a water droplet on the surface of NH₂@EEV-MCH-SNRs sample that is functionalized with cysteamine for 5 min can be ascribed to the increased adhesion force between the modified substrate surface bearing exposed amino groups and the water droplet. Meanwhile, only a small amount of the groups is added due to the short reaction time, which results in the superhydrophobic property of the sample being maintained. Therefore, the transition of the surface wetting mode from the lotus effect[175] to the rose petal effect[176] is achieved in a controlled situation, which is important in further functional surface coating design[177]. Similarly, the free-falling water droplet (10 μ L) released 1.5 cm above the sample can hardly bounce on the NH₂@EEV-MCH-SNRs sample (*RT*: 5 min) but is able to re-bounce on the NH₂@EVE-MCH-SNRs samples for respective 3 and 4 times even the sample is functionalized with cysteamine for 90 min (**Figure 4.4.17.b**). Self-cleaning tests with the above samples exhibit the same results, as shown in **Figure 4.4.17.c**, the rolling-off water droplet can only take the dirt away from the NH₂@EVE-MCH-SNRs samples, but pins on the NH₂@EEV-MCH-SNRs sample at the tilt angle of 5°.

In summary, the surface anti-wetting properties of the EVE-MCH-SNRs samples after the RSF are maintained/protected due to the RSP theory, but of the EV-MCH-SNRs and EEV-MCH-SNRs samples, their surface chemical properties are modified by the connected terminal functional groups, and their superhydrophobic property and the self-cleaning ability are therefore significantly changed due to the direct exposure of the added groups at the surface solid-liquid interfaces.

4.4.8 Visualization of water penetration status

To better understand the surface wetting properties of the MCH samples before and after the RSF, confocal microscopy was the first time employed in detecting the water droplet penetration status. Meanwhile, in addition to the conventional wetting modes,

we studied the newly developed and widely discussed wetting mode, the intermediate/partial/mixed wetting states [131, 178], in a more intuitive way with the help of the Atto 633-COOH fluorescent dye molecules. The dye-containing water droplet enables to emit fluorescent signals from the interface of the solid-liquid-vapor when it is sitting on the surface of the sample [179] due to the coffee-ring effect [180], from which a layer of small dye molecules concentrated around the triple-line resulted from the evaporation of water droplet. Therefore, the penetration depths of the water droplet can be easily captured and analyzed instead of studying the fluorescently labeled micro- and nanostructures after long-time staining. The scheme of the sample surface, structure surface, and solid-liquid-vapor interfaces is shown in **Figure 4.4.18**.

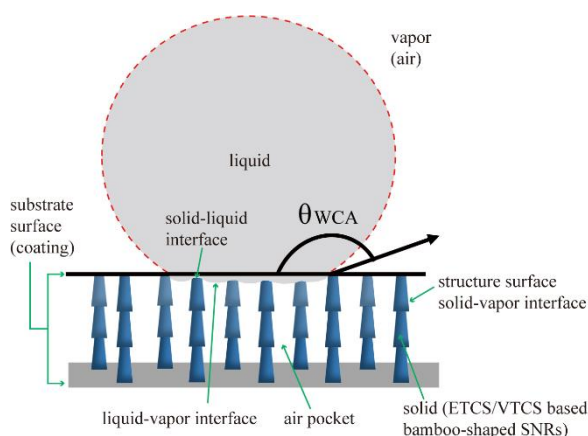


Figure 4.4.18: Scheme illustration of the water droplet on the superhydrophobic surface of the bamboo-shaped SNRs coated substrate.

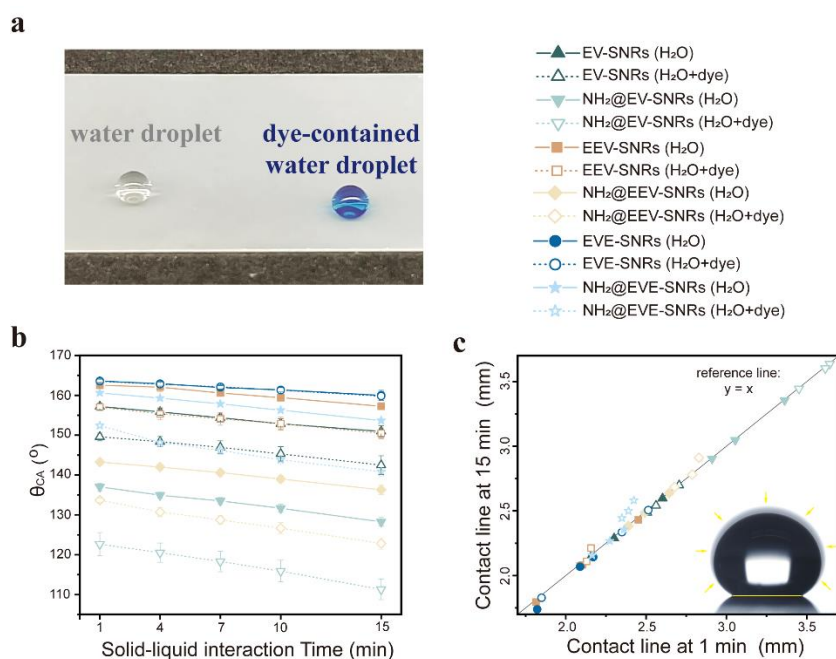


Figure 4.4.19: (a) Images of water droplet (10 μL) and Atto 633-COOH fluorescent dye-containing water droplet (10 μL) sitting on the $\text{NH}_2\text{@EVE-MCH-SNRs}$ sample. (b-c) Plot of θ_{CA} as a function of time of 10 μL pure water droplet and dye-containing water droplet on the sample surfaces, and length ratio of the contact line measured at 15 and 1 min solid-liquid interaction (reference line: $y = x$), of the EV-MCH-SNRs, EEV-MCH-SNRs, and EVE-MCH-SNRs samples before and after the RSF (30 min) with cysteamine. Insert in (c) is the illustration of the water droplet shrinking process. All measurements were conducted in lab conditions ($\sim 23\text{ }^\circ\text{C}$, 50% RH).

The influences of replacing pure water droplet with dye-containing water droplet on the sample surface wetting properties and the confocal microscopy imaging process are first investigated (**Figure 4.4.19.a**). In order to reduce the undesirable effects resulting from the water droplet evaporation, all measurements, as well as the imaging process, are completed within 15 min as that is considered the constant contact line mode [150, 151], indicating that the penetration depth of the water droplet dominates the different wetting performances. Compared with the pure water droplet, the dye-containing water droplet performs similarly in contact with different MCH samples, as demonstrated by the proportional decrease in θ_{CA} measurements (**Figure 4.4.19.b**) as well as the nearly constant solid-liquid contact line (**Figure 4.4.19.c**).

Even though the effects (evaporation) of using the dye-containing water droplet in confocal microscopy imaging process might be negligible, a small decrease of the θ_{CA} ($\sim 3\% - 10\%$) can be observed (at 1 min solid-liquid interaction) from the EV-MCH-SNRs, $\text{NH}_2\text{@EV-MCH-SNRs}$, EEV-MCH-SNRs, and $\text{NH}_2\text{@EEV-MCH-SNRs}$ samples, whereas the θ_{CA} change from the EVE-MCH-SNRs sample is close to 0. The RSP theory can be used to explain this phenomenon, as the dye molecules in the water droplet have almost no effect on the ethyl-group-based superhydrophobic surfaces [179]. Nevertheless, the $\sim 5\%$ decrease detected from the $\text{NH}_2\text{@EVE-MCH-SNRs}$ sample demonstrates the possible contact between the water droplet and the loaded $-\text{NH}_2$ groups, which may have resulted from the imperfect uniformity of the EVE-MCH-SNRs structures, especially after the RSF, some undesirable collapses and bending of the structures may exist.

Notably, as reported from the literature [179], different types of dye molecules, for

example, different molecular weights and different functional groups involved, may have different impacts on the imaging process, more dye molecules will be investigated in the future, hopefully, to improve the resolution of solid-liquid and liquid-vapor interfaces. Eventually, the Atto 633-COOH fluorescent dye-containing water droplet is used in acquiring the confocal microscopy images.

General settings and parameters of the confocal microscopy have been summarized in section 3.6.14, some system and display settings applied in acquiring the 2D and 3D images presented in this thesis are shown in **Table 4.4.1**.

Table 4.4.1: System & display settings used for acquiring the 2D and 3D confocal microscopy images.

Samples	Confocal Settings (Pinhole: 95.5 μm , z-step: 0.16 μm)				Display Settings					
	Channel Resolution	Laser Intensity (%)	Gain PMT (631-644 nm)	Gain HyD (645-720 nm)	Fluorescence Channel			Reflectance Channel		
					Min	Max	γ	Min	Max	γ
EEV-MCH-SNRs	12-bit	0.8	800	10	0	59	1	1299	4091	1
NH ₂ @EEV-MCH-SNRs	(0-4095)				107	839	1.5	523	4091	1.5
EVE-MCH-SNRs	12-bit	0.8	800	10	0	27	1	1007	4091	1
NH ₂ @EVE-MCH-SNRs	(0-4095)				0	27	1	2759	4091	0.8
EV-MCH-SNRs	12-bit	Flu. 0.7	611.8	10	5	64	1	60	328	1
NH ₂ @EV-MCH-SNRs	(0-4095)	Ref. 0.2			0	57	1	36	344	1
MCH-SMHs	8-bit	0.8	683.6	10	0	27	1.5	36	255	1.5
NH ₂ @MCH-SMHs	(0-255)				17	157	1.5	14	255	1.5
EV-SNRs (no droplet)	12-bit (0-4095)	Ref. 0.2	611.8	10	-	-	-	356	3091	1

As the reflectance signals (green) are originating from the solid-vapor and liquid-vapor interfaces, they can be used to indicate the profile of the structures, especially their bottom positions (substrate), as shown in **Figure 4.4.20**. Meanwhile, the unwetted area can also be represented by the reflectance signals.

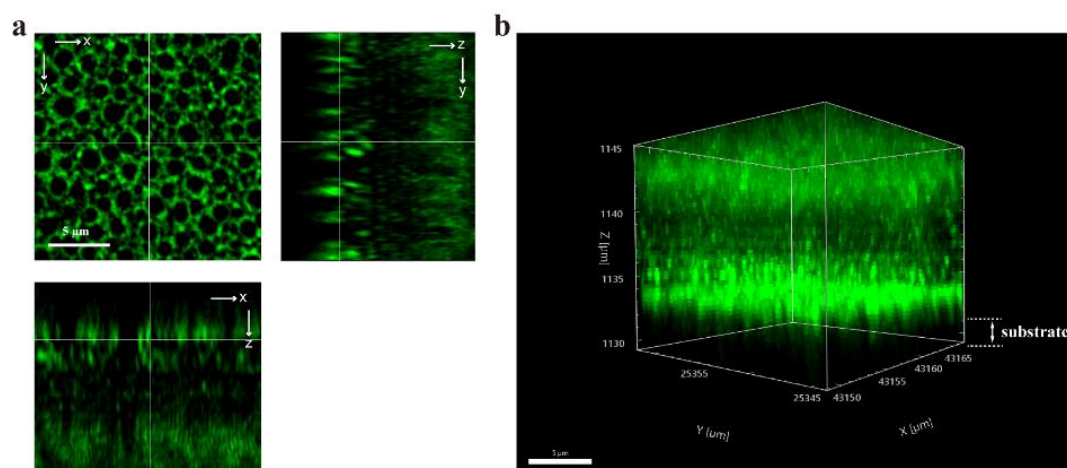


Figure 4.4.20: Confocal microscopy images of the EV-MCH-SNRs sample without water droplet on top, including (a) X-Y slicers and X-Z, Y-Z cross-sectional images and (b) 3D z-stack images.

The bottom of the structure can be easily identified because no reflectance signals can be detected from the substrate.

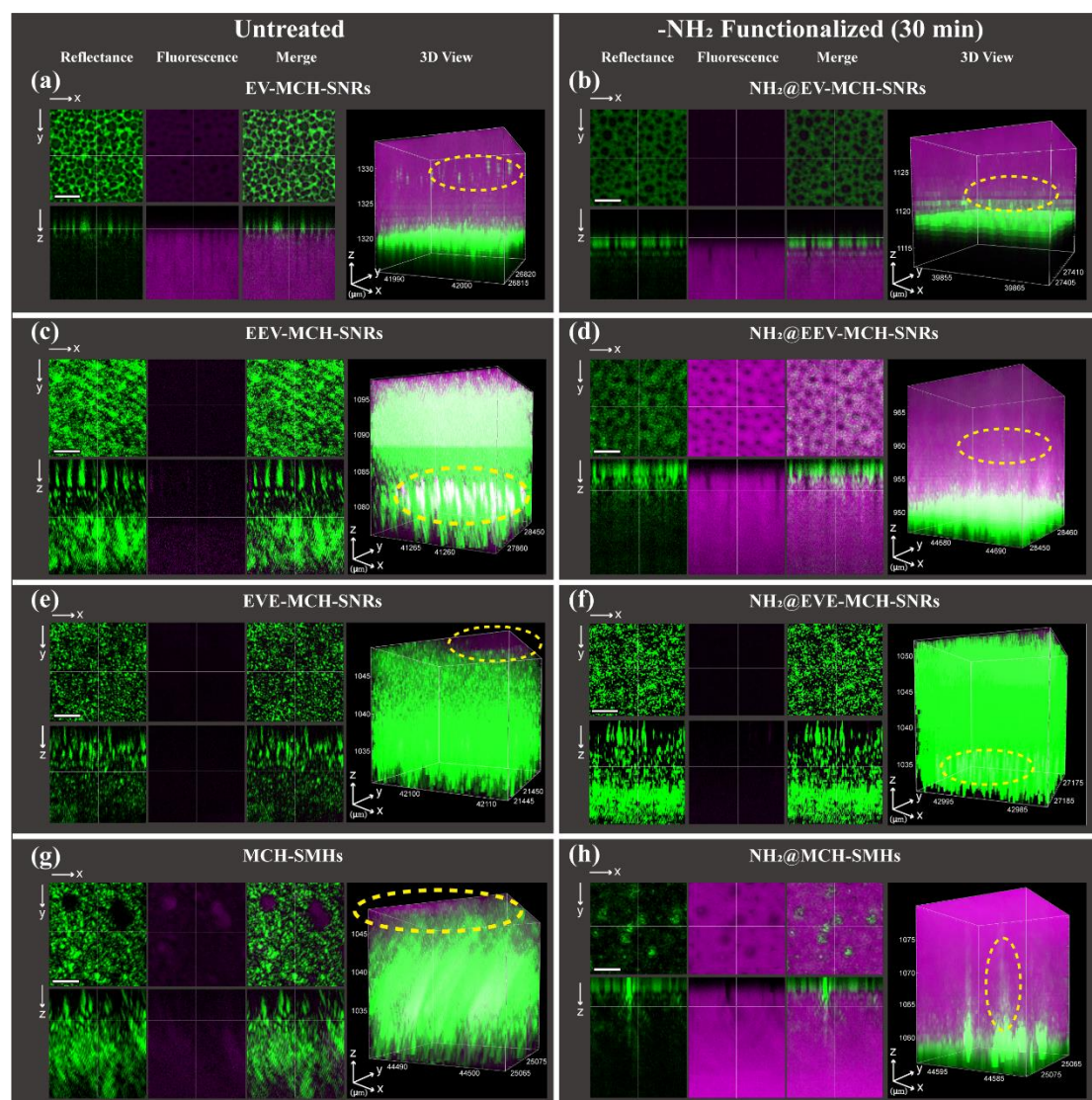


Figure 4.4.21: 2D and 3D images acquired from the confocal microscopy with dye-containing water droplet sitting on the (a, c, e, g) EV-MCH-SNRs, EEV-MCH-SNRs, EVE-MCH-SNRs, and MCH-SMHs samples (b, d, f, h) NH_2 @EV-MCH-SNRs, NH_2 @EEV-MCH-SNRs, NH_2 @EVE-MCH-SNRs, and NH_2 @MCH-SMHs samples. Traces of reflectance and fluorescent signals detected between wetted (magenta) and unwetted (green) areas are circled in the pictures.

As shown in **Figure 4.4.21**, fluorescent signals (magenta) originating from the small dye molecules in the water droplet is used to represent the wetted area, i.e., water penetration depth. Through comparing the magenta area of the respective MCH samples before (a, c, e, and g) and after (b, d, f, and h) the RSF, a general conclusion is derived that the dye-containing water droplet can infiltrate deeper to the $-NH_2$ groups modified samples except for the $NH_2@EVE-MCH-SNRs$ sample.

In specific to each sample, the following results are obtained:

First of all, traces of the reflectance signals (as circled in figure a, b, d, and h) are detected from the wetted area, indicating the presence of the plastrons that are trapped between the solid and liquid phases during the water penetrating process. On the contrary, traces of the fluorescent signals (as circled in figures c and f) detected from the unwetted area may demonstrate that the nonuniformity of the solid-liquid-vapor contact area [131], namely, dye molecules/ tiny dye-containing water droplets may have infiltrated the voids of the MCH structures.

Secondly, EV-MCH-SNRs and $NH_2@EV-MCH-SNRs$ samples exhibit similar anti-wetting properties. During the imaging process (15 min), with the respective decrease of θ_{CA} from $\sim 150^\circ$ to $\sim 143^\circ$ (**Figure 4.4.21.a**) and $\sim 123^\circ$ to $\sim 111^\circ$ (**Figure 4.4.21.b**), both samples are deeply wetted by the dye-containing water droplets, especially the $NH_2@EV-MCH-SNRs$ sample, a slight deeper water penetration level can be observed from the images.

Thirdly, EEV-MCH-SNRs and $NH_2@EEV-MCH-SNRs$ samples are much higher than the EV-MCH-SNRs and $NH_2@EV-MCH-SNRs$ samples (**Figure 4.4.6.b**), thereby exhibiting stronger water-repelling ability. EEV-MCH-SNRs sample enables to maintain its high θ_{CA} ($\sim 157^\circ$ at 1 min to $\sim 150^\circ$ at 15 min) during the imaging process. By considering the detected fluorescent signals below the water penetration edge, an intermediate wetting mode might be used to explain its wetting behaviour (**Figure 4.4.21.c**, **Figure 4.4.22.a**). Similarly, as shown in **Figure 4.4.21.d** and **Figure 4.4.22.b**, the functionalized $NH_2@EEV-MCH-SNRs$ sample is losing its robust anti-wetting property as the loaded $-NH_2$ groups are located at the top segment, from where they are directly exposed to the water droplet. The increased surface energy, as well as the affinity to water droplets, are able to lower the θ_{CA} of the sample. However, due to the special position of the modified VTCS-based segment of the sample, two ETCS-based

segments below the top segment are able to prevent further penetration of the dye-containing water droplets, a bigger θ_{CA} than the $\text{NH}_2@\text{EV-MCH-SNRs}$ sample is therefore obtained. The wetting state transition process (water penetration) and the intermediate wetting mode are visually revealed.

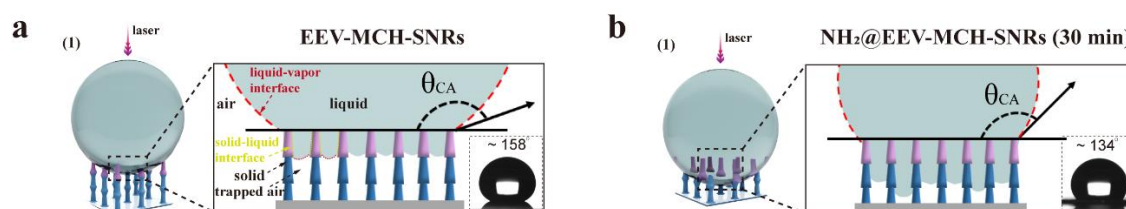


Figure 4.4.22: Schematic illustrations of the possible wetting mode of (a) EEV-MCH-SNRs and (b) $\text{NH}_2@\text{EEV-MCH-SNRs}$ samples.

Fourthly, EVE-MCH-SNRs and $\text{NH}_2@\text{EVE-MCH-SNRs}$ samples are able to maintain their unwetted state with very high θ_{CA} ($> 160^\circ$) for the whole measuring process (**Figure 4.4.21.e-f**). The weak fluorescent signals can only be observed from the very top of the structures, as circled in the 3D view (**Figure 4.4.21.e**). Traces of feeble fluorescent signals observed from the base area in 3D images (**Figure 4.4.21.f**) are consistent with the previous conclusion of the θ_{CA} measurement that the possible contact between the water droplet and the loaded $-\text{NH}_2$ groups may occur in some areas where relatively large voids exist between adjacent EVE-SNRs structures. All in all, it can be concluded that the EVE-MCH-SNRs and $\text{NH}_2@\text{EVE-MCH-SNRs}$ samples are in the Cassie-Baxter state (**Figure 4.4.23.a-b**), which is also consistent with their measured high θ_{CA} (superhydrophobic). The advantage of the RSP mechanism is evident again in that specific molecules (functional groups) can be hidden and protected inside the superhydrophobic surface structures.

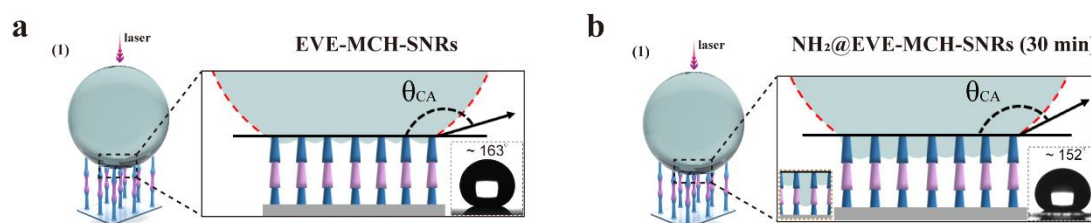


Figure 4.4.23: Schematic illustrations of the possible wetting mode of (a) EVE-MCH-SNRs and (b) $\text{NH}_2@\text{EVE-MCH-SNRs}$ samples.

Additionally, the wetting properties of the MCH-SMHs samples before and after the RSF are also investigated, as shown in **Figure 4.4.21.g-h**. Similar to the EEV-MCH-

SNRs and NH_2 @EEV-MCH-SNRs samples, the unmodified MCH-SMHs sample can hardly be fully wetted by the dye-containing water droplet because its θ_{WCA} is $\sim 150^\circ$, whereas the NH_2 @MCH-SMHs sample shows high affinity to the water droplet. Unlike the other samples, reflectance signals are obvious in the wetted area, which is because of the special mushroom-shaped morphology of the MCH-SMHs, plastrons can be easily formed underneath the sphere mushroom head.

4.4.9 Anti-adhesive application (MCH-SMHs)

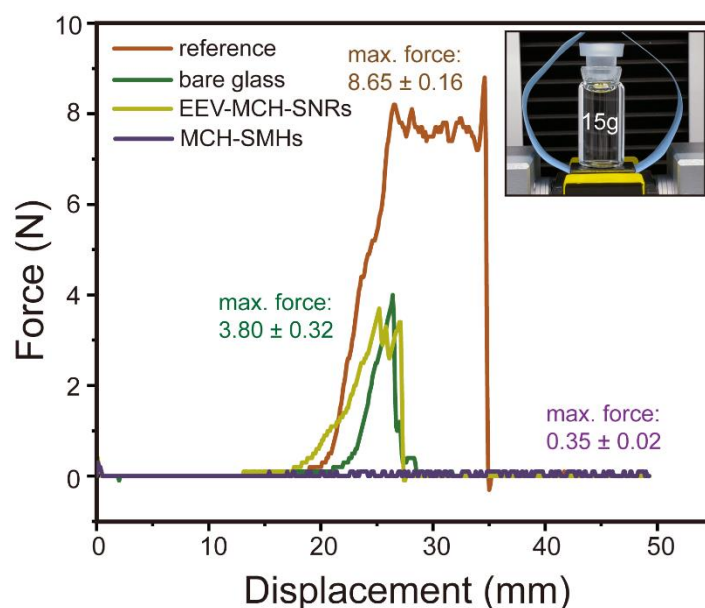


Figure 4.4.24: Adhesive loop tack strength test of different samples. Insert is the picture showing that a weight (15 g) is placed on the contact area for at least 1 min to make sure the tight attach.

MCH-SMHs structures are a kind of promising surface functional coating because of their robust anti-adhesive ability. For comparison, a reference sample¹, a bare glass², a bamboo-shaped EEV-MCH-SNRs coated sample, and the MCH-SMHs coated sample were used in the adhesive loop tack strength test following the instructions in section 3.6.2. At least five measurements were conducted for each sample, and the average results are summarized in **Figure 4.4.24**. The reference sample illustrates the strongest adhesion of the tape used in this test to the samples, with an average maximum adhesion force of 8.65 ± 0.16 N. The bare glass sample and the sample coated with the bamboo-

¹ A glass slide ~ 1.0 mm thick to prevent brokage.

² The substrate used in synthesizing MCH-SMHs structures.

shaped EEV-MCH-SNRs performed similarly in the tests as the thin glass slides are usually used broken. An average maximum adhesion force of 3.80 ± 0.32 N is obtained from five measurements with the bare glass, even though the samples also broke apart, indicating that it is probably the maximum tensile capacity of the glass substrate used in synthesizing the MCH structures. Surprisingly, it is observed that the MCH-SMHs coated sample shows very strong anti-adhesive ability toward the tape with the measured average maximum adhesion force of 0.35 ± 0.02 N.

Scheme of contact area

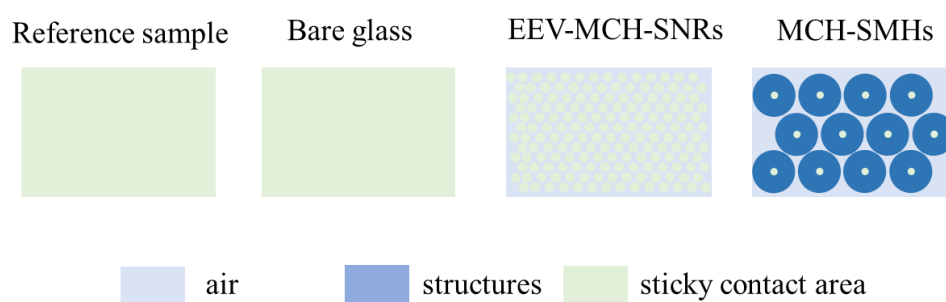


Figure 4.4.25: Scheme illustration of the contact area of different samples.

Considering the special morphology of the MCH-SMHs, a possible explanation for their almost zero adhesive force to sticky tape is proposed, as shown in **Figure 4.4.25**, an important factor, the contact area (surface interaction) between coating structures and the tape, is probably playing the critical role in deciding the anti-adhesive ability of the samples. A huge decrease in the surface interaction of the MCH-SMHs structures and the tape is achieved because of the unique round-top-segment shape of the structures. Moreover, the chemical properties of the DCMVS-based segment may also contribute to their robust anti-adhesive ability, which needs to be investigated in future studies.

Summary and Outlook

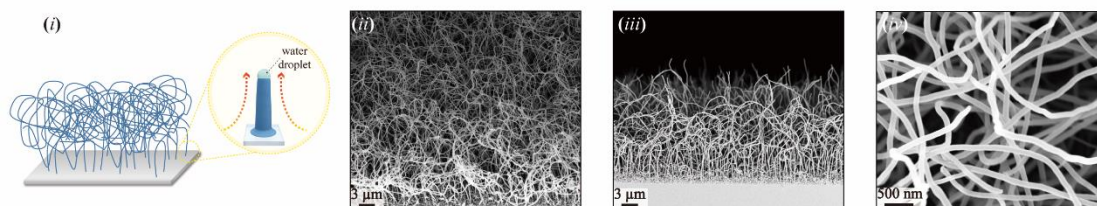
Designing and engineering functional coating structures at the nanometer scale on solid surfaces and interfaces with unique physicochemical and mechanical properties are becoming increasingly crucial in surface and material sciences as the demand for high-performance multifunctional products from the real world have grown in recent years. 1D silicone-based nanostructures, commonly referred to SNFs, have been investigated and developed since their discovery in the early 2000s because of their many benefits, for example, the cheap precursors, facile and efficient reactions with water, applicability to various substrates, and their inherent oxidative stability, chemical inertness, and dielectric and thermal properties. In order to gain a deeper understanding of the mechanism of growing morphological-controlled silicone-based homogeneous and heterogeneous nanostructures on different types of solid substrates, and obtain the design freedom in tailoring the functional structures with desired physicochemical properties and performance characteristics, from synthesis methods to chemical functionalization and practical applications have been systematically investigated in this work.

A **Summary Figure** is provided below to intuitively exhibit synthesis methods and silicone-based nanostructures reported in this thesis. Moreover, an outlook method of producing hierarchical structures that will be studied in the future is also presented.

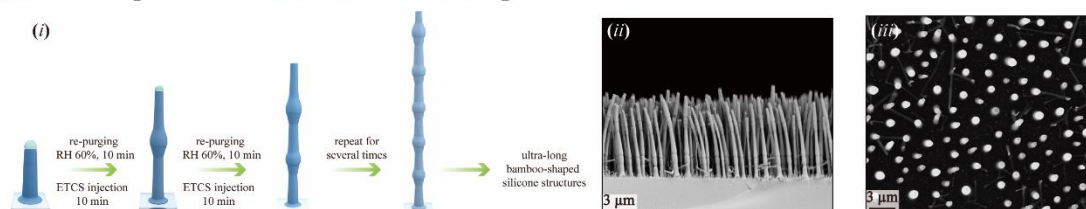
In the first part of this work, systematic investigations of the effects of the synthesis conditions on the morphology and surface properties of the single-component-based silicone nanostructures were conducted. Benefiting from the DAGS mechanism (a kind of CVD method) studied in our group for many years, all the silicone-based nanostructures could be efficiently produced in the gas phase at room temperature ($\sim 23.0\text{ }^{\circ}\text{C}$). Different combinations of the growing parameters, including *RH*, *RT*, *VOL*, and types of substrates, have been systematically investigated in a series of testing experiments.

SC silicone nanostructures:

(a). One-step DAGS method, conventional SC-SNFs:

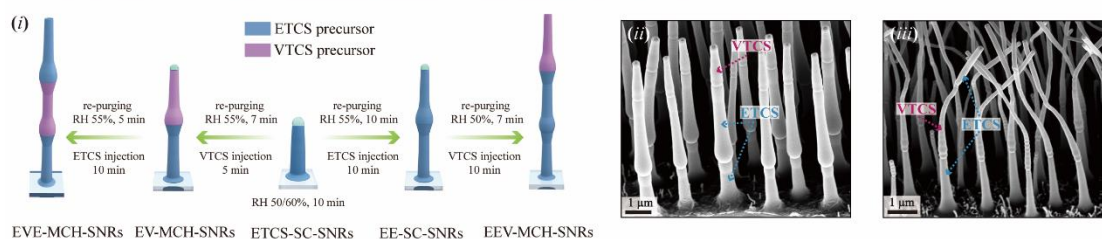


(b). One-step d-DAGS method, bamboo-shaped SC-SNRs:

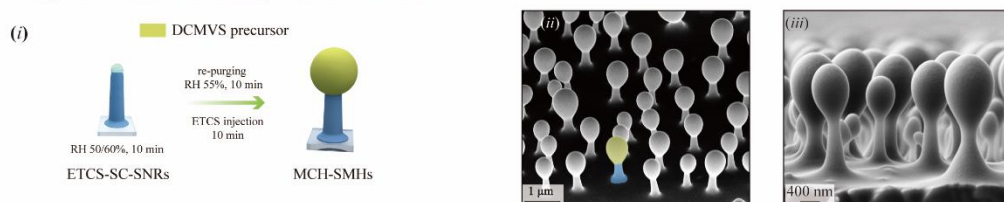


MCH silicone nanostructures:

(c). One-step d-DAGS method, bamboo-shaped MCH-SNRs:

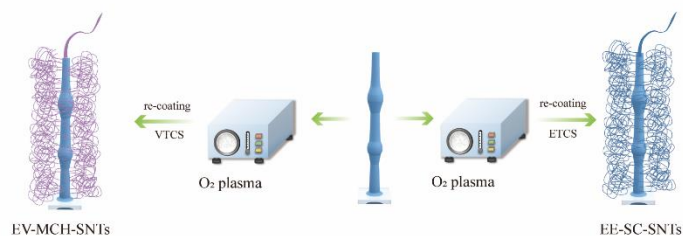


(d). One-step d-DAGS method, MCH-SMHs:



Outlook:

(e). Two-steps O₂ plasma treatment, Silicone nanotrees (SNTs):



Summary Figure: (a-d) Methods used in synthesizing different home- and heterogenous silicone-based micro- and nanostructures. (e) Outlook of a novel two-step method that can be used in fabricating the hierarchal home- and heterogenous silicone-based micro- and nanostructures.

Even though all parameters are collectively affecting the final results, the critical role each factor played in the polysiloxanes shaping process can be identified as follows: *(i)* Diameter of the base segment, in case of multi-segment structures are involved, is dominated by the *RH* value applied in the pre-treatment steps. With increasing the *RH* value, a more extensive water droplet can be condensed on the surface of the substrate; thereby, the structures with corresponding diameters are produced. From filaments (low *RH* value) to rods to big volcanoes and rings (high *RH* value), the required shape of the formed structures can be customized by regulating the initial *RH* value. *(ii)* *RT* plays a significant role in deciding the height of the synthesized structures as the growth of the silicone-based nanostructures follows the “tip-growth” mode. *(iii)* *VOL* contributes to the ratio between different reactants, namely, water and silanes, which is less critical in controlling the final morphology as the volume of the water droplet located at the top cavity of the structure is mainly decided by the *RH* value. However, *VOL* can also be adjusted to improve the reaction efficiency and produce a perfect micro- and nanostructure. *(iv)* Depending on the types of substrates, different surface activation methods might be used. As presented in this work, the optimal growth conditions of *VOL*: 800 μL , *RH*: 50% \pm 1%, and *RT*: 120 min under room temperature are preferred in fabricating ETCS-SC-SNRs on cellulosic-paper-based substrate. Understanding each factor’s role guides synthesizing the silicone-based nanostructures with the desired shape, but flexible adjustments on these factors in different structural needs are also essential.

In the second part of this thesis, following up on the growing instructions investigated in the first project, practical applications based on the typical ETCS-SC-SNRs structures were explored by replacing the lab frequently-used glass substrate with the cellulosic-paper-based substrate. Different from the conventional SNFs, the homogeneous ETCS-SC-SNRs are the first time, successfully synthesized on the cellulosic-paper-based substrate, which endows the fibrous texture of the pristine cellulosic paper with a micro-nano hierarchical morphology. Robust superhydrophobicity is achieved on the SNRs-paper surface with θ_{WCA} of $162^\circ \pm 2^\circ$. Due to their inert low-surface-energy chemical compositions and the cross-linked structures, the engineered paper exhibited excellent durability towards chemical and extreme environmental perturbations and mechanical damages. In addition, scale-up fabrications extended this coating strategy to A4 -paper, more practical applications are

therefore investigated. For example, the engineered SNRs-A4-paper can be directly utilized in commercial inkjet printers or handwritten with customized-made water-soluble ink without negatively affecting their appearance, integrity, and anti-wetting properties. Similarly, the ETCS-SC-SNRs coatings, as a protective layer, can also be fabricated on cellulosic paper that has been preprinted or written with some contents. The modified cellulosic paper prints, SNRs-p-paper, presented excellent waterproof functionality and enhanced strength against water exposure.

Notably, the ETCS-SC-SNRs modified substrate surface shows excellent antimicrobial functionality. Because of the intrinsic superhydrophobicity of the ETCS-SC-SNRs coatings, necessary growth conditions for microorganisms, namely, moisture and nutrients, can hardly be created and maintained around the sample surfaces. In addition, after specific surface treatment, the ETCS-SC-SNRs coatings had successfully replicated on other cellulosic-paper-based substrates, such as letter envelopes, papers, printings, and packaging materials, to provide surface protection for their outdoor use.

In the third part of this thesis, the in-situ fabrication of bamboo-shaped SNRs based on the d-DAGS mechanism was developed. This newly developed d-DAGS strategy enables controlling and adjusting the geometric properties of each single segment during its growth process, thereby creating a series of bamboo-shaped SNRs with segment numbers 1 to 6 and ultra-long structures with segment numbers 12 and 18. The growth mechanism, physicochemical properties, and potential applications of the newly synthesized bamboo-shaped SC-SNRs were systematically investigated. The “tip-growth” model of the d-DAGS method was proved, illustrating the decisive role of the shape of the water droplet located at the inverted triangular conical cavity at the segment top during the growth/deposition process of the polysiloxanes.

The as-prepared bamboo-shaped SC-SNRs samples presented robust and stable superhydrophobicity under static and dynamic conditions. It was demonstrated that the higher structures have better anti-wetting properties, particularly for the ultra-long structures with the perfect average θ_{WCA} to be nearly 180° as well as the θ_{WSA} to be lower than 1° . Additionally, the bamboo-shaped SC-SNRs showed great potential for applications in complex environments due to their enhanced chemical and mechanical durability and self-cleaning properties compared to conventional SNFs. The 6-seg-ETCS-SNRs presented excellent performance in water harvesting applications with a

maximum WCR of $32.3 \pm 0.6 \text{ mg}\cdot\text{cm}^{-2}\cdot\text{min}^{-1}$. As a material that relies on superhydrophobic structural design for efficient water collection, it exhibits more robust application prospects than existing surface designs based on wettability patterns.

However, the synthesized silicone-based nanostructures are normally limited in real applications due to the lack of simple and controllable modification options on the level of a single nanostructure.

In the final part of this thesis, based on the d-DAGS method, the newly proposed synthesis and functionalization strategies lifted the conventional silicone nanostructures to a more advanced level with the following features: *(i)* The MCH nanostructures, including MCH-SNRs and MCH-SMHs, with desired region-specific properties and controllable morphologies had been dynamically synthesized via the one-step in situ method (d-DAGS). Small units, with or without modifiable regions, could be arranged in a specific order on-demand to form heterogeneous bamboo-shaped and mushroom-shaped morphologies. The co-existence of the inert and reactive components enables the as-prepared superhydrophobic products to be modified directly and selectively. *(ii)* The RSF had been successfully performed on the level of a single nanostructure. Various thiol derivatives (functional groups) were loaded on the selectable specific region of the MCH-SNRs and MCH-SMHs samples via photoinitiated radical-based thiol-ene click reactions. *(iii)* Based on the studies of the surface-wetting behaviors of the MCH-SNRs with and without the RSF, a new theory, so-called RSP, was developed, which illustrates that the ETCS-based segments can selectively protect the loaded terminal functional groups after the RSF through physically blocking their contact with water or other solvents when the VTCS-based segment is located between two or more inert ETCS-based segments. *(iv)* The water penetration status was visually revealed using confocal microscopy, and the existence of the intermediate wetting state was therefore verified. *(v)* MCH-SMHs structures were proved to be a promising surface functional coating because of their robust anti-adhesive ability.

In conclusion, the results presented in this thesis demonstrated that the d-DAGS method is facile, efficient, and low-cost, which enables the customization of multifunctional silicone coatings at the nanoscale on-demand, paving the way for designing and synthesizing versatile silicone micro and nanostructures with unique shapes and chemical compositions. The RSF strategy will lead to the development of novel

versatile MCH silicone materials and will shed new light on silicone materials to be applied in the fields like biology, diagnosis, catalysis, and functional surface coating. With the conclusions in material science and nanotechnology, replicating the presented methods on different types of functional silanes and other materials will be an exciting field for future research.

References

1. Artus, G. R. J.; Jung, S.; Zimmermann, J.; Gautschi, H.-P.; Marquardt, K.; Seeger, S., Silicone Nanofilaments and Their Application as Superhydrophobic Coatings. *Advanced Materials* **2006**, *18* (20), 2758-2762.
2. Wang, D.; Sun, Q.; Hokkanen, M. J.; Zhang, C.; Lin, F.-Y.; Liu, Q.; Zhu, S.-P.; Zhou, T.; Chang, Q.; He, B.; Zhou, Q.; Chen, L.; Wang, Z.; Ras, R. H. A.; Deng, X., Design of robust superhydrophobic surfaces. *Nature* **2020**, *582* (7810), 55-59.
3. Lu, Y.; Sathasivam, S.; Song, J.; Chen, F.; Xu, W.; Carmalt, C. J.; Parkin, I. P., Creating superhydrophobic mild steel surfaces for water proofing and oil-water separation. *Journal of Materials Chemistry A* **2014**, *2* (30), 11628-11634.
4. Chen, R.; Zhang, X.; Su, Z.; Gong, R.; Ge, X.; Zhang, H.; Wang, C., Perfectly Hydrophobic Silicone Nanofiber Coatings: Preparation from Methyltrialkoxysilanes and Use as Water-Collecting Substrate. *The Journal of Physical Chemistry C* **2009**, *113* (19), 8350-8356.
5. Zhang, X.; Liu, S.; Salim, A.; Seeger, S., Hierarchical Structured Multifunctional Self-Cleaning Material with Durable Superhydrophobicity and Photocatalytic Functionalities. *Small* **2019**, *15* (34), 1901822.
6. Min, W.-L.; Jiang, B.; Jiang, P., Bioinspired Self-Cleaning Antireflection Coatings. *Advanced Materials* **2008**, *20* (20), 3914-3918.
7. Wong, J. X. H.; Yu, H.-Z., Preparation of Transparent Superhydrophobic Glass Slides: Demonstration of Surface Chemistry Characteristics. *Journal of Chemical Education* **2013**, *90* (9), 1203-1206.
8. Iwasaki, Y.; Omichi, Y.; Iwata, R., Site-Specific Dense Immobilization of Antibody Fragments on Polymer Brushes Supported by Silicone Nanofilaments. *Langmuir* **2008**, *24* (16), 8427-8430.
9. Yohe, S. T.; Colson, Y. L.; Grinstaff, M. W., Superhydrophobic Materials for Tunable Drug Release: Using Displacement of Air To Control Delivery Rates. *Journal of the American Chemical Society* **2012**, *134* (4), 2016-2019.

10. Chu, Z.; Feng, Y.; Seeger, S., Oil/Water Separation with Selective Superantiwetting/Superwetting Surface Materials. *Angewandte Chemie International Edition* **2015**, *54* (8), 2328-2338.
11. Zhang, D.; Wang, W.; Peng, F.; Kou, J.; Ni, Y.; Lu, C.; Xu, Z., A bio-inspired inner-motile photocatalyst film: a magnetically actuated artificial cilia photocatalyst. *Nanoscale* **2014**, *6* (10), 5516-5525.
12. Artus, G. R. J.; Seeger, S., One-dimensional silicone nanofilaments. *Advances in Colloid and Interface Science* **2014**, *209*, 144-162.
13. Zhang, J.; Li, L.; Li, B.; Seeger, S., Solvent-controlled growth of silicone nanofilaments. *RSC Advances* **2014**, *4* (63), 33424-33430.
14. Zimmermann, J.; Artus, G. R. J.; Seeger, S., Superhydrophobic Silicone Nanofilament Coatings. *Journal of Adhesion Science and Technology* **2008**, *22* (3-4), 251-263.
15. Zimmermann, J.; Reifler, F. A.; Fortunato, G.; Gerhardt, L.-C.; Seeger, S., A Simple, One-Step Approach to Durable and Robust Superhydrophobic Textiles. *Advanced Functional Materials* **2008**, *18* (22), 3662-3669.
16. Artus, G. R. J.; Bottone, D.; Seeger, S., Silicon Oxycarbide Coatings Consisting of Defined Bottom-Up-Grown Nanostructures. *Small* **2023**, *n/a* (n/a), 2303079.
17. Barthlott, W.; Neinhuis, C., Purity of the sacred lotus, or escape from contamination in biological surfaces. *Planta* **1997**, *202* (1), 1-8.
18. Meseck, G. R.; Fabbri, E.; Schmidt, T. J.; Seeger, S., Silicone Nanofilament Supported Nickel Oxide: A New Concept for Oxygen Evolution Catalysts in Water Electrolyzers. *Advanced Materials Interfaces* **2015**, *2* (12), 1500216.
19. Meier, M.; Suppiger, A.; Eberl, L.; Seeger, S., Functional Silver-Silicone-Nanofilament-Composite Material for Water Disinfection. *Small* **2017**, *13* (4), 1601072.
20. Bottone, D.; Donadei, V.; Niemelä, H.; Koivuluoto, H.; Seeger, S., Coral-like silicone nanofilament coatings with extremely low ice adhesion. *Scientific Reports* **2021**, *11* (1), 20427.
21. Zahner, D.; Abagat, J.; Svec, F.; Fréchet, J. M. J.; Levkin, P. A., A Facile Approach to Superhydrophilic-Superhydrophobic Patterns in Porous Polymer Films. *Advanced Materials* **2011**, *23* (27), 3030-3034.

22. Artus, G. R. J.; Oliveira, S.; Patra, D.; Seeger, S., Directed In Situ Shaping of Complex Nano- and Microstructures during Chemical Synthesis. *Macromolecular Rapid Communications* **2017**, *38* (4), 1600558.
23. Chen, K.; Liu, S.; Lau, Y.-Y.; Seeger, S., One-Step Synthesis of Dynamically Shaped Stiff Nanorods Using Soft Silicone Materials to Control Water Repulsion and Collection. *Small* **2022**, *18* (40), 2203820.
24. Liu, S.; Zhang, X.; Seeger, S., Solvent-Free Fabrication of Flexible and Robust Superhydrophobic Composite Films with Hierarchical Micro/Nanostructures and Durable Self-Cleaning Functionality. *ACS Applied Materials & Interfaces* **2019**, *11* (47), 44691-44699.
25. Liu, S.; Chen, K.; Salim, A.; Li, J.; Bottone, D.; Seeger, S., Printable and Versatile Superhydrophobic Paper via Scalable Nonsolvent Armor Strategy. *ACS Nano* **2022**, *16* (6), 9442-9451.
26. Oliveira, S.; Stojanovic, A.; Seeger, S., Systematic parametric investigation on the CVD process of polysiloxane nano- and microstructures. *Journal of Nanoparticle Research* **2018**, *20* (11), 307.
27. Baidya, A.; Ganayee, M. A.; Jakka Ravindran, S.; Tam, K. C.; Das, S. K.; Ras, R. H. A.; Pradeep, T., Organic Solvent-Free Fabrication of Durable and Multifunctional Superhydrophobic Paper from Waterborne Fluorinated Cellulose Nanofiber Building Blocks. *ACS Nano* **2017**, *11* (11), 11091-11099.
28. Chen, S.; Li, X.; Li, Y.; Sun, J., Intumescent Flame-Retardant and Self-Healing Superhydrophobic Coatings on Cotton Fabric. *ACS Nano* **2015**, *9* (4), 4070-4076.
29. Qian, B.; Shen, Z., Fabrication of Superhydrophobic Surfaces by Dislocation-Selective Chemical Etching on Aluminum, Copper, and Zinc Substrates. *Langmuir* **2005**, *21* (20), 9007-9009.
30. Cheng, Y.; Zhu, T.; Li, S.; Huang, J.; Mao, J.; Yang, H.; Gao, S.; Chen, Z.; Lai, Y., A novel strategy for fabricating robust superhydrophobic fabrics by environmentally-friendly enzyme etching. *Chemical Engineering Journal* **2019**, *355*, 290-298.
31. Li, Z.; Cao, M.; Li, P.; Zhao, Y.; Bai, H.; Wu, Y.; Jiang, L., Surface-Embedding of Functional Micro-/Nanoparticles for Achieving Versatile Superhydrophobic Interfaces. *Matter* **2019**, *1* (3), 661-673.
32. Peng, C.; Chen, Z.; Tiwari, M. K., All-organic superhydrophobic coatings with mechanochemical robustness and liquid impalement resistance. *Nature Materials* **2018**,

17 (4), 355-360.

33. Li, Z.; Milionis, A.; Zheng, Y.; Yee, M.; Codispoti, L.; Tan, F.; Poulidakos, D.; Yap, C. H., Superhydrophobic hemostatic nanofiber composites for fast clotting and minimal adhesion. *Nature Communications* **2019**, *10* (1), 5562.
34. Stamm, A. J., Thermal Degradation of Wood and Cellulose. *Industrial & Engineering Chemistry* **1956**, *48* (3), 413-417.
35. Huang, X.-J.; Kim, D.-H.; Im, M.; Lee, J.-H.; Yoon, J. B.; Choi, Y.-K., "Lock-and-Key" Geometry Effect of Patterned Surfaces: Wettability and Switching of Adhesive Force. *Small* **2009**, *5* (1), 90-94.
36. Cassie, A. B. D.; Baxter, S., Wettability of porous surfaces. *Transactions of the Faraday Society* **1944**, *40* (0), 546-551.
37. Patankar, N. A., Transition between Superhydrophobic States on Rough Surfaces. *Langmuir* **2004**, *20* (17), 7097-7102.
38. Vörösmarty, C. J.; Green, P.; Salisbury, J.; Lammers, R. B., Global Water Resources: Vulnerability from Climate Change and Population Growth. *Science* **2000**, *289* (5477), 284-288.
39. Kim, H.; Yang, S.; Rao, S. R.; Narayanan, S.; Kapustin, E. A.; Furukawa, H.; Umans, A. S.; Yaghi, O. M.; Wang, E. N., Water harvesting from air with metal-organic frameworks powered by natural sunlight. *Science* **2017**, *356* (6336), 430-434.
40. Kyong Kim, N.; Hee Kang, D.; Eom, H.; Wook Kang, H., Biomimetic fog harvesting surface by photo-induced micro-patterning of zinc-oxide silver hierarchical nanostructures. *Applied Surface Science* **2019**, *470*, 161-167.
41. Tamas-Williams, S.; Todd, I., Design for additive manufacturing with site-specific properties in metals and alloys. *Scripta Materialia* **2017**, *135*, 105-110.
42. Torquato, S., Optimal Design of Heterogeneous Materials. *Annual Review of Materials Research* **2010**, *40* (1), 101-129.
43. Garcia, D.; Jones, M. E.; Zhu, Y.; Yu, H. Z., Mesoscale design of heterogeneous material systems in multi-material additive manufacturing. *Journal of Materials Research* **2018**, *33* (1), 58-67.
44. Vaezi, M.; Chianrabutra, S.; Mellor, B.; Yang, S., Multiple material additive manufacturing – Part 1: a review. *Virtual and Physical Prototyping* **2013**, *8* (1), 19-50.

45. N. Turner, B.; Strong, R.; A. Gold, S., A review of melt extrusion additive manufacturing processes: I. Process design and modeling. *Rapid Prototyping Journal* **2014**, *20* (3), 192-204.
46. Zadpoor, A. A.; Malda, J., Additive Manufacturing of Biomaterials, Tissues, and Organs. *Annals of Biomedical Engineering* **2017**, *45* (1), 1-11.
47. Savitha, U.; Jagan Reddy, G.; Venkataramana, A.; Sambasiva Rao, A.; Gokhale, A. A.; Sundararaman, M., Chemical analysis, structure and mechanical properties of discrete and compositionally graded SS316–IN625 dual materials. *Materials Science and Engineering: A* **2015**, *647*, 344-352.
48. Zhu, Z. G.; An, X. H.; Lu, W. J.; Li, Z. M.; Ng, F. L.; Liao, X. Z.; Ramamurty, U.; Nai, S. M. L.; Wei, J., Selective laser melting enabling the hierarchically heterogeneous microstructure and excellent mechanical properties in an interstitial solute strengthened high entropy alloy. *Materials Research Letters* **2019**, *7* (11), 453-459.
49. Kruth, J. P.; Wang, X.; Laoui, T.; Froyen, L., Lasers and materials in selective laser sintering. *Assembly Automation* **2003**, *23* (4), 357-371.
50. Penumakala, P. K.; Santo, J.; Thomas, A., A critical review on the fused deposition modeling of thermoplastic polymer composites. *Composites Part B: Engineering* **2020**, *201*, 108336.
51. Kipping, F. S.; Lloyd, L. L., XLVII. - Organic derivatives of silicon. Triphenylsilicic and alkyloxysilicon chlorides. *Journal of the Chemical Society, Transactions* **1901**, *79*, 449-459.
52. Wake, W. C., Silicon and silicones E. G. Rochow, Springer-Verlag, Berlin, 1987. pp. xi + 181, price DM 24.80. ISBN 3-540-17565-2. *British Polymer Journal* **1988**, *20* (5), 452-452.
53. Fain, J. H.; Gad, S., Silicones. In *Encyclopedia of Toxicology (Third Edition)*, Wexler, P., Ed. Academic Press: Oxford, 2014; pp 270-272.
54. Arkles, B., Look what you can make out of silicones. **1983**.
55. Baney, R. H.; Itoh, M.; Sakakibara, A.; Suzuki, T., Silsesquioxanes. *Chemical Reviews* **1995**, *95* (5), 1409-1430.
56. Chandra, G.; Maxim, L. D.; Sawano, T., The Silicone Industry and its Environmental Impact. In *Organosilicon Materials*, Chandra, G., Ed. Springer Berlin

Heidelberg: Berlin, Heidelberg, 1997; pp 295-319.

57. Moretto, H.-H.; Schulze, M.; Wagner, G., Silicones. In *Ullmann's Encyclopedia of Industrial Chemistry*, 2000.
58. Little Jr, E. J.; Jones, M. M., A complete table of electronegativities. *Journal of Chemical Education* **1960**, *37* (5), 231.
59. Dankert, F.; von Hänisch, C., Siloxane Coordination Revisited: Si–O Bond Character, Reactivity and Magnificent Molecular Shapes. *European Journal of Inorganic Chemistry* **2021**, *2021* (29), 2907-2927.
60. Kaftory, M.; Kapon, M.; Botoshansky, M., The Structural Chemistry of Organosilicon Compounds. In *The Chemistry of Organic Silicon Compounds*, 1998; pp 181-265.
61. Smith, M. B., *March's advanced organic chemistry: reactions, mechanisms, and structure*. John Wiley & Sons: 2020.
62. Greenwood, N. N.; Earnshaw, A., *Chemistry of the Elements 2nd Edition*. 1997.
63. Vojinović, K.; Losehand, U.; Mitzel, N. W., Dichlorosilane–dimethyl ether aggregation: a new motif in halosilane adduct formation. *Dalton Transactions* **2004**, (16), 2578-2581.
64. Barrow, M. J.; Ebsworth, E. A. V.; Harding, M. M., The crystal and molecular structures of disiloxane (at 108 K) and hexamethyldisiloxane (at 148 K). *Acta Crystallographica Section B* **1979**, *35* (9), 2093-2099.
65. Colas, A.; Curtis, J., 7 - Silicones. In *Handbook of Polymer Applications in Medicine and Medical Devices*, Modjarrad, K.; Ebnesajjad, S., Eds. William Andrew Publishing: Oxford, 2013; pp 131-143.
66. Chojnowski, J.; Cypriak, M., Silicon-containing polymers. *Jones, RG., Ando, W., and Chojnowski, J., Eds* **2000**, 3.
67. Lickiss, P. D., The Synthesis and Structure of Organosilanols. In *Advances in Inorganic Chemistry*, Sykes, A. G., Ed. Academic Press: 1995; Vol. 42, pp 147-262.
68. Wolf, M. P.; Salieb-Beugelaar, G. B.; Hunziker, P., PDMS with designer functionalities—Properties, modifications strategies, and applications. *Progress in Polymer Science* **2018**, *83*, 97-134.

69. Fromme, H., Cyclic Volatile Methylsiloxanes: Occurrence and Exposure. In *Encyclopedia of Environmental Health (Second Edition)*, Nriagu, J., Ed. Elsevier: Oxford, 2019; pp 805-812.
70. Fadeev, A. Y.; McCarthy, T. J., Self-Assembly Is Not the Only Reaction Possible between Alkyltrichlorosilanes and Surfaces: Monomolecular and Oligomeric Covalently Attached Layers of Dichloro- and Trichloroalkylsilanes on Silicon. *Langmuir* **2000**, *16* (18), 7268-7274.
71. Fadeev, A. Y.; McCarthy, T. J., Trialkylsilane Monolayers Covalently Attached to Silicon Surfaces: Wettability Studies Indicating that Molecular Topography Contributes to Contact Angle Hysteresis. *Langmuir* **1999**, *15* (11), 3759-3766.
72. Gao; McCarthy, T. J., (CH₃)₃SiCl/SiCl₄ Azeotrope Grows Superhydrophobic Nanofilaments. *Langmuir* **2008**, *24* (2), 362-364.
73. Rollings, D.-a. E.; Veinot, J. G. C., Polysiloxane Nanofibers via Surface Initiated Polymerization of Vapor Phase Reagents: A Mechanism of Formation and Variable Wettability of Fiber-Bearing Substrates. *Langmuir* **2008**, *24* (23), 13653-13662.
74. Zhang, J.; Seeger, S., Silica/Silicone Nanofilament Hybrid Coatings with Almost Perfect Superhydrophobicity. *ChemPhysChem* **2013**, *14* (8), 1646-1651.
75. Nouri, N. M.; Sekhavat, S.; Bayani Ahangar, S.; Faal Nazari, N., Effect of Curing Condition on Superhydrophobic Surface for 7075Al. *Journal of Dispersion Science and Technology* **2012**, *33* (6), 771-774.
76. Zhang, J.; Seeger, S., Polyester Materials with Superwetting Silicone Nanofilaments for Oil/Water Separation and Selective Oil Absorption. *Advanced Functional Materials* **2011**, *21* (24), 4699-4704.
77. Hua, Z.; Yang, J.; Wang, T.; Liu, G.; Zhang, G., Transparent Surface with Reversibly Switchable Wettability between Superhydrophobicity and Superhydrophilicity. *Langmuir* **2013**, *29* (33), 10307-10312.
78. Chua, M. H.; Zhou, H.; Xu, J., Chapter 15 - Polymer-POSS hybrid materials as fire retardants. In *Polyhedral Oligomeric Silsesquioxane (POSS) Polymer Nanocomposites*, Thomas, S.; Somasekharan, L., Eds. Elsevier: 2021; pp 305-332.
79. Oh, W.; Ree, M., Anisotropic Thermal Expansion Behavior of Thin Films of Polymethylsilsesquioxane, a Spin-on-Glass Dielectric for High-Performance Integrated Circuits. *Langmuir* **2004**, *20* (16), 6932-6939.

80. Dong, H.; Brook, M. A.; Brennan, J. D., A New Route to Monolithic Methylsilsesquioxanes: Gelation Behavior of Methyltrimethoxysilane and Morphology of Resulting Methylsilsesquioxanes under One-Step and Two-Step Processing. *Chemistry of Materials* **2005**, *17* (11), 2807-2816.
81. Zimmermann, J.; Seeger, S.; Artus, G.; Jung, S., Superhydrophobic coating. Google Patents: 2011.
82. Gao, L.; McCarthy, T. J., A Perfectly Hydrophobic Surface ($\theta_A/\theta_R = 180^\circ/180^\circ$). *Journal of the American Chemical Society* **2006**, *128* (28), 9052-9053.
83. Acatay, K.; Simsek, E.; Ow-Yang, C.; Menciloglu, Y. Z., Tunable, Superhydrophobically Stable Polymeric Surfaces by Electrospinning. *Angewandte Chemie International Edition* **2004**, *43* (39), 5210-5213.
84. Zheng, J.; He, A.; Li, J.; Xu, J.; Han, C. C., Studies on the controlled morphology and wettability of polystyrene surfaces by electrospinning or electro spraying. *Polymer* **2006**, *47* (20), 7095-7102.
85. Zhang, B.; Zhao, X.; Li, Y.; Hou, B., Fabrication of durable anticorrosion superhydrophobic surfaces on aluminum substrates via a facile one-step electrodeposition approach. *RSC Advances* **2016**, *6* (42), 35455-35465.
86. Meng, H.; Wang, S.; Xi, J.; Tang, Z.; Jiang, L., Facile Means of Preparing Superamphiphobic Surfaces on Common Engineering Metals. *The Journal of Physical Chemistry C* **2008**, *112* (30), 11454-11458.
87. Zhang, X.; Zheng, F.; Ye, L.; Xiong, P.; Yan, L.; Yang, W.; Jiang, B., A one-pot sol-gel process to prepare a superhydrophobic and environment-resistant thin film from ORMOSIL nanoparticles. *RSC Advances* **2014**, *4* (19), 9838-9841.
88. Qi, D.; Lu, N.; Xu, H.; Yang, B.; Huang, C.; Xu, M.; Gao, L.; Wang, Z.; Chi, L., Simple Approach to Wafer-Scale Self-Cleaning Antireflective Silicon Surfaces. *Langmuir* **2009**, *25* (14), 7769-7772.
89. Li, M.; Xu, J.; Lu, Q., Creating superhydrophobic surfaces with flowery structures on nickel substrates through a wet-chemical-process. *Journal of Materials Chemistry* **2007**, *17* (45), 4772-4776.
90. Ren, H.-X.; Chen, X.; Huang, X.-J.; Im, M.; Kim, D.-H.; Lee, J.-H.; Yoon, J.-B.; Gu, N.; Liu, J.-H.; Choi, Y.-K., A conventional route to scalable morphology-controlled regular structures and their superhydrophobic/hydrophilic properties for biochips application. *Lab on a Chip* **2009**, *9* (15), 2140-2144.

91. Park, Y.-B.; Im, M.; Im, H.; Choi, Y.-K., Superhydrophobic Cylindrical Nanoshell Array. *Langmuir* **2010**, *26* (11), 7661-7664.
92. Cai, Z.; Lin, J.; Hong, X., Transparent superhydrophobic hollow films (TSHFs) with superior thermal stability and moisture resistance. *RSC Advances* **2018**, *8* (1), 491-498.
93. Hooda, A.; Goyat, M. S.; Pandey, J. K.; Kumar, A.; Gupta, R., A review on fundamentals, constraints and fabrication techniques of superhydrophobic coatings. *Progress in Organic Coatings* **2020**, *142*, 105557.
94. Parvate, S.; Dixit, P.; Chattopadhyay, S., Superhydrophobic Surfaces: Insights from Theory and Experiment. *The Journal of Physical Chemistry B* **2020**, *124* (8), 1323-1360.
95. Chu, Z.; Seeger, S., Robust superhydrophobic wood obtained by spraying silicone nanoparticles. *RSC Advances* **2015**, *5* (28), 21999-22004.
96. Wang, Y.; Cao, R.; Wang, M.; Liu, X.; Zhao, X.; Lu, Y.; Feng, A.; Zhang, L., Design and synthesis of phenyl silicone rubber with functional epoxy groups through anionic copolymerization and subsequent epoxidation. *Polymer* **2020**, *186*, 122077.
97. Zhang, W.; Li, X.; Shan, Z.; Wang, S.; Xiao, Y., Surface modification of magnesium hydroxide by wet process and effect on the thermal stability of silicone rubber. *Applied Surface Science* **2019**, *465*, 740-746.
98. Artus, G. R. J.; Seeger, S., Scale-Up of a Reaction Chamber for Superhydrophobic Coatings Based on Silicone Nanofilaments. *Industrial & Engineering Chemistry Research* **2012**, *51* (6), 2631-2636.
99. Shirgholami, M. A.; Shateri Khalil-Abad, M.; Khajavi, R.; Yazdanshenas, M. E., Fabrication of superhydrophobic polymethylsilsesquioxane nanostructures on cotton textiles by a solution-immersion process. *Journal of Colloid and Interface Science* **2011**, *359* (2), 530-535.
100. Timonen, J. V. I.; Latikka, M.; Leibler, L.; Ras, R. H. A.; Ikkala, O., Switchable Static and Dynamic Self-Assembly of Magnetic Droplets on Superhydrophobic Surfaces. *Science* **2013**, *341* (6143), 253-257.
101. Korhonen, J. T.; Huhtamäki, T.; Ikkala, O.; Ras, R. H. A., Reliable Measurement of the Receding Contact Angle. *Langmuir* **2013**, *29* (12), 3858-3863.
102. Rollings, D.-a. E.; Tsoi, S.; Sit, J. C.; Veinot, J. G. C., Formation and Aqueous

Surface Wettability of Polysiloxane Nanofibers Prepared via Surface Initiated, Vapor-Phase Polymerization of Organotrichlorosilanes. *Langmuir* **2007**, *23* (10), 5275-5278.

103. Saddiqi, N.-u.-H.; Patra, D.; Seeger, S., Room-Temperature Synthesis of Germanium Oxide Nanofilaments and Their Potential Use as Luminescent Self-Cleaning Surfaces. *ChemPhysChem* **2019**, *20* (4), 538-544.

104. Cao, P.; Xu, K.; Varghese, J. O.; Heath, J. R., The Microscopic Structure of Adsorbed Water on Hydrophobic Surfaces under Ambient Conditions. *Nano Letters* **2011**, *11* (12), 5581-5586.

105. James, M.; Darwish, T. A.; Ciampi, S.; Sylvester, S. O.; Zhang, Z.; Ng, A.; Gooding, J. J.; Hanley, T. L., Nanoscale condensation of water on self-assembled monolayers. *Soft Matter* **2011**, *7* (11), 5309-5318.

106. Buck, A. L., New Equations for Computing Vapor Pressure and Enhancement Factor. *Journal of Applied Meteorology and Climatology* **1981**, *20* (12), 1527-1532.

107. Wallin, T. J.; Simonsen, L.-E.; Pan, W.; Wang, K.; Giannelis, E.; Shepherd, R. F.; Mengüç, Y., 3D printable tough silicone double networks. *Nature Communications* **2020**, *11* (1), 4000.

108. Davoodi, E.; Montazerian, H.; Haghniaz, R.; Rashidi, A.; Ahadian, S.; Sheikhi, A.; Chen, J.; Khademhosseini, A.; Milani, A. S.; Hoorfar, M.; Toyserkani, E., 3D-Printed Ultra-Robust Surface-Doped Porous Silicone Sensors for Wearable Biomonitoring. *ACS Nano* **2020**, *14* (2), 1520-1532.

109. Lam, M.; Migonney, V.; Falentin-Daudre, C., Review of silicone surface modification techniques and coatings for antibacterial/antimicrobial applications to improve breast implant surfaces. *Acta Biomaterialia* **2021**, *121*, 68-88.

110. Li, J.; Li, L.; Du, X.; Feng, W.; Welle, A.; Trapp, O.; Grunze, M.; Hirtz, M.; Levkin, P. A., Reactive Superhydrophobic Surface and Its Photoinduced Disulfide-ene and Thiol-ene (Bio)functionalization. *Nano Letters* **2015**, *15* (1), 675-681.

111. Zimmermann, J.; Rabe, M.; Artus, G. R. J.; Seeger, S., Patterned superfunctional surfaces based on a silicone nanofilament coating. *Soft Matter* **2008**, *4* (3), 450-452.

112. Zhang, J.; Seeger, S., Superoleophobic Coatings with Ultralow Sliding Angles Based on Silicone Nanofilaments. *Angewandte Chemie International Edition* **2011**, *50* (29), 6652-6656.

113. Meseck, G. R.; Kontic, R.; Patzke, G. R.; Seeger, S., Photocatalytic

Composites of Silicone Nanofilaments and TiO₂ Nanoparticles. *Advanced Functional Materials* **2012**, 22 (21), 4433-4438.

114. Wang, D.; Gao, Y.; Gao, S.; Huang, H.; Min, F.; Li, Y.; Seeger, S.; Jin, J.; Chu, Z., Antifouling superhydrophilic porous glass membrane based on sulfobetaine prepared by thiol-ene click chemistry for high-efficiency oil/water separation. *Journal of Membrane Science* **2023**, 670, 121336.

115. Guo, J.; Fang, W.; Welle, A.; Feng, W.; Filpponen, I.; Rojas, O. J.; Levkin, P. A., Superhydrophobic and Slippery Lubricant-Infused Flexible Transparent Nanocellulose Films by Photoinduced Thiol-Ene Functionalization. *ACS Applied Materials & Interfaces* **2016**, 8 (49), 34115-34122.

116. Li, X.; Zhang, W.; Qu, R.; Liu, Y.; Wei, Y.; Feng, L., Asymmetric superwetting configuration of Janus membranes based on thiol-ene clickable silane nanospheres enabling on-demand and energy-efficient oil-water remediation. *Journal of Materials Chemistry A* **2019**, 7 (16), 10047-10057.

117. Bordoni, A. V.; Lombardo, M. V.; Wolosiuk, A., Photochemical radical thiol-ene click-based methodologies for silica and transition metal oxides materials chemical modification: a mini-review. *RSC Advances* **2016**, 6 (81), 77410-77426.

118. Asanuma, H.; Noguchi, H.; Uosaki, K.; Yu, H.-Z., Water Structure at Superhydrophobic Quartz/Water Interfaces: A Vibrational Sum Frequency Generation Spectroscopy Study. *The Journal of Physical Chemistry C* **2009**, 113 (50), 21155-21161.

119. Artus, G. R. J.; Zimmermann, J.; Reifler, F. A.; Brewer, S. A.; Seeger, S., A superoleophobic textile repellent towards impacting drops of alkanes. *Applied Surface Science* **2012**, 258 (8), 3835-3840.

120. Khoo, H. S.; Tseng, F.-G., Spontaneous high-speed transport of subnanoliter water droplet on gradient nanotextured surfaces. *Applied Physics Letters* **2009**, 95 (6), 063108.

121. Quéré, D., Wetting and Roughness. *Annual Review of Materials Research* **2008**, 38 (1), 71-99.

122. Verho, T.; Korhonen, J. T.; Sainiemi, L.; Jokinen, V.; Bower, C.; Franze, K.; Franssila, S.; Andrew, P.; Ikkala, O.; Ras, R. H. A., Reversible switching between superhydrophobic states on a hierarchically structured surface. *Proceedings of the National Academy of Sciences* **2012**, 109 (26), 10210-10213.

123. Zimmermann, J.; Rabe, M.; Verdes, D.; Seeger, S., Functionalized Silicone Nanofilaments: A Novel Material for Selective Protein Enrichment. *Langmuir* **2008**,

24 (3), 1053-1057.

124. Lau, Y.-Y.; Chen, K.; Liu, S.; Reith, L.; Seeger, S., Silicone Nanofilament Coatings as Flexible Catalyst Supports for a Knoevenagel Condensation Reaction in Batch and Flow Systems. *ACS Omega* **2022**, 7 (43), 39463-39470.

125. Young, T., III. An essay on the cohesion of fluids. *Philosophical Transactions of the Royal Society of London* **1997**, 95, 65-87.

126. Nishino, T.; Meguro, M.; Nakamae, K.; Matsushita, M.; Ueda, Y., The Lowest Surface Free Energy Based on $-CF_3$ Alignment. *Langmuir* **1999**, 15 (13), 4321-4323.

127. Extrand, C. W., Designing for Optimum Liquid Repellency. *Langmuir* **2006**, 22 (4), 1711-1714.

128. Wenzel, R. N., RESISTANCE OF SOLID SURFACES TO WETTING BY WATER. *Industrial & Engineering Chemistry* **1936**, 28 (8), 988-994.

129. Tuteja, A.; Choi, W.; Ma, M.; Mabry, J. M.; Mazzella, S. A.; Rutledge, G. C.; McKinley, G. H.; Cohen, R. E., Designing Superoleophobic Surfaces. *Science* **2007**, 318 (5856), 1618-1622.

130. Butt, H.-J.; Roisman, I. V.; Brinkmann, M.; Papadopoulos, P.; Vollmer, D.; Semprebon, C., Characterization of super liquid-repellent surfaces. *Current Opinion in Colloid & Interface Science* **2014**, 19 (4), 343-354.

131. Nagayama, G.; Zhang, D., Intermediate wetting state at nano/microstructured surfaces. *Soft Matter* **2020**, 16 (14), 3514-3521.

132. Bormashenko, E., Progress in understanding wetting transitions on rough surfaces. *Advances in Colloid and Interface Science* **2015**, 222, 92-103.

133. Miwa, M.; Nakajima, A.; Fujishima, A.; Hashimoto, K.; Watanabe, T., Effects of the Surface Roughness on Sliding Angles of Water Droplets on Superhydrophobic Surfaces. *Langmuir* **2000**, 16 (13), 5754-5760.

134. Marmur, A., Wetting on Hydrophobic Rough Surfaces: To Be Heterogeneous or Not To Be? *Langmuir* **2003**, 19 (20), 8343-8348.

135. Luo, C.; Xiang, M.; Heng, X., A Stable Intermediate Wetting State after a Water Drop Contacts the Bottom of a Microchannel or Is Placed on a Single Corner. *Langmuir* **2012**, 28 (25), 9554-9561.

136. Luo, C.; Xiang, M., Existence and stability of an intermediate wetting state on circular micropillars. *Microfluidics and Nanofluidics* **2014**, *17* (3), 539-548.
137. Yu, Y.; Zhang, D.; Nagayama, G., Estimation of surface free energy at microstructured surface to investigate intermediate wetting state for partial wetting model. *Soft Matter* **2023**, *19* (6), 1249-1257.
138. Zhang, X.; Seeger, S., Morphology Tuneable and Multifunctional Polystyrene-Silicone Nano-Composite Materials. *ChemNanoMat* **2019**, *5* (7), 964-971.
139. Liu, S.; Yin, S.; Duvigneau, J.; Vancso, G. J., Bubble Seeding Nanocavities: Multiple Polymer Foam Cell Nucleation by Polydimethylsiloxane-Grafted Designer Silica Nanoparticles. *ACS Nano* **2020**, *14* (2), 1623-1634.
140. Kim, H.; Kim, H.-G.; Kim, S.; Kim, S. S., PDMS–silica composite membranes with silane coupling for propylene separation. *Journal of Membrane Science* **2009**, *344* (1), 211-218.
141. Zhang, J.; Zhu, C.; Lv, J.; Zhang, W.; Feng, J., Preparation of Colorful, Infrared-Reflective, and Superhydrophobic Polymer Films with Obvious Resistance to Dust Deposition. *ACS Applied Materials & Interfaces* **2018**, *10* (46), 40219-40227.
142. Gao, X.; Jiang, L., Water-repellent legs of water striders. *Nature* **2004**, *432* (7013), 36-36.
143. Chandra, D.; Yang, S.; Soshinsky, A. A.; Gambogi, R. J., Biomimetic Ultrathin Whitening by Capillary-Force-Induced Random Clustering of Hydrogel Micropillar Arrays. *ACS Applied Materials & Interfaces* **2009**, *1* (8), 1698-1704.
144. Chandra, D.; Yang, S., Capillary-Force-Induced Clustering of Micropillar Arrays: Is It Caused by Isolated Capillary Bridges or by the Lateral Capillary Meniscus Interaction Force? *Langmuir* **2009**, *25* (18), 10430-10434.
145. Meisser, U. KOL-05. <https://uzh.canto.global/v/DAM/album/T132S?viewIndex=1&display=fitView&column=image&id=sgmlqhgb2t0170bhvmpq9i5s13> (accessed 2023-07-03).
146. Zhang, L.; Zhou, A. G.; Sun, B. R.; Chen, K. S.; Yu, H.-Z., Functional and versatile superhydrophobic coatings via stoichiometric silanization. *Nature Communications* **2021**, *12* (1), 982.
147. Encinas, N.; Yang, C.-Y.; Geyer, F.; Kaltbeitzel, A.; Baumli, P.; Reinholz, J.; Mailänder, V.; Butt, H.-J.; Vollmer, D., Submicrometer-Sized Roughness Suppresses Bacteria Adhesion. *ACS Applied Materials & Interfaces* **2020**, *12* (19), 21192-21200.

148. Wang, R.; Takeda, M.; Kido, M., Micro pure water wettability evaluation with an AC no-contact mode of atomic force microscope. *Materials Letters* **2002**, *54* (2), 140-144.
149. Kumar, M.; Ando, Y., Chemical Vapor Deposition of Carbon Nanotubes: A Review on Growth Mechanism and Mass Production. *Journal of Nanoscience and Nanotechnology* **2010**, *10* (6), 3739-3758.
150. Picknett, R. G.; Bexon, R., The evaporation of sessile or pendant drops in still air. *Journal of Colloid and Interface Science* **1977**, *61* (2), 336-350.
151. Erbil, H. Y., Evaporation of pure liquid sessile and spherical suspended drops: A review. *Advances in Colloid and Interface Science* **2012**, *170* (1), 67-86.
152. Hwang, G. B.; Patir, A.; Page, K.; Lu, Y.; Allan, E.; Parkin, I. P., Buoyancy increase and drag-reduction through a simple superhydrophobic coating. *Nanoscale* **2017**, *9* (22), 7588-7594.
153. Lu, J.; Ngo, C.-V.; Singh, S. C.; Yang, J.; Xin, W.; Yu, Z.; Guo, C., Bioinspired Hierarchical Surfaces Fabricated by Femtosecond Laser and Hydrothermal Method for Water Harvesting. *Langmuir* **2019**, *35* (9), 3562-3567.
154. Bai, H.; Tian, X.; Zheng, Y.; Ju, J.; Zhao, Y.; Jiang, L., Direction Controlled Driving of Tiny Water Drops on Bioinspired Artificial Spider Silks. *Advanced Materials* **2010**, *22* (48), 5521-5525.
155. Bai, H.; Ju, J.; Sun, R.; Chen, Y.; Zheng, Y.; Jiang, L., Controlled Fabrication and Water Collection Ability of Bioinspired Artificial Spider Silks. *Advanced Materials* **2011**, *23* (32), 3708-3711.
156. Bai, H.; Sun, R.; Ju, J.; Yao, X.; Zheng, Y.; Jiang, L., Large-Scale Fabrication of Bioinspired Fibers for Directional Water Collection. *Small* **2011**, *7* (24), 3429-3433.
157. Cao, M.; Ju, J.; Li, K.; Dou, S.; Liu, K.; Jiang, L., Facile and Large-Scale Fabrication of a Cactus-Inspired Continuous Fog Collector. *Advanced Functional Materials* **2014**, *24* (21), 3235-3240.
158. Bintein, P.-B.; Lhuissier, H.; Mongruel, A.; Royon, L.; Beysens, D., Grooves Accelerate Dew Shedding. *Physical Review Letters* **2019**, *122* (9), 098005.
159. Zhang, J.; Chen, F.; Lu, Y.; Zhang, Z.; Liu, J.; Chen, Y.; Liu, X.; Yang, X.; Carmalt, C. J.; Parkin, I. P., Superhydrophilic–superhydrophobic patterned surfaces on glass substrate for water harvesting. *Journal of Materials Science* **2020**, *55* (2), 498-508.

160. Yu, Z.; Yun, F. F.; Wang, Y.; Yao, L.; Dou, S.; Liu, K.; Jiang, L.; Wang, X., Desert Beetle-Inspired Superwetable Patterned Surfaces for Water Harvesting. *Small* **2017**, *13* (36), 1701403.
161. Nioras, D.; Ellinas, K.; Constantoudis, V.; Gogolides, E., How Different Are Fog Collection and Dew Water Harvesting on Surfaces with Different Wetting Behaviors? *ACS Applied Materials & Interfaces* **2021**, *13* (40), 48322-48332.
162. Zhu, H.; Duan, R.; Wang, X.; Yang, J.; Wang, J.; Huang, Y.; Xia, F., Prewetting dichloromethane induced aqueous solution adhered on Cassie superhydrophobic substrates to fabricate efficient fog-harvesting materials inspired by Namib Desert beetles and mussels. *Nanoscale* **2018**, *10* (27), 13045-13054.
163. Zhu, H.; Cai, S.; Zhou, J.; Li, S.; Wang, D.; Zhu, J.; Wu, Y.; Huang, Y.; Yuan, S.; Jin, S.; Xia, F., Integration of water collection and purification on cactus- and beetle-inspired eco-friendly superwetable materials. *Water Research* **2021**, *206*, 117759.
164. Zhong, L.; Feng, J.; Guo, Z., An alternating nanoscale (hydrophilic–hydrophobic)/hydrophilic Janus cooperative copper mesh fabricated by a simple liquidus modification for efficient fog harvesting. *Journal of Materials Chemistry A* **2019**, *7* (14), 8405-8413.
165. Garrod, R. P.; Harris, L. G.; Schofield, W. C. E.; McGettrick, J.; Ward, L. J.; Teare, D. O. H.; Badyal, J. P. S., Mimicking a Stenocara Beetle's Back for Microcondensation Using Plasmachemical Patterned Superhydrophobic–Superhydrophilic Surfaces. *Langmuir* **2007**, *23* (2), 689-693.
166. Thickett, S. C.; Neto, C.; Harris, A. T., Biomimetic Surface Coatings for Atmospheric Water Capture Prepared by Dewetting of Polymer Films. *Advanced Materials* **2011**, *23* (32), 3718-3722.
167. Ishizaki, T.; Saito, N.; Takai, O., Correlation of Cell Adhesive Behaviors on Superhydrophobic, Superhydrophilic, and Micropatterned Superhydrophobic/Superhydrophilic Surfaces to Their Surface Chemistry. *Langmuir* **2010**, *26* (11), 8147-8154.
168. Stojanovic, A.; Artus, G. R. J.; Seeger, S., Micropatterning of superhydrophobic silicone nanofilaments by a near-ultraviolet Nd:YAG laser. *Nano Research* **2010**, *3* (12), 889-894.
169. Zhang, J.; Wang, A.; Seeger, S., Nepenthes Pitcher Inspired Anti-Wetting Silicone Nanofilaments Coatings: Preparation, Unique Anti-Wetting and Self-Cleaning Behaviors. *Advanced Functional Materials* **2014**, *24* (8), 1074-1080.

170. Takao, H.; Okoshi, M.; Inoue, N., Swelling and modification of silicone surface by F2 laser irradiation. *Applied Physics A* **2004**, *79* (4), 1571-1574.
171. Chen, D.; Yi, S.; Wu, W.; Zhong, Y.; Liao, J.; Huang, C.; Shi, W., Synthesis and characterization of novel room temperature vulcanized (RTV) silicone rubbers using Vinyl-POSS derivatives as cross linking agents. *Polymer* **2010**, *51* (17), 3867-3878.
172. Liravi, F.; Toyserkani, E., Additive manufacturing of silicone structures: A review and prospective. *Additive Manufacturing* **2018**, *24*, 232-242.
173. Tucker-Schwartz, A. K.; Farrell, R. A.; Garrell, R. L., Thiol-ene Click Reaction as a General Route to Functional Trialkoxysilanes for Surface Coating Applications. *Journal of the American Chemical Society* **2011**, *133* (29), 11026-11029.
174. Ukaji, E.; Furusawa, T.; Sato, M.; Suzuki, N., The effect of surface modification with silane coupling agent on suppressing the photo-catalytic activity of fine TiO₂ particles as inorganic UV filter. *Applied Surface Science* **2007**, *254* (2), 563-569.
175. Li, X.-M.; Reinhoudt, D.; Crego-Calama, M., What do we need for a superhydrophobic surface? A review on the recent progress in the preparation of superhydrophobic surfaces. *Chemical Society Reviews* **2007**, *36* (8), 1350-1368.
176. Bhushan, B.; Nosonovsky, M., The rose petal effect and the modes of superhydrophobicity. *Philosophical Transactions of the Royal Society A: Mathematical, Physical and Engineering Sciences* **2010**, *368* (1929), 4713-4728.
177. Wang, C.; Shao, R.; Wang, G.; Sun, S., Hierarchical hydrophobic surfaces with controlled dual transition between rose petal effect and lotus effect via structure tailoring or chemical modification. *Colloids and Surfaces A: Physicochemical and Engineering Aspects* **2021**, *622*, 126661.
178. Yu, D. I.; Doh, S. W.; Kwak, H. J.; Kang, H. C.; Ahn, H. S.; Park, H. S.; Kiyofumi, M.; Kim, M. H., Wetting state on hydrophilic and hydrophobic micro-textured surfaces: Thermodynamic analysis and X-ray visualization. *Applied Physics Letters* **2015**, *106* (17), 171602.
179. Varol, H. S.; Seeger, S., Fluorescent Staining of Silicone Micro- and Nanopatterns for Their Optical Imaging. *Langmuir* **2022**, *38* (1), 231-243.
180. Garcia-Cordero, J. L.; Fan, Z. H., Sessile droplets for chemical and biological assays. *Lab on a Chip* **2017**, *17* (13), 2150-2166.

Curriculum Vitae

Name: Chen

First Name: Kangwei

Date of Birth: 24 Feb 1995

Place of Origin: Shandong, China

Education:

- 08.2019 – pres.** PhD Program in Chemical and Molecular Sciences
University of Zurich, Zurich, Switzerland
Thesis: Homo- and Heterogeneous Silicone Micro-Nano Structures: Synthesis, Functionalization and Applications
Supervisor: Prof. Dr. Stefan Seeger
- 09.2016 – 07.2019** MChem (Hons) in Chemistry with Environmental and Sustainable Chemistry
The University of Edinburgh, Edinburgh, United Kingdom
Thesis: Developing and Understanding Functionalized Ionic Liquids (FILs) for Sustainable Recovery of Rare Earth Elements (REEs)
Supervisor: Prof. Jason Love
- 09.2014 – 07.2019** B.Eng in Environmental Engineering (Full English Class)
South China University of Technology, Guangzhou, China

冀以尘雾之微，补葺山海；荧烛末光，增辉日月。

曹植 *Zhi Cao* (192 - 232)



**Universität
Zürich^{UZH}**

CMSZH 
CHEMICAL MOLECULAR SCIENCES ZÜRICH GRADUATE SCHOOL